THE ROLE OF DROPLETS IN THE AUTOIGNITION OF A POLYDISPERSE JET-A SPRAY IN VITIATED CO-FLOW

A Dissertation
Presented to
The Academic Faculty

By

Aimee N. Williams

In Partial Fulfillment
of the Requirements for the Degree
Doctor of Philosophy in the
School of Aerospace Engineering

Georgia Institute of Technology

August 2019

Copyright © Aimee N. Williams 2019

THE ROLE OF DROPLETS IN THE AUTOIGNITION OF A POLYDISPERSE JET-A SPRAY IN VITIATED CO-FLOW

Approved by:

Dr. Jerry M. Seitzman, Co-Advisor
School of Aerospace Engineering
Georgia Institute of Technology

Dr. Jechiel Jagoda
School of Aerospace Engineering
Georgia Institute of Technology

Dr. Joseph Oefelein
School of Aerospace Engineering
Georgia Institute of Technology

Dr. Ben T. Zinn, Co-Advisor
School of Aerospace Engineering
Georgia Institute of Technology

Dr. Jeffrey A. Lovett
Pratt and Whitney

Date Approved: May 30, 2019

The only true failure can come if you quit

Andrea Beaty

To Corey and Ellee

ACKNOWLEDGEMENTS

This thesis would not have been possible without the support of so many wonderful people. First my family, Corey and Ellee, have provided so much support and love. You are both so full of kindness and understanding are an inspiration of how to treat others.

My parents helped me grow my love of science and always supported and encouraged me through my many years of school.

My advisor, Dr. Zinn gave me so many opportunities to learn and grow as an engineer and researcher. You taught me to always ask questions and never trust any answer until I can prove it to myself. I will also always remember to turn on the spark before the fuel. Due to your mentoring I was able to grow from a scared student in a corner watch experiments into a confident engineer with a passion in experimental spray combustion.

My advisor, Dr. Seitzman gave me the opportunity to finish my thesis and provided so much invaluable insight and discussion without which I would not have been able to put together this work. Despite gaining a student you did not choose, you treated me as one of your own and spent so much time with me in meetings and through editing. At a time when my graduate student future felt uncertain you gave me confidence that I could still accomplish my dreams and for that I am eternally grateful.

To my committee, I thank you so much for your time. Your comments and insight have helped me to make this the best work I can do with the experiments I have available.

Eugene Lubarsky has been an incredible mentor to me during my many years at the Combustion Lab. I feel so thankful and privileged to have been able to learn about spray combustion from such a knowledgeable engineer. You helped me discover a passion for experimental testing and analysis and I enjoyed working with you to better understand spray combustion.

To the research engineers Sasha, Dmitriy, and Slava, you each taught me so many things and were willing to help with anything I approached you with. I could not have accom-

plished the work in this thesis without all of the aid and teaching you provided. Sasha, you always made yourself available to help me with diagnostics, lasers, and discussing the capabilities in order to acquire the data I was looking for. Dmitriy, you helped me with so many instrumentation issues, taught me about the science stick, and how zip ties sometimes aren't the best solution. Slava, your design and machining skills were such a huge asset to this research and I hope no one asks you to machine graphite again.

To the rest of the combustion lab family and undergraduates who worked with me - you have been the best peers any person could ask for. The environment created in the lab is one of friendship and encouragement and it makes for a place I thoroughly enjoyed working. It is obvious on a daily basis that each person wants every other person to succeed. I thank you all for helping me when I needed a hand in the lab, or a second person to be available during experiments, and for all the time you spent talking with me.

Lastly, I would like to thank sponsors throughout the years. Pratt and Whitney, and specifically Jeff Lovett, you provided not only financial support for the autoignition test facility, but a wealth of conversation and interpretation of results in telecons and meetings. This work was also partially funded through the National Science Foundation Research Fellowship.

TABLE OF CONTENTS

LIST OF TABLES

LIST OF FIGURES

SUMMARY

The objective of this study is to understand the underlying mechanisms of autoignition of a polydisperse fuel spray. Understanding and predicting autoignition of fuel sprays is important to the design of modern gas turbine engines, especially in the interest of developing a flame-holder-less afterburner concept. Systems that previously required pilot flames could potentially produce stable flames using autoignition.

In this system, liquid fuel is injected into a high temperature, flowing, vitiated air flow. Previous studies of fuel spray autoignition have suggested multiple mechanisms for a fuel spray to autoignite, including single droplet and droplet cloud ignition behavior. The majority of liquid-fueled autoignition studies have been parametric in nature and describe the overall effect of droplet size, equivalence ratio, turbulence intensity, etc. on ignition delay time but do not investigate the phenomena controlling the local behavior of autoignition kernel formation and growth. Autoignition studies of cold gaseous fuel jets in hot oxidizer cross flows have shown the importance of local mixture fraction. Specifically, there is a most reactive mixture fraction that produces the highest reaction rate due to the trade-off between the relative amounts of fuel and oxidizer, and the lower temperature produced when hot oxidizer is mixed with cold fuel. In a liquid fueled system, it is likely that the most reactive mixture fraction could play a role in the formation and growth of autoignition kernels. This study utilizes modern diagnostics to investigate local behavior and determine what methods of autoignition are dominant in more practical sprays, for example those relevant to gas turbines.

A test facility was developed that is capable of reproducing flow conditions in an aero-engine reheat combustor. A natural gas fueled preburner provides elevated temperatures and vitiated oxygen content. Dilution air provides control of the temperature and O_2 concentration. Fuel is injected using a reproduction of a commercially available spray nozzle installed on an aerodynamically shaped body centered in the flow by three aerodynamic

pylons. Caps can be attached over the fuel injector to change the flow in the wake. The test section consists of a 0.9m long, 75mm inner diameter quartz silica tube that provides full optical accessibility to the fuel spray, co-flow, and the region of autoignition kernel formation and their subsequent evolution.

The incoming vitiated co-flow and liquid fuel spray were characterized in order to have well-defined flow conditions. The vitiated flow was characterized using a Pitot/thermocouple traverse, and with LDV and PIV in the region of interest without fuel spray. Results show a relatively uniform flow with a small wake downstream of the fuel injector. The fuel spray was characterized using a PDPA system to determine spatial profiles of droplet sizes and velocities.

High speed chemiluminescence and UV PLIF were used to determine the dependence of the locations where autoignition kernels form, upon the flow temperature and velocity. Combined with velocity measurements, the data provided statistics of autoignition delay times in the spray. The measured delay times were compared to predictions for the most reactive mixture fraction from a constant pressure reactor model and an established chemical mechanism for Jet-A. The measured mean ignition delay times were shorter than the times predicted for prevaporized fuel based on the mean co-flow temperature. Analysis of the scatter in the time-resolved ignition locations revealed the importance of temperature fluctuations in the vitiated flow. Specifically, the most upstream ignition locations likely correspond to the hottest and, therefore, most reactive fluid packets. The average kernel forms further upstream than the location based on the average flow temperature. As the average flow temperature increased, the scatter of autoignition events decreased. Thus, as the chemical time significantly decreases as the temperature increases, the times required to heat up the droplets and vaporize the fuel decreases only slightly. Consequently, these processes become the limiting timescales.

In order to elucidate the dependence of the behavior of autoignition kernels upon the droplet distribution, UV PLIF was used to simultaneously visualize autoignition kernels

and fuel spray in a plane that bisects the test section through the center of the fuel spray. This novel approach provided temporal and spatial resolution of autoignition events and their proximity to fuel droplets. Results show that autoignition is more likely to occur in the vicinity of a fuel droplet; i.e., ignition kernels preferentially occur with a droplet within or at the boundary of the kernel. Furthermore, the ignition kernel preferentially propagates towards nearby droplets, presumably through the vaporized fuel trail. This behavior most closely resembles the cloud ignition theory described in the literature.

With an aerodynamic injector body, the ignition kernels preferentially formed away from center of the spray, which consisted of small droplets which vaporized quickly. Using a blunt body introduced a larger wake and recirculation zone and enhanced mixing of the central region with the main portion of the fuel spray. This led to a higher probability of autoignition kernels in the center of the flow. Finally, a near stationary (on average) flame was found to exist at high co-flow temperatures. However, this flame appears to be stabilized by autoignition, with distinct kernels being formed upstream of the main flame region.

These experimental results can be used to validate the predictions of models of spray ignition. Moreover, these results can guide the design of future combustors, whether for the purpose of using autoignition as a stabilizing mechanism or preventing detrimental autoignition events in combustion mixtures within combustors.

CHAPTER 1
INTRODUCTION AND BACKGROUND

1.1 Motivation

Efforts to increase thermal efficiency in modern turbine engine combustors, both for aviation and land-based power generation applications, have led to higher operating pressures, and thus higher pre-combustion temperatures. For example, in modern reheat combustors, inlet temperatures can exceed 1300K [1]. At such high temperatures, reactant can rapidly ignite without an external energy source and before interacting with a pre-existing flame. This type of ignition is commonly called autoignition.

Thus combustors that previously required pilot systems to stabilize and maintain a flame may now be operating in a region capable of autoignition-based stabilization. Augmentors and reheat combustors involve injecting fuel into high temperature, lean combustion products in order to extract additional thrust and power. This is commonly done using specific configurations of liquid fueled injectors and flame holders. The concept of afterburners without flameholders, utilizing autoignition and partial oxidation to stabilize combustion, has the potential to reduce engine weight and increase thermal efficiency [2, 3]. Staged injection in main combustors can also be used to meet performance and emissions requirements. Autoignition can play a role in the location and shape of the flame produced by secondary fuel injection systems.

While autoignition can be desirable, when it occurs unexpectedly in some regions of a combustor, it can be catastrophic. For example, Lean-Premixed Prevaporized (LPP) combustion is one approach to reduce emissions in liquid fueled power systems. LPP systems can rely on premixing fuel and oxidizer upstream of the combustor and generally seek to avoid the presence of autoignition due to its unpredictable nature, and potential to damage

or destroy hardware not designed to deal with the resulting high combustion temperatures. Thus introducing fuel into a high temperature mixing duct has the potential for safety issues due to the unpredictability of autoignition in a real system [4].

So depending on the configuration and circumstances, autoignition can either cause combustor stress by producing large amounts of heat release in undesirable locations or it can contribute to the proper operation of the combustion system if it were predictable and reliable. Thus being able to understand and predict the occurrence of autoignition is important to the design of modern gas turbine engines.

Non-premixed fuel injection and polydisperse sprays encountered in real combustion systems increases the difficulty of predicting spray autoignition. In a liquid fueled system, the time between fuel injection and autoignition consists of the time for primary (and potentially secondary) break-up, heat up and evaporation of the droplets, mixing the fuel vapor and oxidizer, and finally chemically reacting the mixture. With fast vaporization and mixing, the local mixtures can become too rich and/or too cold to support autoignition, depending on the proportion of characteristic times. In a polydisperse spray of a multi-component fuel, the interacting phenomena of fuel droplet evaporation, mixing, and chemical reaction occur simultaneously and non-homogeneously. Being able to accurately predict this complex autoignition behavior can play a key role in the design and performance of modern combustion systems.

1.2 Background

Autoignition is the process by which a combustible mixture undergoes a runaway chemical reaction, leading to ignition, without the aid of any external source, such as a spark, hot surface, or laser. Traditionally, autoignition is a fundamental parameter of a given fuel-air mixture, assuming that the mixture is uniform and has no interactions with its environment. The process is generally characterized with an autoignition delay time, defined as the time between when a combustible mixture is formed at its initial temperature and when ignition

occurs. The ignition delay time (t_{ign}) of a specific fuel and oxidizer is dependent upon the mixture temperature and the reactant concentration. Often this delay time can be modeled through a modified, global Arrhenius type equation,

$$t_{ign} = A[F]^a[Ox]^b e^{\frac{E_a}{R_u T}} \tag{1.1}$$

where $[F]$ and $[Ox]$ are fuel and oxidizer concentrations, respectively, P and T are initial mixture pressure and temperature, and E_a is the activation energy of the fuel. The exponents, a, b, and n are determined through experiments or reaction mechanisms. The effect of overall pressure is often studied and although not explicitly included in this Arrhenius definition it manifests through other terms, such as the concentrations.

This description of autoignition comes from simplified systems, such as constant volume reactors and homogeneous plug-flow systems. Thus, this autoignition analysis is ideal for modeling the chemical processes involved in elementary experiments, such as ignition of premixed mixtures in shock tubes, used to develop surrogate fuel mixtures, and understand or validate chemical mechanisms[5].

In a non-premixed, liquid-fueled system, the autoignition delay time will consist of both physical and chemical times, where the physical delay includes time to form a spray, evaporate, and mix with the surrounding oxidizer. So even though the traditional autoignition delay time is an important metric for validating chemical mechanisms and surrogate fuel mixtures in homogeneous mixtures, it does not fully represent the ignition physics of a realistic, liquid-fueled combustion system. Autoignition is most significantly affected by changes in temperature but can also depend upon changes in fuel or oxidizer concentration, pressure, and also physical changes such as droplet size and turbulence level, which are not represented in a simple, one-step, Arrhenius-type expression. In this study, and in agreement with most experimental studies on autoignition, the ignition delay time will be defined as the residence time between the fuel injector and the location of autoignition,

where the distance is converted to time with the flow velocity.

1.2.1 Prevaporized, Premixed Autoignition of Jet Fuel

Premixed autoignition studies have shown that the autoignition behavior of prevaporized, kerosene-type fuels, such as Jet-A, has three important temperature regimes. At both low and high temperatures, autoignition is exponentially dependent on temperature. In the median range, approximately 750-900K, a negative temperature coefficient regime exists[6]. Unlike in the other regimes, an increase in temperature can lead to an increase in the autoignition delay. In the high temperature regime, which is of primary interest in this study, changes in autoignition delay time due to increases in both equivalence ratio and pressure can be predicted using a power-law relationship[6]. However it may not fully encapsulate the underlying physio-chemical processes involved in non-premixed flows and especially the presence of a multi-phase flow that can significantly affect the chemical processes of autoignition.

1.2.2 Autoignition of Fuel Sprays

Autoignition of sprays involves the simultaneous breakup and atomization of the liquid jet, droplet heat up and evaporation, mixing with the oxidizer gas, and chemical reaction. The autoignition process for a single, large droplet located in a quiescent hot gas is illustrated in Figure 1.1. To start, the temperature of the droplet increases, mainly by conduction, increasing the vapor pressure of the droplet. At a sufficiently high temperature, the droplet evaporation rate becomes significant and the droplet begins shrinking. The evaporating fuel vapor diffuses into the oxidizer, and reactions can occur in the region where fuel and oxidizer have mixed. Eventually, the reaction rate exceeds a critical limit and thermal runaway leads to ignition and a subsequent self-sustaining flame surrounding the droplet [7].

Jet fuel is generally a complex blend of hydrocarbons, consisting of many components

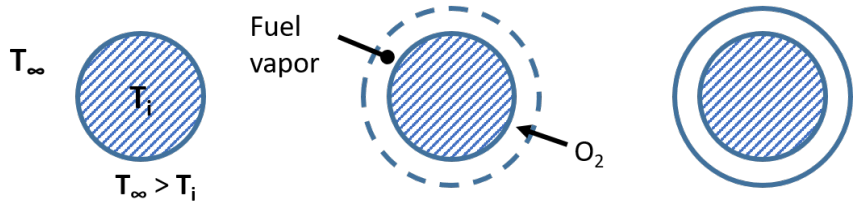

Figure 1.1: Illustration of the timeline of droplet autoignition. Reproduced from Reference [7]

[8], and its composition can vary with the constraint that specified physical and chemical properties of the fuel mixture lie within a specified range. Each of these components has different properties that can affect autoignition delay time and related properties, such as viscosity and volatility [9, 10]. All of these complexities can affect autoignition delay time of a realistic fuel spray through both physical and chemical processes. Due to the nature of droplet autoignition of a multi-component fuel, there are many local inhomogeneities that can affect the time history of any given autoignition kernel. It has been shown that preferential vaporization of multi-component fuels will have a significant effect on autoignition when the chemical time is comparable to the evaporation time [11].

The literature describes three possible methods of autoignition of a fuel spray: individual droplet ignition, ignition of a droplet cloud, or spray ignition; these are illustrated in Figure 1.2a [12]. Which type of autoignition method is present depends upon global and local flow conditions, and it can influence flame properties and subsequently, combustion performance. Furthermore, a study by Thibaut and Candel [13] found that there are two modes of droplet cloud autoignition. These two modes are determined based on the relative vaporization and mixing time scales and are illustrated in Figure 1.2b. If evaporation, and therefore cooling, is quick, ignition will initiate on the outer edge of the droplet cloud in the form of a diffusion flame. If cooling is not as drastic, ignition will occur initially in a homogeneous mixture inside the droplet cloud and then combustion will occur as a diffusion flame once the oxidizer inside the droplet cloud is consumed.

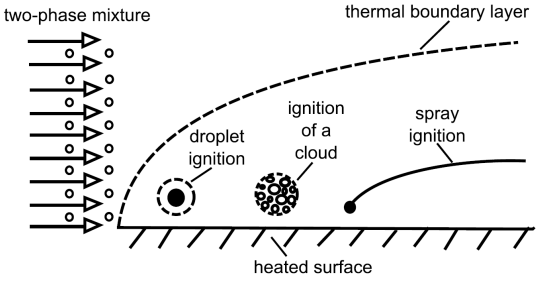

(a) Ignition modes of droplets described by Aggarwal [12]

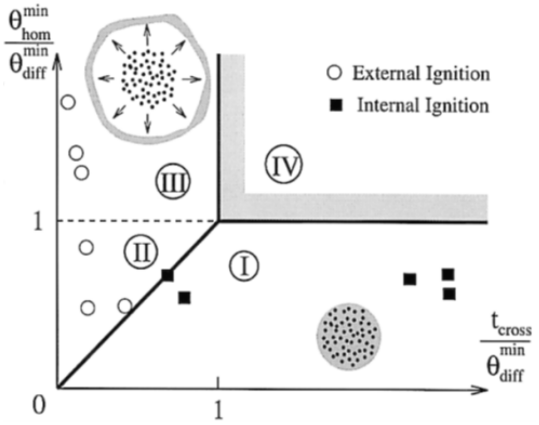

(b) Two ignition modes described by Candel [13]

Figure 1.2: Possible autoignition modes of two-phase flow predicted by theory

Single Droplet Autoignition

Single droplet autoignition has been investigated both numerically and experimentally [14, 15, 16]. For a given operating condition, there is a minimum droplet diameter below which autoignition cannot occur [14]. A single, cold droplet that fully evaporates before sufficient heat release has occurred may not autoignite if the mixture becomes too lean before thermal runaway occurs [15]. Law described two distinct regimes, or theoretical ignition limits, for single droplet autoignition: droplet-heating controlled and kinetically controlled [15]. In the droplet-heating controlled region, a cold droplet in a heated environment will autoignite as soon as enough vapor is evaporated to support the high temperature reactions. In the kinetically controlled region, a hot droplet in a colder environment would evaporate a significant portion of its mass thereby increasing the mixture temperature and initiating autoignition.

Both of these regions have a dependence upon droplet size: in the droplet-heating regime small droplets ignite sooner, whereas small droplets in the kinetically-controlled regime ignite slower or do not ignite at all. For less volatile fuels, heat up time is a more significant part of total ignition delay time. For single droplet autoignition, the location of autoignition occurs at a steady distance from the droplet at high temperatures and occurs

closer to the droplet at low temperatures [16]. Single droplet autoignition neglects the effect surrounding droplets in a spray can have on each other. Also due to the constrains of these previous experiments, droplets are generally much larger than what is encountered in real systems, the literature does not provide significant data on the effect of droplet sizes in the range of practical fuel sprays [16].

Droplet Interaction

The presence of other droplets can influence droplet evaporation and autoignition. Autoignition studies of cold droplet streams in a hot oxidizer have shown that there is an inter-droplet spacing that leads to a minimum ignition delay time [17, 18]. This behavior is attributed to changes in forced convection due to the presence of other droplets. As fuel loading increases (closer droplet spacing), the time necessary to heat the droplets increases, while the time to form a flammable mixture decreases. A more recent droplet stream study found that autoignition appeared in isolated spots that may correspond to evaporated fuel, and these droplet scale flames can collide and either merge or quench [19, 20].

For cloud ignition, an increase in cloud density requires more thermal energy to evaporate the droplets while the heat lost, proportional to the radius of the reaction zone, is higher for a single droplet than a cloud [21]. It has been shown that for very rich conditions, the droplets can completely evaporate before ignition occurs. At leaner conditions, cluster ignition occurs, and at even leaner conditions, droplets ignite almost immediately before much evaporation has occurred [22].

Parametric Studies

A number of previous studies have investigated autoignition of Jet-A and kerosene-type fuels, either prevaporized or in liquid form. These studies have reported the effects of pressure, temperature, equivalence ratio, turbulence intensity, and co-flow velocity on ignition delay time [23, 24, 25, 26]. Some of these previous results for near atmospheric pressure

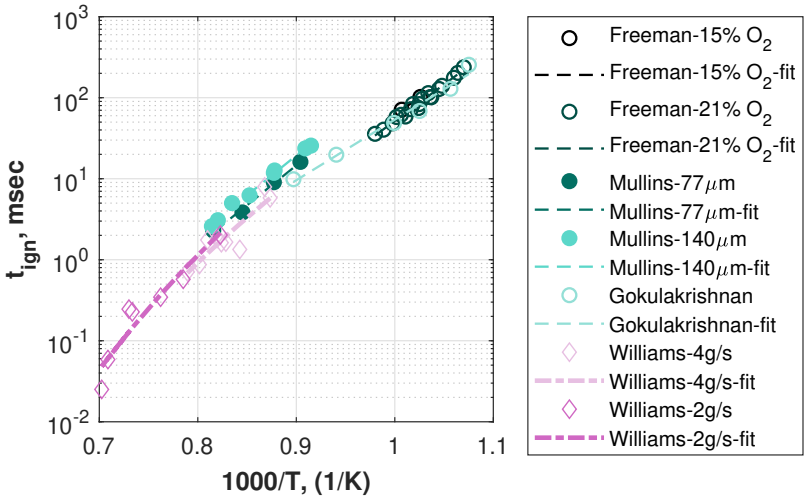

Figure 1.3: Ignition delay times reproduced from literature for vitiated, liquid fuel [23], and prevaporized Jet-A [25, 26] along with previous work by this author [27]

conditions are presented in Figure 1.3.

The experimental ignition delay times from Freeman and Lefebvre [25] and Gokulakrishnan et al. [26] are for prevaporized jet fuel mixed with preheated air in electrically-heated flow reactors. In [25], the authors studied Jet-A and also examined variations in the oxygen content of the air, while [26] used JP-8. Combined, their results cover the temperature range 930-1100K (1000/T≈0.9-1.08). Over this range, the delay decreases from nearly 300 to 10ms. The exponential temperature dependence of the ignition delay is evident in the nearly linear relationship between the log of the ignition delay and 1/T. Furthermore, even moderate temperature changes impact the ignition delay more significantly than changes in oxygen level (with lowered oxygen producing longer delays) or jet fuel type (at least for standard distillate jet fuels).

Mullins [23] and Williams et al. [27] report work for autoignition of (non-prevaporized) liquid fuel sprays in a vitiated flow. The liquid results are mostly at higher (flow) temperatures than the prevaporized studies, but show reasonable agreement in measured delay times. More specifically, they show ignition delay continues to drop at higher temperatures, below 1ms at the highest temperature (≈1430K). However, there are some important differences to note. First, the spray data from Mullins, which are for relatively large liq-

uid droplets, shows longer delays than the prevaporized results from Gokulakrishnan et al. at temperatures where data is available from both studies. Moreover, the delay increases more for larger droplets (reported values are Sauter mean diameters). On the other hand, the ignition delays of Williams et al., which extend to much higher temperatures than the previous studies, appear to decrease more rapidly with increasing temperature than would be expected from a linear extrapolation of the low temperature, prevaporized results. With regard to fuel-air ratio effects in ignition of multi-phase flows, Mullins found it does not have a significant impact on ignition delay, while others have reported both a decrease in the delay time [24] and an exponential increase at lean conditions [28].

Other flow conditions can also influence ignition delay. For example, the delay time generally varies inversely with pressure [23, 24, 25]. On the other hand, the delay time does not vary with flow velocity, it simply causes a change in ignition location proportional to the change in convective time, unless turbulence is significantly changed [23, 29, 19]. Turbulence has been shown to have counter effects on ignition delay time, due to changes in both the mixing and heat transfer rates [29]. As noted above, reduced oxygen content (common in vitiated systems) increases the delay, but the presence of NOx (also typical of vitiated systems) can reduce the delay time [30].

In summary, Arrhenius type expressions for ignition delay have been reasonably successful in describing its dependence on flow conditions, at least in simple flows. It should be noted, however, that these studies generally been based on spatially or temporally averaged measurements of both flow conditions and ignition delays. In a practical liquid-fueled system, the local conditions are no longer homogeneous or steady. Furthermore, these parametric studies do not contain sufficient details to fully explain the behavior of polydisperse fuel spray autoignition.

1.3 Local Autoignition

Previous parametric studies have shown that while average ignition delay times may agree with Arrhenius-type correlations, instantaneous autoignition kernels can vary greatly in ignition location due to the non-homogeneous mixture and stochastic history of fluid packets in a real flow. Studies of non-homogeneous, gaseous fuel have also shown that autoignition preferentially occurs in kernels [31, 32, 33, 34]. Autoignition was shown to occur in areas such as the wake of a jet-in-cross flow [32], and in the mixing layer of a jet in co-flow [33, 34]. A three-dimensional direct numerical simulation (DNS) showed that in non-homogeneous, gaseous, turbulent jets, kernels form in areas corresponding to vortically dominated regions of the flow [35]. Figure 1.4 shows the kernel expansion of a localized ignition event that begins in a flammable region of the fuel-air mixture of a co-flowing fuel jet in air. In this situation, ignition occurred in the small region designated as "1" in a flammable region between the stoichiometric and lean mixture fractions. The kernel expands as a turbulent flame into partially reacted regions that can experience a range of equivalence ratios due to the non-premixed nature of the flow and follows preferred mixture fraction regions upstream through the stratified mixture until it reaches a turbulent jet flame or lifted flame [36].

It has been shown that the mixture fraction, and the history of mixture fraction, experienced by a packet of fuel-air has an important role in determining reaction rates and therefore the likelihood of autoignition in a non-premixed gaseous system. In turbulent systems, the balance between scalar dissipation rates and the most reactive mixture fraction can control the likelihood of autoignition [36, 37]. The introduction of vaporized cold fuel to hot oxidizer causes opposing effects on reaction rate. Colder mixture temperatures will have lower reaction rates, but adding fuel concentration increases reaction rates. The regions of most reactive mixture fraction is determined based on both the fastest reaction rates and the least amount of cooling to the region due to fuel evaporation and mixing.

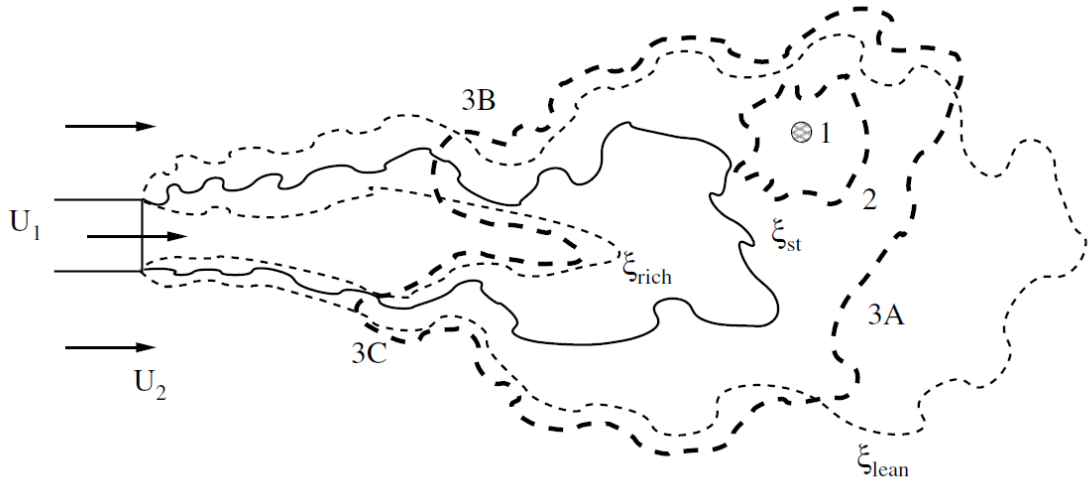

Figure 1.4: Kernel expansion of a localized ignition event where U_1 corresponds to a fuel jet in an air co-flow U_2, reproduced from Reference [36]

Given enough time, the flows will mix sufficiently in order to act as a premixed system, in which there is no longer a fastest chemical reaction rate. Figure 1.5 shows the physics of a gaseous, non-premixed fuel jet in co-flow. In the upstream region, where the fuel and air are mixing, autoignition event happen preferentially in most reactive mixture regions. Downstream, once the fuel and air have mixed more completely, the system begins to behave as a premixed system. In a liquid-fueled system, the region of most reactive mixture fraction will be more difficult to describe as it becomes more non-uniform than a gaseous system, but it is likely the same ideas will apply.

In predicting autoignition in multiphase flows, it is important to understand the role of the liquid spray in the development of kernels. Limited work has been done to investigate the behavior of local autoignition events in the vicinity of fuel droplets. A study of dilute sprays using high speed OH LIF and CH* chemiluminescence found that ignition kernels of OH initiate and grow on the outside edge of the droplet clouds, within a stabilization regime, with intensity increasing with distance downstream [38]. Using simultaneous OH PLIF and Mie scattering, with chemiluminescence, in a high pressure facility, Hinkeldey et al. found autoignition in random kernels that did not interact with residual droplets [39,

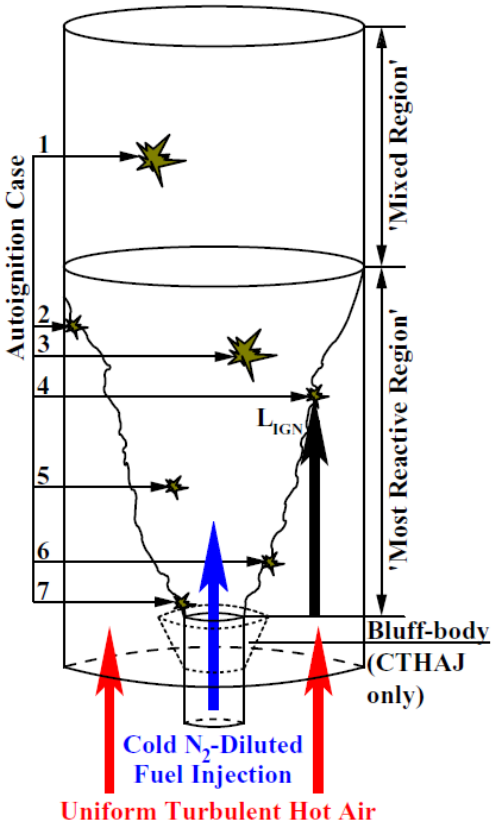

Figure 1.5: Modes of autoignition in a turbulent, non-premixed gaseous fuel jet in co-flow system, reproduced from Reference [37]

40]. They found no correlation between visible droplets and the reaction zone. However, examination of the resulting images suggests that their test facility consisted of a very dilute spray, unlike the conditions in many practical combustion systems. It is likely that their autoignition events did not interact with droplets because it was more closely described by the premixed region as illustrated in Figure 1.5. This study will investigate the behavior of autoignition in the presence of the fuel spray where droplets are more dense than in this previous study.

In summary, numerical studies have shown there are multiple ways for autoignition to occur in a polydisperse spray, such as single droplet ignition and droplet cloud ignition but this has not been sufficiently observed in an experimental system [13, 4]. Gaseous fueled non-premixed studies have shown the importance of most reactive mixture fraction in the statistics of autoignition kernels [36, 37]. Autoignition and droplet interaction in the presence of polydisperse sprays has not been sufficiently studied on a local scale at relevant gas turbine conditions and with more practical fuel sprays.

1.4 Goals of This Study

Based on this review, this thesis investigates the formation of autoignition kernels in the presence of a fuel spray using modern diagnostic methods in order to better understand when and how autoignition occurs in a liquid fueled combustion system at conditions relevant to a gas turbine combustor and augmentor. One objectives of this thesis is to provide an extensive data set on the statistics of autoignition kernel initiation in the presence of a polydisperse fuel spray in a well-characterized flow. Autoignition kernel locations are characterized on a statistical basis using multiple imaging methods in order to quantify the temporal and spatial nature of autoignition in a non-homogeneous, multi-phase mixture. Additionally the interaction of ignition kernels and droplets is investigated both qualitatively and quantitatively in order to understand which autoignition theories best describe the process in a real spray and if this changes with flow conditions.

1.5 Thesis Outline

Chapter 2 of this thesis describes the experimental approach for investigating autoignition and the modeling tools used for interpreting results. The experimental description includes details of the test facility, such as the fuel injector, piping and instrumentation. This chapter also describes the diagnostics used and methodologies for data processing.

Chapter 3 provides the results of the characterization of the flow in this test facility in order to better understand the conditions at which autoignition occurs. Co-flow profiles are presented and regions of interest are investigated further using higher resolution LDV and PIV methods. Fuel droplets are characterized using PDPA to measure the properties of droplets while PIV of fuel spray allows for viewing the streamlines of droplets in the two-phase flow region.

Chapter 4 first presents results from the entire combustion region as shown through high speed chemiluminescence. Next, the results of autoignition initiation locations and measured ignition delay times are given. Experimental results are compared to modeling predictions and differences are discussed and explained.

Chapter 5 introduces the fuel spray into the understanding of autoignition kernel locations. This chapter analyzes the presence or absence of droplets where kernels are initiated.

The results are summarized in Chapter 6, including the qualitatively observed behavior of autoignition kernels. The primary conclusions of the study are listed and the implications discussed. The final section gives recommendations for future work.

In the appendices, examples of autoignition kernels at the first appearance and in the next frame are shown for each flow condition using UV PLIF. Also the code to implement the droplet heat up and vaporization calculations are given in Appendix B.

CHAPTER 2
APPROACH

This chapter describes the methodology used to investigate the autoignition of polydisperse Jet-A sprays. The first section describes the test facility; its design was intended to achieve a reasonably uniform co-flow to provide the closest replication of a preheated plug-flow system with minimal flow disturbances due to measurements and fuel injection. The next section outlines the optical diagnostics, including high-speed laser-based methods, employed to characterize the facility and to investigate details of the autoignition. In addition, it provides details on the methods used to analyze the data. Lastly the modeling approaches used to interpret the experimental results are outlined. These include chemical kinetic simulations and models to predict droplet heat-up and vaporization time scales.

2.1 Test Facility

The experimental facility used for this study was designed to simulate important flow conditions in a jet engine reheat combustor. The facility operates at test section velocities up to 50 m/s and inlet temperatures up to 1400K. The facility (Figure 2.1) consists of a stagnation point, reverse flow (SPRF) preburner, dilution section, flow conditioning and measurement section, and transparent test section. The fully optically accessible test section allows for the use of many optical diagnostic systems including PDPA, LDV, both low and high speed chemiluminescence, OH PLIF and PIV.

A SPRF preburner (also denoted here as the vitiator) was used in this test facility as it can provide high combustion efficiency and good stability without employing swirl, which would represent a flow disturbance to the desired flow conditions. Figure 2.2 shows a cross-section of this preburner configuration with flow streams illustrated; the exterior tubing is not shown. Cold air was supplied from a 125 psig supply tank to the SPRF combustor at

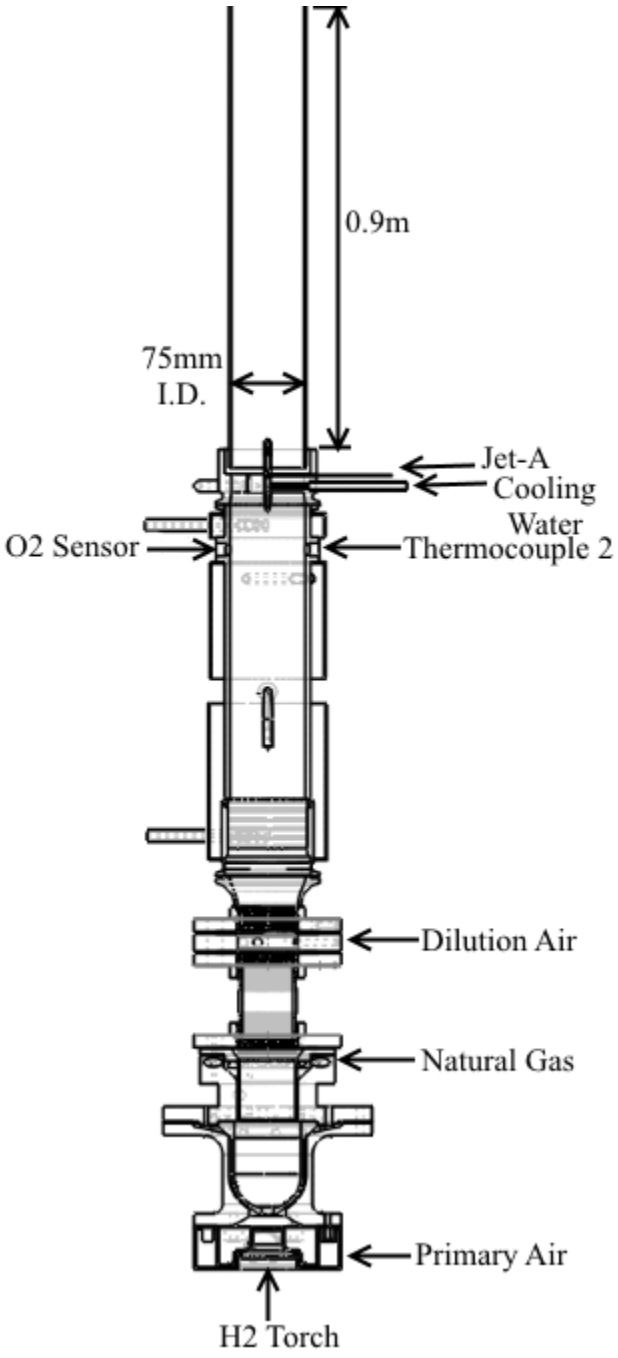

Figure 2.1: Schematic of test facility

the base, which then passed along the outside of the combustion can. This provided cooling of the combustor liner and also preheats the air flow leading to enhanced flame stability. Air is channeled through the outer tubing from the preheat region before being injected into the combustion chamber. Natural gas from a 32 psig supply line and the preheated air are injected radially inward in separate distributed jets. The mixture is then impeded by a cylindrical insert and forced down to the base of the combustor, where the flow must stagnate before reversing direction. This arrangement allows for a partially premixed gaseous supply to burn in a strongly recirculating flow, thereby creating a well-stabilized flame. A continuous spark ignitor with hydrogen purge was located at the base of the preburner. Cold, diluting air was introduced in the form of cross-flow jets just downstream of the vitiator to allow for control of the temperature and oxygen content. The total air flow to both the vitiator and dilution air was metered, so the split between the two is unknown. The split was occasionally changed to help with vitiator stability, meaning the split of dilution air is not necessarily the same between all tests. For estimating the actual temperature leaving the preburner, its operating equivalence ratio is important. The SPRF preburner operates poorly below an equivalence ratio of roughly 0.5, so this represents a minimum temperature condition. Since the air flow to the preburner was typically increased until stable combustion was achieved, it is unlikely that it operated anywhere close to a stoichiometric condition.

After the flows have mixed, a Haynes alloy perforated plate and ceramic honeycomb are used to create a more uniform velocity and dampen acoustic fluctuations from the preburner. The temperature and oxygen content of the vitiated air flow is measured just upstream of the fuel injection section using a shielded, non-grounded, K-type thermocouple and Bosch LSU-42, wide-band oxygen sensor. The oxygen sensor is installed along the wall to minimize flow disturbances while the thermocouple is installed slightly protruding into the facility to increase accuracy.

Fuel was initially injected using a commercially available pressure-swirl atomizer (Hago

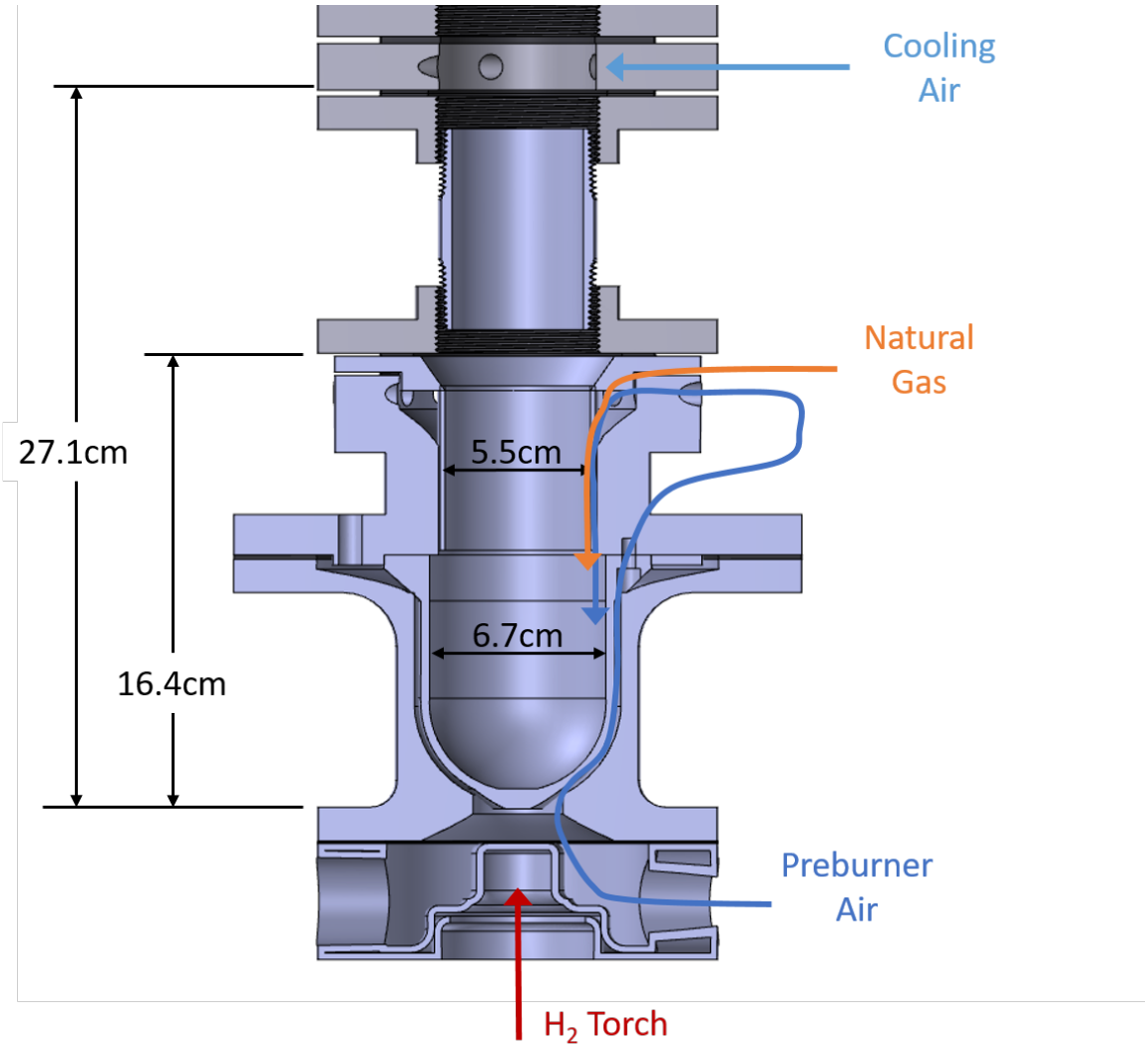

Figure 2.2: Zoom of SPRF preburner with flow streams illustrated

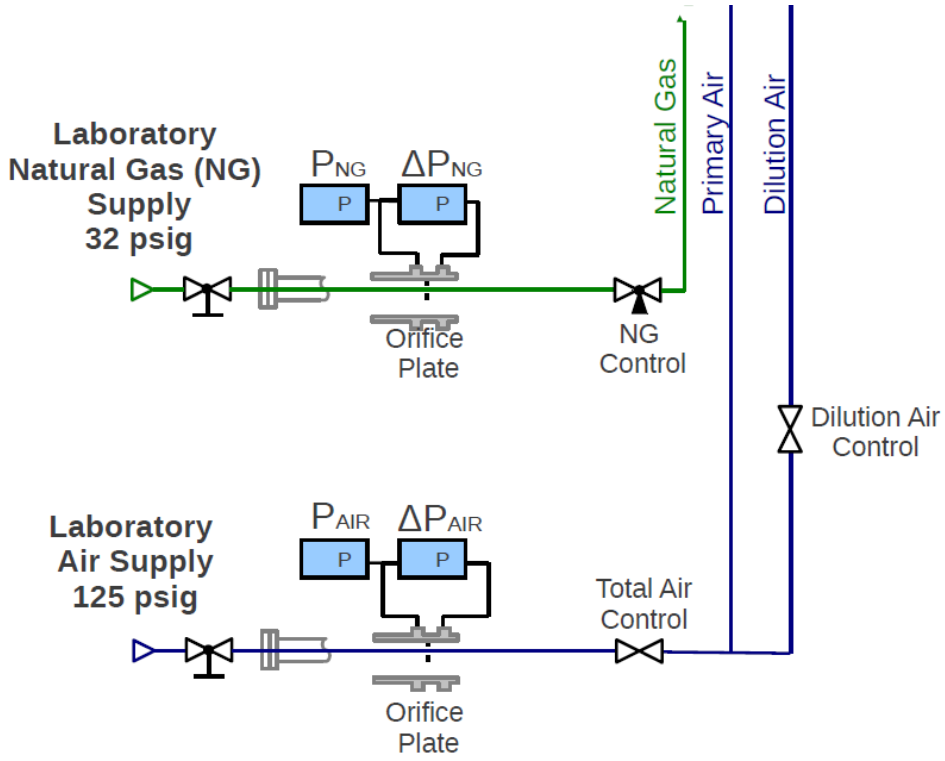

Figure 2.3: Schematic of supply line instrumentation

M2) installed in an aerodynamically shaped center body supported by three pylons. A second fuel injector, based on reverse engineering the Hago design, was fabricated in order to streamline the outer casing and make the injector more aerodynamic. The fuel spray was re-characterized with this design and additional spray and chemiluminescence data were obtained. This reproduction streamlined injector was used for all data that is part of this thesis. The injector body is designed to minimize flow disturbances while attempting to create a uniform spray throughout the test section. A detailed view of the fuel injector is shown in Figure 2.4. Jet fuel is supplied through a 1/16 inch (1.6 mm) stainless steel tube through one of the pylons. Cooling water passes through separate channels in each of the pylons to prevent coking of the fuel and increase injector life-time.

Injection caps can be added on top of the tapered fuel injector to change the flow in the wake of the fuel injector. Images of these caps are shown later in Chapter 3 along with their effect on flow velocity. Caps are held in place with a set screw during operation.

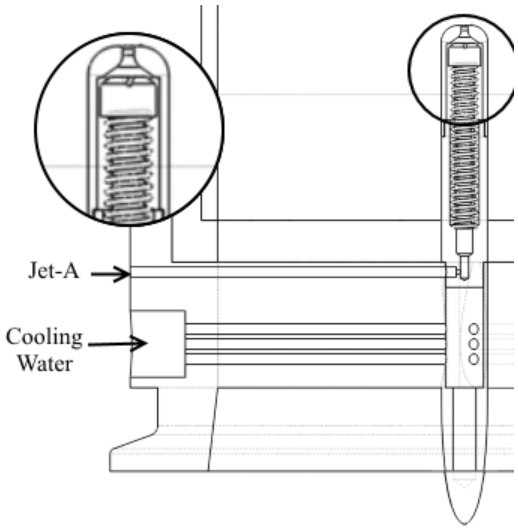

Figure 2.4: Zoom of fuel injection section

The test section consists of a fused quartz silica transparent tube with I.D. = 75 mm and 900 mm length. The lower end of the tube sits upon a shoulder of the injection section with a liner formed from graphite, and the upper end is supported by a metal band attached to the structure of the facility. The entire experiment is installed upon a three-dimensional traversing mechanism.

Liquid Jet-A fuel is supplied from a one gallon, double ended Swagelok DOT-3A1800 stainless steel high pressure cylinder shown in Figure 2.5. This cylinder is pressurized from the top with 150 $psig$ nitrogen. The bottom end of the cylinder is used for supply and refueling. Fuel flows through an Arrow, 25 micron, in-line filter before metering with an Omega type 9401 turbine flow meter connected to an FLSC-AMP Omega preamplifier and DP-F31-LIN Omega display with linear corrector and analog output to the computer before injection in the test section. A needle valve is used to control the Jet-A flow rate and a three-way valve switches the system from Jet-A flow to a nitrogen purge; this prevents the injector from clogging when fuel is not being injected.

The following relationships were used to determine the Jet-A equivalence ratio in a vitiated system. The vitiated stoichiometry is based on a mass balance when the stoichiometric

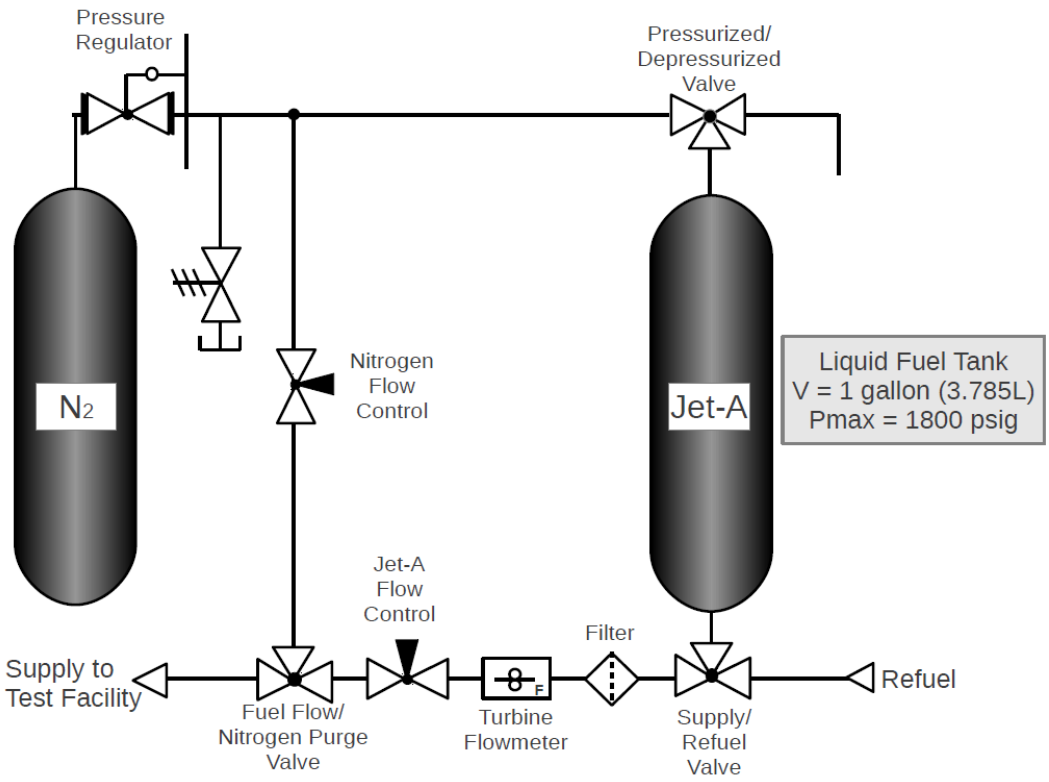

Figure 2.5: Schematic of the jet-A supply system

ratio of Jet-A with non-vitiated flow is 14.7:1.

$$\varphi_{Jet-A} = \frac{\dot{m}_{Jet-A}}{\dot{m}_{air} + \dot{m}_{Jet-A}} S \tag{2.1}$$

$$S = \frac{0.2095}{O_2\%} 14.2467 + 0.42281 \tag{2.2}$$

The facility instrumentation connected to a computer data acquisition system that operates at $10Hz$ with 11 channels for recording temperature, flow rates, and oxygen content. A LabJack was used to digitize the voltage signals from the various tranducers, and Labview was used to convert these signals to useful units in real-time and save the data for later use.

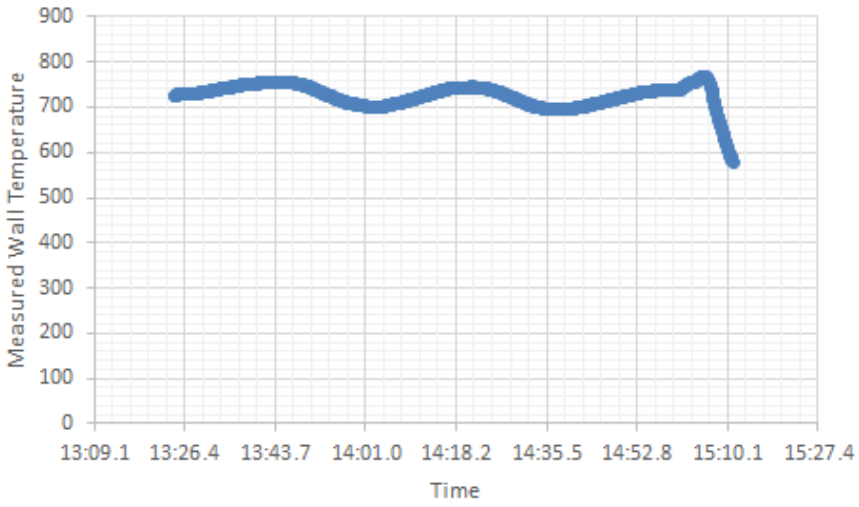

Figure 2.6: Time history of wall temperature for one OH* chemiluminescence test condition

2.1.1 Procedure

The standard operating procedure of the test facility begins with starting all cooling flows: air through the cooling jacked, water through the pylons and nitrogen through the fuel injector. Air flow through the vitiator is started at a lower than desired value, then the spark and then natural gas are added to the vitiator. Once the vitiator has ignited and successfully operated for a short time to warm up, the ignitor is turned off. The air and fuel flow rate to the vitiator are alternately ramped up until achieving the desired co-flow velocity and wall temperature. Figure 2.6 shows the time history of the wall temperature for one OH* chemiluminescence test condition. In this figure, the temperature is allowed to stabilize for nearly 2 minutes, with some adjustments to keep the temperature near the desired flow condition of $750°C$. The transients in the system temperature are slow showing a drift between 700 and $750°C$. The video was captured during the more level, $750°C$ portion of the time history before the temperature was quickly lowered during the waiting period to download the video.

Figure 2.7 shows the relationship between overall vitiator equivalence ratio, based on the measured methane and air flow rates (including dilution air), and the wall temperature,

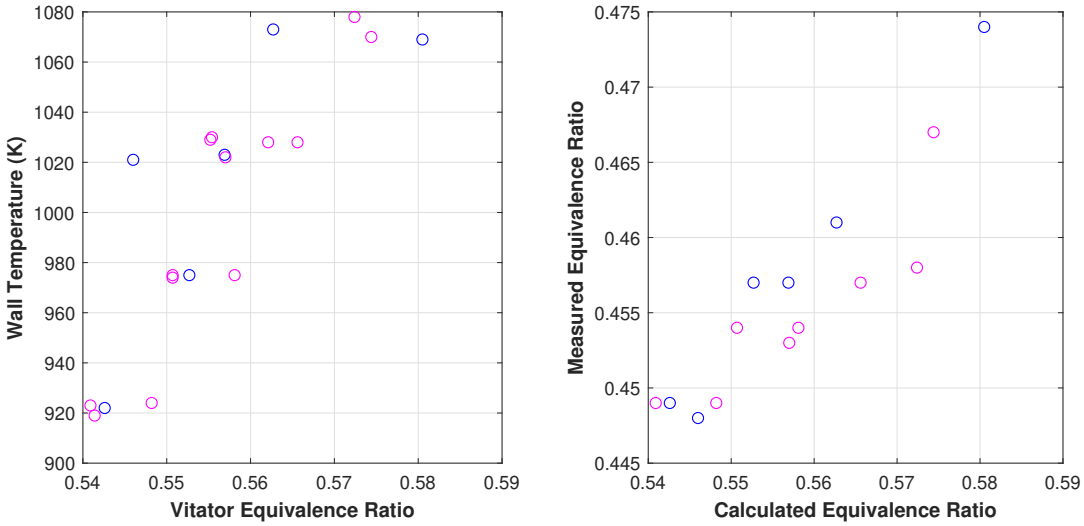

Figure 2.7: Measured wall temperature compared to measured vitiator overall equivalence ratio for OH* chemiluminescence high-speed data taken over two days - day one: blue circles, day two: magenta circles

measured by the thermocouple probe mounted nearly flush with the wall. The data was taken over two days, which are indicated by two colors in the figure. While there is scatter in the data, the general trend is as expected; as the vitiator equivalence ratio increases, there is an increase in wall temperature. The calculated vitator equivalence ratio based on the flow rates and equivalence ratio based on measured oxygen content also showed good agreement. Furthermore, the facility also produces similar results on the separate days, showing reasonable repeatability in the experiments. The scatter in the data is likely due to transients as mentioned previously, where the test facility had a slow drift in temperature due to the large thermal mass of the vitiator.

2.1.2 Temperature Correlations

The temperature of the co-flow was measured at the wall of the mixing section with minimal protrusion into the flow. Due to wall cooling, this temperature represents the coolest temperature in the flow. This will be further proven in the next chapter where the results of flow characterization will be shown. A correlation was made between the wall temper-

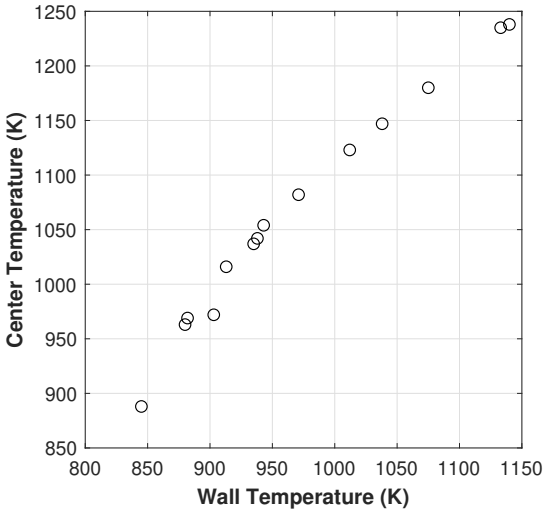

Figure 2.8: Correlation of center temperature (K) to wall temperature (K) used for this study

ature as measured during the experiments and the center temperature measured near the fuel injector. An example of this correlation is shown in Figure 2.8. The measured temperatures were corrected to correlate more closely with maximum center temperatures. In the region of relevant temperatures, this corresponds to an approximately $100K$ increase in temperature.

Additionally, these new temperatures were corrected for radiation heat loss from the thermocouple, further increasing the value for temperature. The temperature corrections are based on the heat transfer to a cylinder in a flow. Equation 2.3 shows an estimation for the Nusselt number for the cylinder.

$$Nu = \frac{hD}{K} = 1.13Re^{1/2} \tag{2.3}$$

The heat transfer is then given by equation 2.4.

$$hA(T_{gas} - T_{probe}) = \epsilon A\sigma(T_{probe}^4 - T_{wall}^4) \tag{2.4}$$

Over the range of $1012K$ to $1175K$, radiation correction adds $60K$ to $102K$, respectively.

2.2 Diagnostics and Data Processing

The fully optically accessible test section allows for the use of many optical diagnostics. These can be used to characterize and observe the fuel spray, or measure the autoignition locations and autoignition kernel evolution at varying flow conditions.

2.2.1 LDV and PDPA

A TSI, three component Phase Doppler Particle Analyzer (PDPA) and Laser Doppler Velocimeter (LDV) was used to characterize the fuel spray and air flow. The setup is shown in Figure 2.9. PDPA and LDV are non-intrusive droplet and particle velocity measurement systems. The two component and single component transmitters were positioned orthogonally, with the three component receiver located at 35° to the two component axis. The two component transmitter contains channel 1 and channel 2 , corresponding to the axial direction and +Y direction (defined by the traverse coordinate system), as shown on Figure 2.9, while channel 3 is the single component transmitter and corresponds to velocity in the +X direction. LDV operates in backscatter mode and does not require the receiver. Droplet size and velocity were measured in the fuel spray; seeding particle velocity and turbulence intensity were measured in the co-flow and wake of the fuel injector. Measurements were taken at increments of 1-3 mm at multiple planes downstream of the fuel injector for both "cold" and "hot" co-flow conditions. For LDV, an external low pressure seeder was used to provide seeding particles into the dilution air flow of the test facility. The seeding particles were 10 μm (nominal size) alumina particles. Due to the curved test section walls formed by the quartz tube, radial measurements did not produce a good signal when off the central axis. Axial velocity, data rate, and droplet size were all measured from the Channel 1 signal in the axial direction. The TSI Flowsizer software was used to collect and analyze the PDPA and LDV data and results.

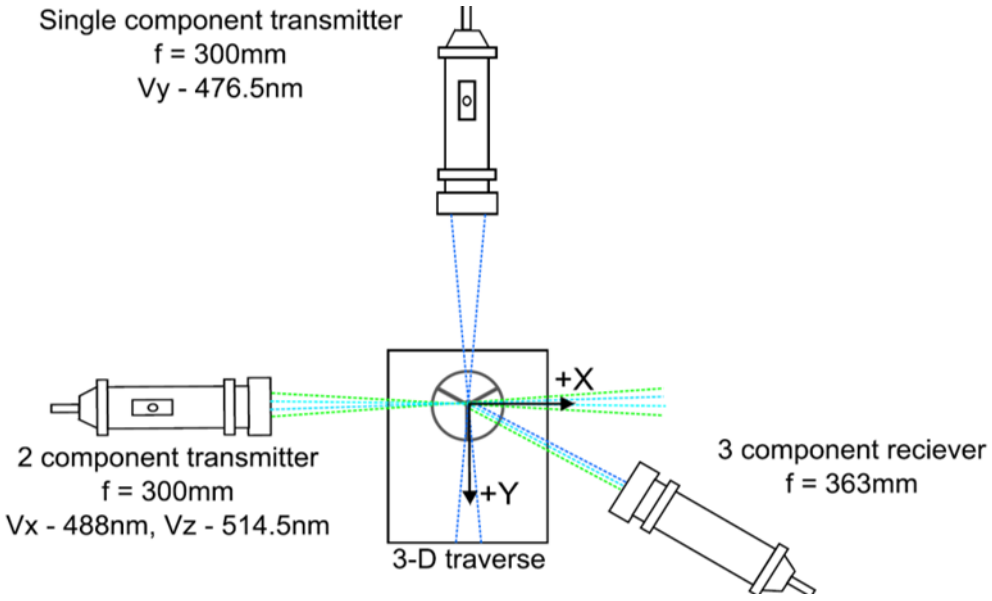

Figure 2.9: Illustration of PDPA and LDV setup

Table 2.1: Camera and intensifier settings for high-speed chemuliminescence

Radical	Camera	Intensifier	Gate (μs)	Gain
CH*	gx3-2224	VideoScope	20	650
OH*	gx3-1613	HiCatt	20	34000

2.2.2 High-Speed CH* and OH* Chemluminescence

High speed imaging of the autoignition process was used to characterize the dynamics of the ignition kernels. The entire test section was captured with a 144×1012 pixel resolution. A NAX GX-IR high speed camera equipped with a HI-Catt intensifier and 432 nm bandpass filter was used to capture CH* chemiluminescence, while a NAC GX-3 with VideoScope intensifier with 308 nm filter was used to record the OH* chemiluminescence. The two cameras were externally triggered using a waveform generator to capture simultaneous CH* and OH* signals at 5000 frames per second. Gate and gain information for both imaging systems are given in Table 2.1.

For each data set acquired with each injector, a calibration image of a printed grid was recorded with both cameras. These grid images allow for image registration in order to

align the OH* and CH* frames, as well as converting the results to physical distances in the test section. Image registration and subsequent data analysis were performed in Matlab.

In order to provide a statistically meaningful analysis of the formation of ignition kernels in this facility, each chemiluminescence image was interrogated to identify kernels. First, regions with ongoing combustion or heat release were identified by the existence of chemiluminescence; the chemiluminescence was differentiated from background and noise sources using a thresholding method. An example of this processing is shown in Figure 2.10; each frame is binarized based on a threshold value.

The binarized images allow us to calculate various statistics. For example, the intermittency is found by summing the binarized images and dividing by the total number of images. Thus the value at each pixel represents the fraction of time the corresponding (line-of-sight integrated) location contained a burning mixture. Note, the presence of chemiluminescence can correspond to kernel initiation, or to the growth and displacement of a kernel as it convects downstream. The binarized data can be used to identify kernel initiation and autoignition location based on the the most upstream position ("leading point") where chemiluminescence is found in each frame. Figure 2.10 illustrated the process with an example. Figure 2.10a contains the original image, while Figure 2.10b shows the binarized version with the most upstream location identified by the "+" symbol. Based on a complete sequence of such images, the axial position of the leading point relative to the downstream edge of the frame is shown in Figure 2.10c as a function of time. A sudden jump upstream in the axial position, which corresponds in the figure to a sudden increase in axial position, corresponds to the formation of a new autoignition kernel.

From such data, the average axial location (Y_{avg}), most upstream axial location (Y_{min}), and the corresponding standard deviation (σ_Y) were found for a range of flow conditions and four injector shapes.

The effect of threshold values is shown in Figures 2.11 and 2.12. The threshold value was varied from just under 12% of the maximum intensity possible, $2^{16} - 1$, to almost 24%.

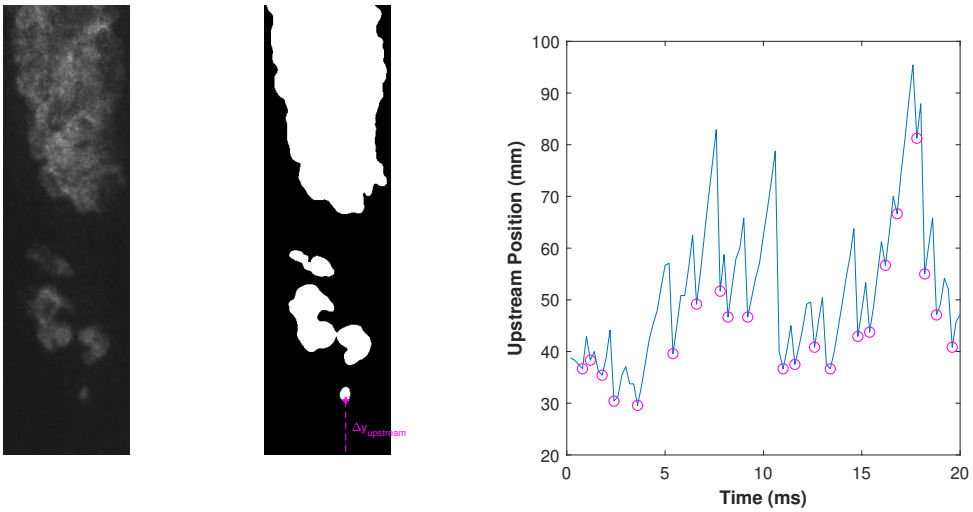

(a) Raw Image

(b) Thresholded image with upstream location shown

(c) Time History of Upstream Locations, Ignition Locations Identified

Figure 2.10: An example of OH* chemiluminescence image processing

Within a region of approximately 14 to 20% there is very small change in autoignition position. At values lower than this range the position jumps far upstream and values larger than the stated region the autoignition kernel itself is not detectable and the ignition location moves upstream to the larger flame structure. The value used for thresholding is shown in the figures as a magenta star. Using this value as reference, over the range 14 to 20% there is a range of error from -2.5% to 4.0% in axial autoignition location. For radial location, the value varies by -6.0% to 6.3%.

2.2.3 OH PLIF and Mie Scattering

Simultaneous OH PLIF and Mie scattering were used to visualize the autoignition kernels and fuel spray. The setup for these experiments is illustrated in Figure 2.13 A laser sheet was generated by a frequency-doubled, Syrah dye laser pumped by an Nd:YAG Edgewave laser at 532 nm. The dye laser was tuned to 283.95nm to excite fluorescence from the OH created by the combustion process which corresponds to the $A^2\Sigma^+ - X^2\Pi$, 1-0 transition [41]. The laser also excites fluorescence from some components of the Jet-A fuel; the

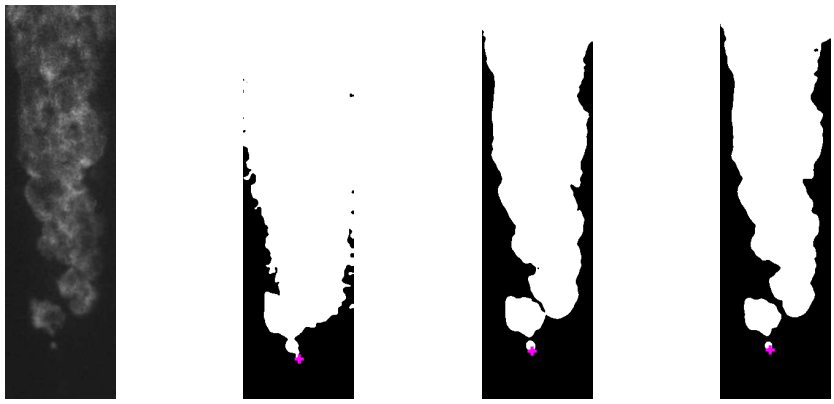

(a) Raw Image (b) Threshold = 30 (c) Threshold = 35 (d) Threshold = 40

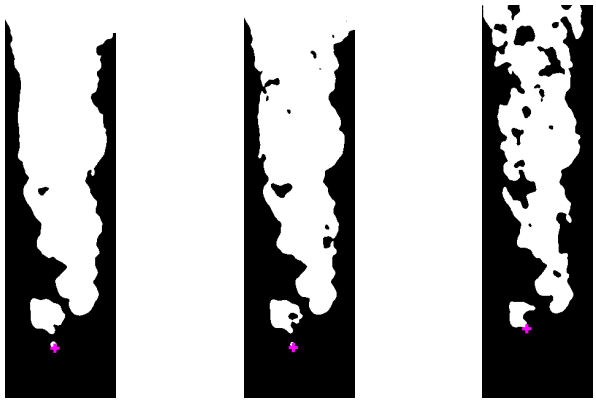

(e) Threshold = 45 (f) Threshold = 50 (g) Threshold = 60

Figure 2.11: The effect of threshold value on binarizing images

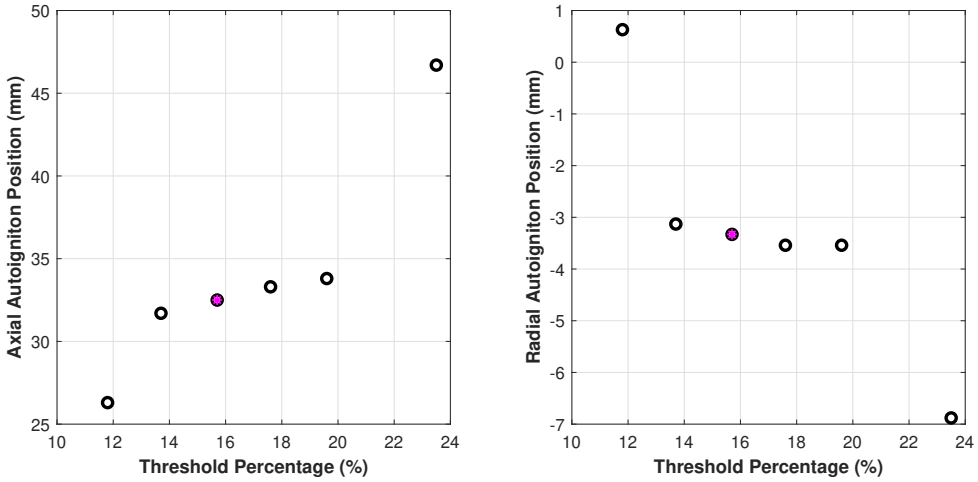

(a) Effect on axial autoigniton location (b) Effect on radial autoignition location

Figure 2.12: The effect of thresholding on autoignition position

fluorescence comes from the liquid fuel and potentially from the vaporized fuel, although this is less likely at high temperatures [42]. The fluorescence from the OH and fuel passed through a $308nm$ bandpass filter placed in front of a $45mm$ UV CIRCA lens. The lens imaged the plane illuminated by the laser sheet onto a gated IRO high-speed intensifier mounted on a Photron high-speed camera. The same ultraviolet (UV) laser sheet produced Mie scattering from the fuel droplets. Images of this elastic scattering was captured by a second NAC high-speed camera and HiCatt intensifier, equipped with a second $45mm$ lens without a filter. Images were acquired at a 5 kHz framing rate.

A plate with uniformly distributed dots was used to produce calibration images in order to align and de-warp the images from the two imaging systems. Image registration and processing was done using Matlab. Due to camera and lens choices, the OH PLIF camera was able to resolve more droplets in each frame than the Mie scattering images, so the Mie scattering images did not provide useful in analyzing the fuel spray.

The process to determing the autoignition kernel locations from the UV PLIF imaging is illustrated in Figure 2.14. In this process, droplets must be identified and eliminated in order to identify regions of light that correspond to OH from autoignition kernels. Fig-

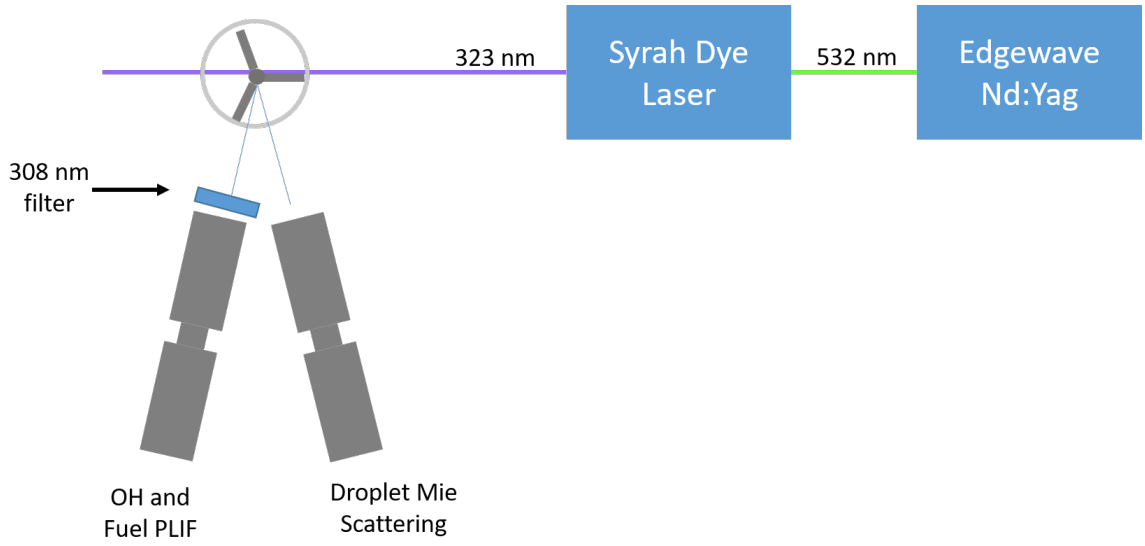

Figure 2.13: Illustration of OH PLIF and droplet Mie scattering diagnostics setup

ure 2.14a shows a raw image from one frame of UV PLIF. From each instantaneous PLIF image, the areas of light intensity were identified using image thresholding. For the OH PLIF images these areas of light were classified as (1) too bright to be an autoignition kernel and therefore is a droplet, (2) too small to be an autoignition kernel and therefore is a droplet or a new kernel indistinguishable from a droplet, or (3) a potential kernel. Figure 2.14b shows the resulting image when high intensity droplets have been subtracted. The remaining light is thresholded again with a lower threshold value and the largest structures are identified. Figure 2.14c shows the boundaries determined from the low threshold and the centroids of the five largest structures are identified. Note that the dark droplets were previously eliminated from this boundary analysis and show no boundary. The structures that exist distinguishable from the fuel spray near the injector are identified as a kernel and the centroid location and size of the structure were recorded.

Note that some large structures were identified near the fuel injector and these are most likely regions of fuel spray, not autoignition.

(a) Raw Image from UV PLIF imaging

(b) Image with high scattered light intensity from droplets removed

(c) Image with boundaries of structures and centroids of largest structures shown

Figure 2.14: An example frame processing for PLIF autoignition kernel locations

2.2.4 PIV

Particle image velocimetry (PIV) was performed using a LaVision system (Flowmaster Planar Time Resolved) consisting of a Litron LDY303He Nd:YLF laser with a $527nm$ wavelength, and a Photron high-speed camera with gated IRO high-speed intensifier. Results were obtained with an overall repetition rate of $5kHz$ and $5.08\mu s$ delay between pulse pairs. The flow was seeded with $5\mu m$ alumina particles using a passively agitated swirl seeder; additionally, depending on the configuration of a given experiments, fuel droplets are used solely for the velocity measurement or intermixed within the seeding particles. Air for the seeding particles was removed after flow metering and reintroduced into the dilution air.

Data was collected for spray only and co-flow only at the lowest temperature setting, and for both spray and co-flow over a range of temperatures. The simultaneous spray and co-flow PIV was performed in the reacting system. Spray only PIV was used to further investigate the behavior of the spray for different fuel injector shapes and to help elucidate the dynamics of the fuel spray in response to the dynamics present in the autoignition system.

2.3 Modeling

This section details the modeling approaches used to interpret the experimental results. A commercial software package (Ansys Chemkin) was used to simulate basic combustion processes: autoignition and laminar flame speed. A reduced order model was employed to predict droplet heat up and vaporization times.

2.3.1 Chemkin

Chemkin was used to model the test facility in order to calculate ignition delay times and laminar flames speeds for mixtures of prevaporized Jet-A and the vitiated oxidizer. The

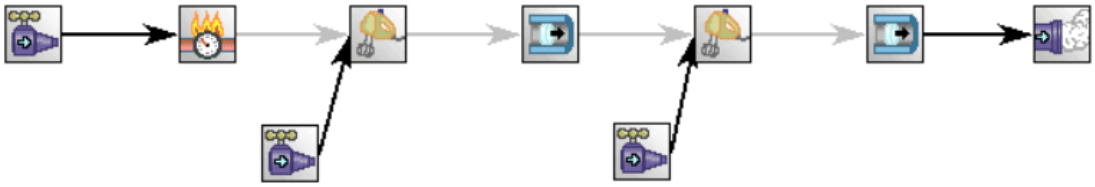

(a) Autoignition Calculation Model

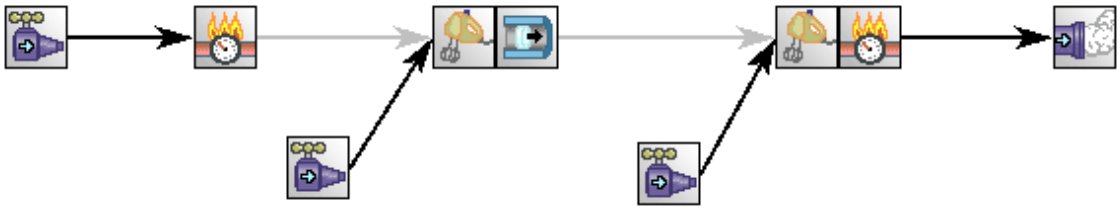

(b) Flame Speed Calculation Model

Figure 2.15: Diagrams of Chemkin Models

model was designed to best represent the experimental test facility and provide a high temperature vitiated flow, mixing section of cooling air, and introduction of Jet-A. The Hy-Chem mechanism, developed at Standford University, was used to provide the chemical rate information necessary to simulate combustion processes in both the natural gas pre-burner (vitiator) and the Jet-A fueled test section [43, 44]. This mechanism is based on the detailed USC mechanism, but uses a small number of pseudo-reactions to model the pyrolosis and partial oxidation of Jet-A, which is assumed to rapidly convert to a small number of other hydrocarbons whose chemistry is captured in the USC mechanism.

The model shown in Figure 2.15a uses a laminar flame speed block to model the pre-burner, with an inlet flow of stoichiometric CH_4 and air. The amount of air preheat achieved by the preburner design was not measured; inlet air was introduced to the preburner at $300K$. The overall equivalence ratio of the vitiator is also not known because the split of the vitiator air and preburner air was not metered. It is known from previous researchers that the SPRF vitiator would not operate at a fuel-air equivalence ratio less than 0.5. The vitiator residence time was estimated based on the volume, estimated average density, and mass flow rate from the experiments and was calculated to be on the order of 10-20ms.

With an inlet flow rate to the laminar flame speed calculator of $50g/s$, a length of $1cm$ will give the appropriate residence time. The equivalence ratio of the laminar flame speed calculator was set to $\varphi = 1.0$ and this results in an equilibrium flame temperature of $2200K$. Dilution air is added to achieve the overal equivalence ratio measured in the test facility via a non-reacting mixer. A plug flow section is used to allow for further reaction to investigate the effect of the mixing section on remaining radicals or achieving equilibrium. The residence time through the mixing section, based on the total length and average flow velocity is on the order of $10ms$ for the experiment and the length of the mixing plug flow is set to achieve the same residence time. Adding dilution air to achieve an overall equivalence ratio of $\varphi = 0.49$, results in a calculated temperature after dilution air of $1365K$. Heat loss is added to the mixing section in order to match the temperatures as measured in the test facility, ranging from a total heat loss in the mixing of 100-300K to get the maximum and minimum, respectively, measured temperatures of the test facility.

A non-reacting mixer allows for the addition of prevaporized Jet-A (HyChem A2 fuel) to the vitiated preburner products. Autoigniton of the resulting mixture is then simulated in a plug flow reactor. First the most reactive mixture ratio was determined at an intermediate temperature and high temperature by measuring the effect of Jet-A flow rate on ignition delay time. Then autoignition delay time was calculated for a mixture at the intermediate most reactive mixture fraction over a range of temperatures. Temperature to the plug flow reactor, represensting the test section of the actual test facility, was varied by adding a heat loss rate to the plug flow reactor representing the mixing section, such that all conditions have the same vitiated flow but at different temperatures. The autoigniton delay times calculated using this model should represent a limiting, fastest time, if the entire mixture of Jet-A was at a homogeneous temperature and most reactive mixture fraction.

An example profile of temperature, axial velocity, and mole fractions of O_2 and CO_2 is shown for this model in Figure 2.16. The first $1cm$ corresponds to the preburner, where temperature increases essentially to the adiabatic flame temperature of approximately $2200K$.

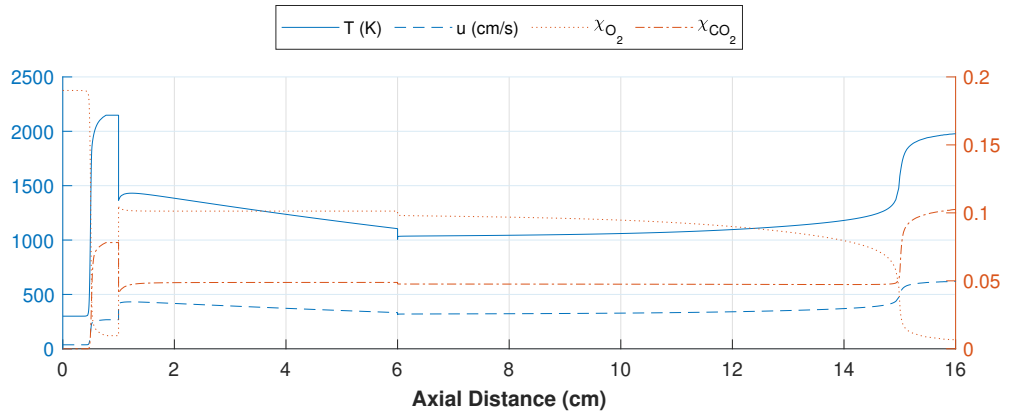

Figure 2.16: Example profile of Chemkin model for autoignition delay time at $1100K$, $\varphi_{Jet-A} = 1.0$ 0-1cm: Preburner, 1-6cm: Mixing section, 6-16cm: Autoignition section

Across the flame, there is a rapid decrease in oxygen and increase in combustion products as expected from a laminar flame. Dilution air is added to achieve a representative overall equivalence ratio as determined by the mass flow rates in the vitiator and dilution air. The dilution air quickly cools the flow to a temperature of about $1300K$, simultaneously raising the oxygen content of the flow. The products remain at equilibrium conditions for the 5 cm of the mixing section. A heat loss introduced into the mixing section to control the entrance temperature to the autoignition section and match experimental conditions. At x=6cm, the jet fuel is injected at $300K$. The model encorporates the cooling of the vitiated air flow due to mixing of the cold prevaporized fuel but does not allow for the extra cooling due to vaporizing the droplets. Based on the mass flows of vitiated air and liquid fuel in the experimental facility, it is estimated that it would lower the flow an additional 2.2K to vaporize the fuel droplets, which would have minimal effect on these results. This estimate is based on overall mixing, so locally could be larger in a region of concentrated vaporized fuel. This cold region would be unlikely to support fast autoignition chemistry and lead to an observable autoignition kernel. At 15cm, autoignition occurs for these conditions. The residence time at which the point of inflection in the temperature profile occurs was used as the ignition delay time. There is a more gradual initial increase in temperature and decrease in oxygen compared to the preburner region, though the formation of CO_2 is quite rapid.

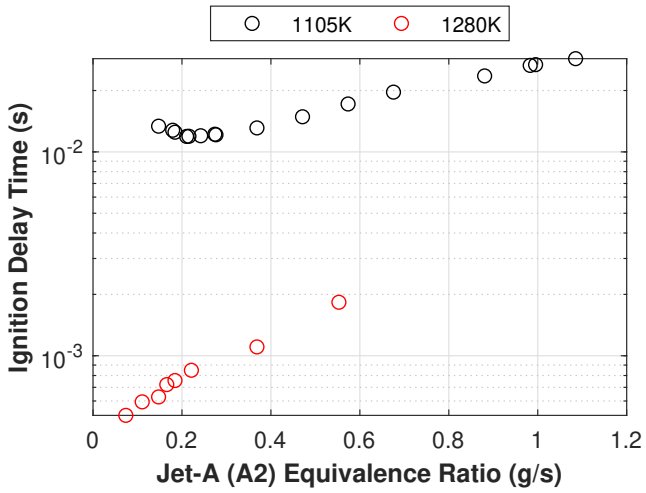

(a) Ignition delay as a function of equivalence ratio at two temperatures

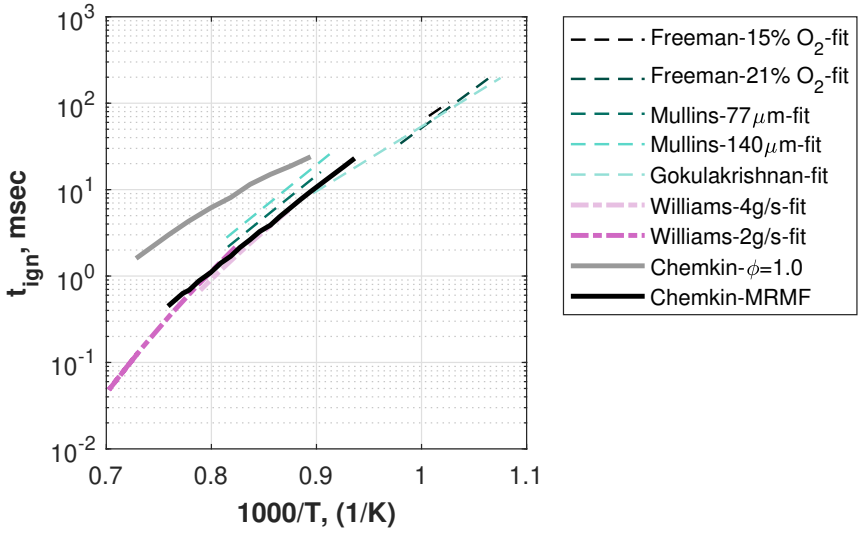

(b) Stoichiometric and MRMF ignition delay times compared to literature values

Figure 2.17: Equivalence ratio effect on modeled ignition delay time results

The effect of overall equivalence ratio was investigated using the Chemkin model. A cold gaseous flow of vaporized Jet-A was mixed with a heated co-flow over a range of lean equivalence ratios and the results are shown in Figure 2.17a. As overall equivalence ratio is decreased, the temperature of the resulting fuel-air mixture increases while reaction rates decrease due to lack of fuel molecules. At $1105K$ there is a distinct minimum in ignition delay time due to this balance of changing mixture temperature and reaction rate. At the higher temperature of $1280K$, there is no discernable minimum as ignition delay times continute to decrease with decreasing fuel flow rate. At such low fuel flow rates, the heat release produced is minimal and the location of autoigniton becomes difficult to determine. Using the equivalence ratio that produces a minimum ignition delay time at $1105K$ as the overall most reactive mixture fraction (MRMF) a series of ignition delay times were calculated over a range of temperature. The results are shown in Figure 2.17b along with modeled results at stoichiometric conditions and previouly measured ignition delay time values (the same values as shown in Figure 1.3). The MRMF model shows better comparison with experimental results than the stoichiometric ignition delay times. This is due to the reduced temperature caused by diluting the hot oxidizer with cold fuel. The MRMF and stoichiometric results approach the same value as the temperature decreases, i.e., as the flow temperature becomes closer to the cold fuel temperature. The good agreement between the MRMF model and the previous experiments likely results from the fact that the reported experimental values are based only on the hot gas temperature, neglecting any dilution cooling caused by mixing with the cold fuel. (Note this is not an issue for the premixed, prevaporized results of Freeman and Gokulakrishnan.)

A second model was used to calculate the laminar flame speeds of Jet-A at elevated temperatures. Flame speeds are useful for understanding the evolution of a kernel after ignition occurs, as we might expect its growth to eventually be controlled by the flame propagation process. Because experimental flame speed data is not available at the high initial temperatures investigated in the current work, we must rely on model predictions of

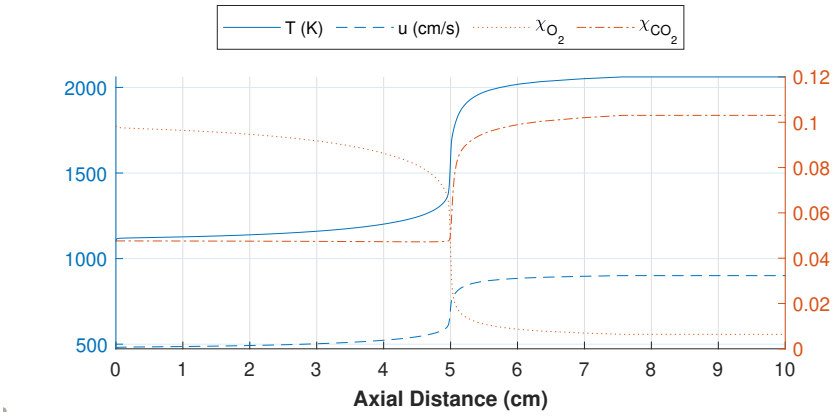

Figure 2.18: Example profile of Chemkin flame speed estimate at $1100K$, $\varphi_{Jet-A} = 1.0$, Only autoignition section shown

flame speed. In this second model, the preburner and mixing sections were kept the same as in the autoignition model, while the test section was changed to a laminar flame speed burner (Chemkin's Premix reactor). An example flame profile is shown in Figure 2.18 for an initial temperature of 1100 K. The behavior of temperature, reactants, and products looks as expected for a flame front. The effect of diffusion is seen slightly upstream of the flame with a small increase in temperature and small amount of oxidation started.

2.3.2 Droplet Heat-up and Vaporization Times

Droplet heat -up and vaporization times were calculated for ideal systems over a range of co-flow temperatures. The calculations are based the combination of methods first outlined by Sahzin[45], and Abramazon and Sirginano[46]. This method assumes spherical droplets. Furthermore, it assumes the thermal conductivity of the droplet is sufficiently high and the droplet is sufficiently small such that the Biot number is much less than unity. Under these constraints, the temperature will be uniform throughout the droplet, including at the droplet surface. Furthermore, the model assumes the fuel composition is invariant during the heat-up and vaporization process, e.g., there is no preferential vaporization of species.

The temperature history (heat-up) of a droplet under these conditions is described by

equation 2.5.

$$\frac{4}{3}\pi R_d^3 \rho_\ell c_\ell \frac{dT_d}{dt} = 4\pi R_d^2 h(T_g - T_d) \tag{2.5}$$

The mass of a droplet is represented by m, c_ℓ is the heat capacity of the liquid fuel, $\dot{m}$ is the mass evaporation rate, and L_v is the latent heat of vaporization, where the convective heat transfer coefficient can be written,

$$h = \frac{NuK}{L} \tag{2.6}$$

In these equations, d is the diameter of the droplet, T_g is the ambient temperature, k is thermal conductivity of the gas in which the droplet sits, and L is a characteristic length, defined as the ratio of the volume of the droplet to the surface area of the droplet (or R_d/6 for a spherical droplet of radius R_d).

This governing equation has a simple analytic solution that is valid if the transients experienced by the droplet are not significant. This solution is shown in equation 2.7.

$$T_d = T_g + (T_{d0} - T_g) e^{\frac{-3ht}{c_\ell \rho_\ell R_d}} \tag{2.7}$$

The Nusselt number is based on a model by Abramazon and Sirignano, which gives the following expressions:

$$Nu = 2\frac{ln(1+B_T)}{B_T}\left(1 + \frac{(1+Re_d Pr_d)^{1/3} max[1, Re_d^{0.077}] - 1}{2F(B_T)}\right) \tag{2.8}$$

where

$$F(B_{M,T}) = (1+B_{M,T})^{0.7}\frac{ln(1+B_{M,T})}{B_{M,T}} \tag{2.9}$$

Once the droplet has heated to the vaporization temperature of Jet-A, a d-squared law was applied to calculate the droplet lifetime for mass-transfer-controlled evaporation [47].

$$t_d = \frac{d_0^2}{K} \tag{2.10}$$

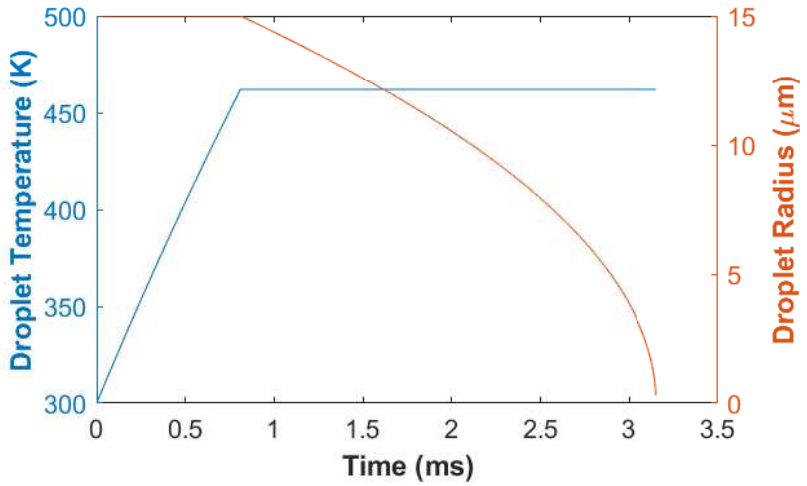

Figure 2.19: An example profile of a $300K$, $30\mu m$ droplet heat-up and vaporization in $1200K$ air with a $30m/s$ velocity difference

The evaporation constant, K, is described in 2.11

$$K = \frac{8k_g}{\rho_\ell c_{pg}} ln(B_q + 1) \tag{2.11}$$

This model uses constant values over the period of droplet heat-up and vaporization which oversimplifies the effect of changes of temperature and surface vapor concentration on the heat-up and vaporization rate but will provide a first order estimate of these characteristic times. The required fuel properties in these expressions are those of Jet-A when available, otherwise the properties of n-dodecane, a major constituent of most Jet-A fuels, was used. GasEQ was used to calculate average properties of vitiated air products at a range of temperatures and for each value a curve fit with temperature was used to calculate values at specific temperatures.

An example of the temperature profile calculated using this method is shown in Figure 2.19. For a $30\mu m$ diameter droplet with an intial temperature of $300K$ traveling at $10m/s$ in a vitiated air flow at $1200K$ and $40m/s$. The droplet heat-up time is approximately $1ms$ while the vaporization time is just over $2ms$, giving a total lifetime of just over $3ms$.

CHAPTER 3
CHARACTERIZATION OF TEST FACILITY

The test facility was characterized using multiple diagnostic methods; not only does this provide the necessary information to interpret the autoignition results, but it also facilitates future simulations of the experiments. Temperature and velocity profiles of the co-flow were measured along with velocity measurements in the wake of the fuel injectors. Droplet size, velocity, and density were measured using PDPA. PIV was used to measure the velocity fields of: the co-flow without the fuel spray operating, the spray (droplets) without co-flow seeding, and the gas and spray two-phase flow simultaneously. Finally, the particle Mie scattering field from the PIV setup is used as an indicator of flow uniformity.

3.1 Co-Flow Characterization

In order to determine autoignition delay times using the traditional method of convection time between fuel injection and autoignition locations, it is important to understand the flow field in this test facility. Multiple methods were used to validate the velocity measurements and wake properties of the different fuel injector shapes.

3.1.1 Co-Flow Velocity

The flow was first characterized using a combination Pitot probe and thermocouple $30mm$ downstream of the fuel injector. Velocity and temperature were measured at $1mm$ radial increments from the flow centerline to the wall; the results are presented in Figure 3.1. The velocity profile (Figure 3.1a) reveals a relatively uniform flow from the center axis almost all the way to the wall. There is a slight deficit (10-15%) at the center due to the wake produced by the fuel injector. There is a similar velocity decrease in the (unresolved) boundary layer along the outer wall. Temperature profiles are shown in Figure 3.1b for

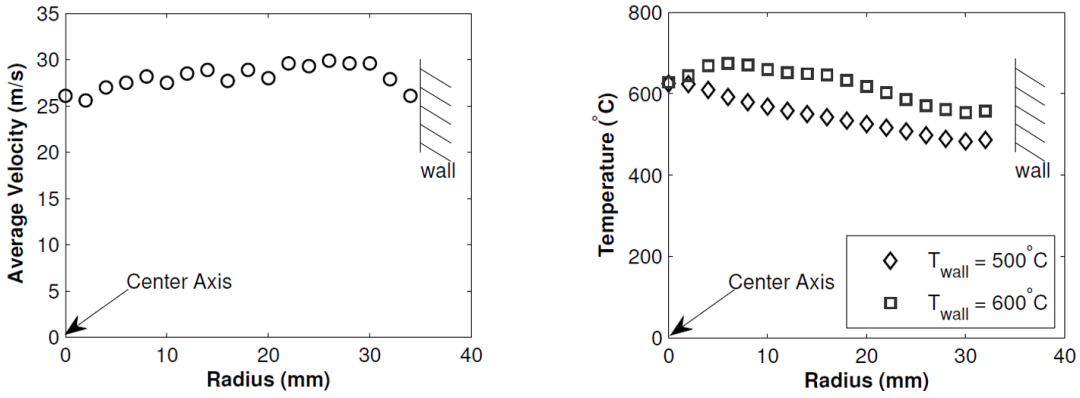

(a) Co-Flow Velocity Measured Using Pitot Probe at $u_{avg} = 38m/s,\ T = 1140K$

(b) Co-Flow Temperature Measured Using a Thermocouple at $u_{avg} = 28m/s$, $T_{wall} = 773K, 873K$

Figure 3.1: Radial profiles obtained using combined Pitot and thermocouple probe

two wall temperatures: 500 and 600°C. These temperature results are raw temperature data and have not had any corrections. These profiles are not used to correct the wall to center temperatures, only for visualizing the temperature distribution across the flow. These are lower operating temperatures than in the autoignition experiment so that a cooling nitrogen flow (replacing the fuel flow) through the nozzle was not needed as it would have disturbed both the velocity and temperature profile results. The radial profiles indicate a quasi-linear increase from a colder temperature near the wall to the maximum temperature location near the center of the flow. In both cases, this increase is approximately 100 K. For the colder case, the maximum occurs within 1-2mm of the centerline, while the maximum occurs roughly 5mm from the center for the hotter operating condition. This likely results from upstream heat losses to the fuel injector, which become more significant at higher flow temperatures. The temperature profiles show a need to correct temperature measured at the wall to a higher centerline temperature. Temperature data was recorded at the wall and one center location to determine a temperature correlation over the range of temperatures used in this thesis. In the remainder of the thesis, the temperatures reported will be corrected for centerline temperature and radiation loss. The temperature correlation was show previously in Chapter 2, Figure 2.8.

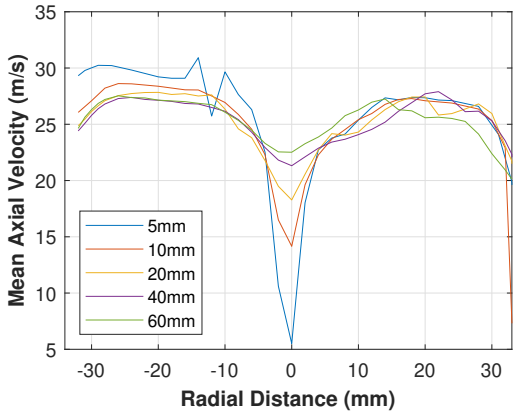

(a) Mean axial velocity

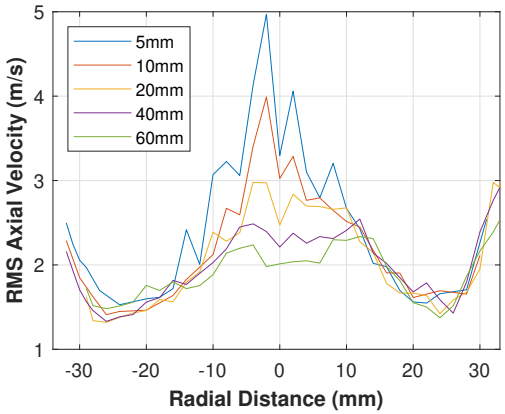

(b) RMS axial velocity

Figure 3.2: Mean velocity profiles through the centerline of the test facility at locations 5,10, 20, 40, and 60mm downstream of the tapered fuel injector, 710K, 28m/s, 11.5%O_2

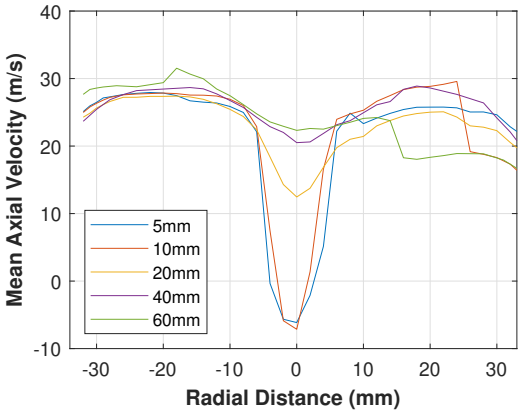

(a) Mean axial velocity

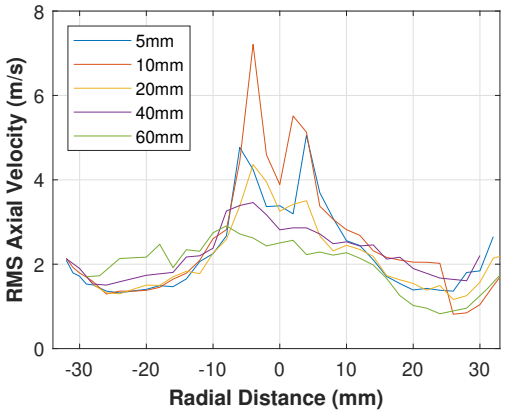

(b) RMS axial velocity

Figure 3.3: Mean velocity profiles through the centerline of the test facility at locations 5,10, 20, 40, and 60mm downstream of the blunt fuel injector, 700K, 30m/s, 11.4%O_2

Figures 3.2 and 3.3 show radial profiles of the mean and RMS axial velocities across the centerline of the test facility at axial locations 5, 10, 20, 40, and 60mm downstream of the fuel injector. These measurements were taken at lower temperatures in order to preserve the injector integrity without cooling air at the extended times required to obtain the data. The free-stream, injector wake, and boundary layer (on one side) features were captured in these profiles. Both injector shapes show a drop in velocity due to the wake of the fuel injector. The tapered shape has a minimum velocity of $6m/s$ at $5mm$ while the blunt shape has a recirculation zone present at 5 and $10mm$ with a velocity of -$7m/s$. The velocity fluctuation is larger in the wake of the fuel injectors. The tapered fuel injector shows a peak at the center of the flow, while the blunt shape shows two peaks, in the shear layer on each side of the recirculation zone. On average, the turbulence intensity is 5-10% in the freestream of the flow.

To better characterize the flow in the wake of the fuel injector, gaseous flow velocities were measured with a finer resolution in the wake region for each injector shape using LDV, with the flow seeded with alumina particles without fuel injection. The mean wake velocity contours, based on point measurements obtained for a grid of 2-3mm spacing, are shown in Figure 3.4, along with the images of the corresponding injector. Note that the injector images are not scaled to match the physical dimensions in the velocity graphs. For comparison, the width of the tapered fuel injector is 7 mm and the caps are $12mm$ wide. The contour of zero (mean) velocity is shown for each injector in green; inside of this boundary is a recirculation zone with negative average velocity. The tapered fuel injector has no measurable recirculation zone, which was the intent of its design. As the bluntness of the fuel injectors is increased, the wake becomes wider and longer, so the size of the recirculation zone increases. The recirculation zone width is approximately the width of the blunt downstream edge of the injector cap.

Figure 3.5a shows the mean cold flow velocity results from the PIV imaging. This image spans approximately $65mm$ of the $75mm$ inner diameter of the test section. The fuel

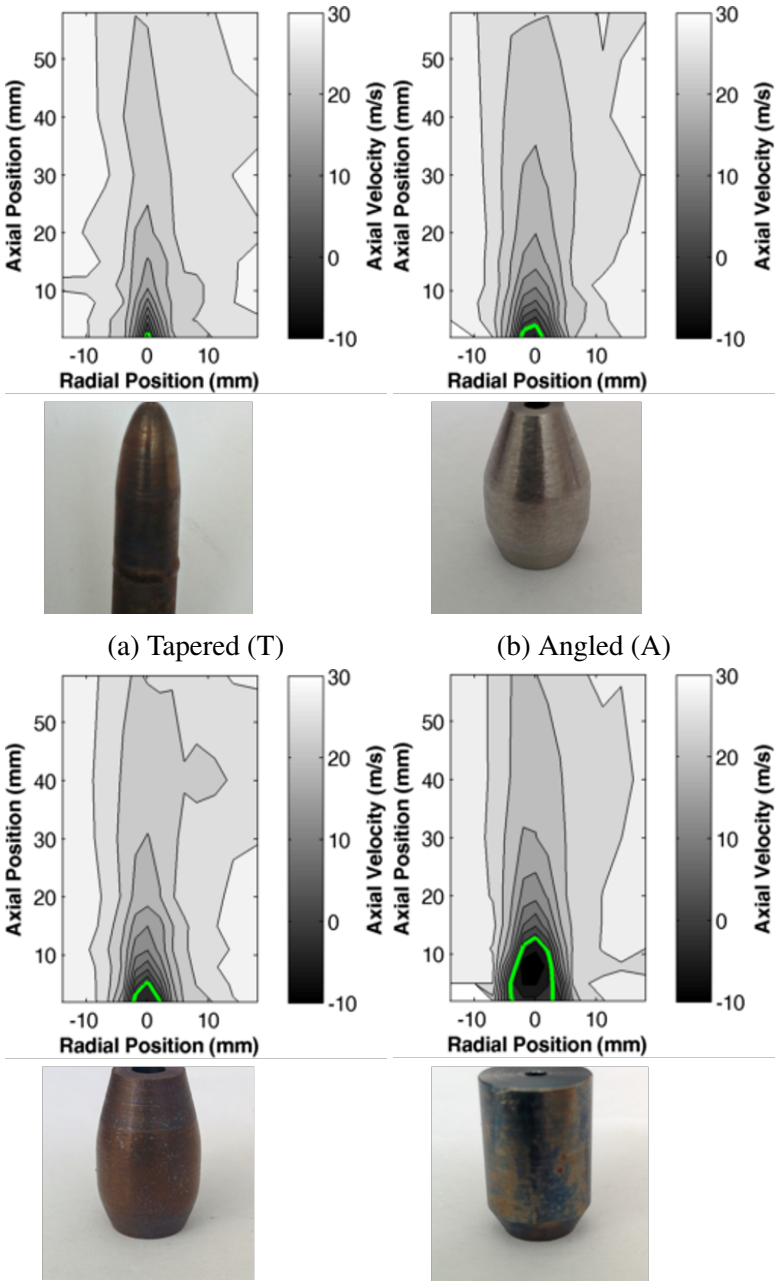

(a) Tapered (T)

(b) Angled (A)

(c) Chamfered (C)

(d) Blunt (B)

Figure 3.4: Co-flow velocity in the wake of various fuel injector shapes, $u_{avg} = 28m/s$, $T = 1143K$

injector is centered at the bottom edge of the image. The red box outlines the tip of the fuel injector and will be shown on processed PIV results throughout the chapter where the injector is not visible as a reference. For this test, the preburner was not in operation, only cold air was flowing through both the main supply of the test facility and dilution air sections, with seeding particles introduced through the dilution air. The air mass flow rate was kept at levels comparable to a burning experiment, so this results in a lower overall co-flow velocity. The results agree well with the LDV measurements, showing a wake in the immediate vicinity of the tapered fuel injector that narrows as it moves downstream. In addition, the velocity vectors show the flow is mostly axial; the regions with noticeable radial velocity (non-vertical velocity vectors) correspond to strong reflections from the cylindrical quartz tube (see Figure 3.5b), and thus the results in these regions are invalid.

Examples of instantaneous flow fields are shown in Figures 3.6 and 3.7 for the tapered and blunt injector shapes. Each figure shows four consecutive frames with instantaneous velocity vectors superimposed over velocity magnitude colormap. The tapered images show regions of low particle density where velocity could not be calculated as a zero or very low velocity region. Other then those regions, there are no observable regions of flow disturbances produced using this tapered, aerodynamically shaped center body. For the blunt injector shape, there are more observable wake disturbances and some small regions suggest circulating flow. It it possible that there are small vortices being shed from the blunt fuel injector.

3.1.2 Co-Flow Uniformity

Particle scattering images were also obtained for heated flow conditions, i.e., with the preburner operating, but without a fuel spray or nitrogen cooling flow. Consecutive raw images for a $1213K$, $44.1m/s$ flow with tapered fuel injector are shown in Figure 3.8, with only pre-processing performed to make the particles in the image more visible. These result indicate that the particles density is higher nearer to the walls. Additionally, there seem to be

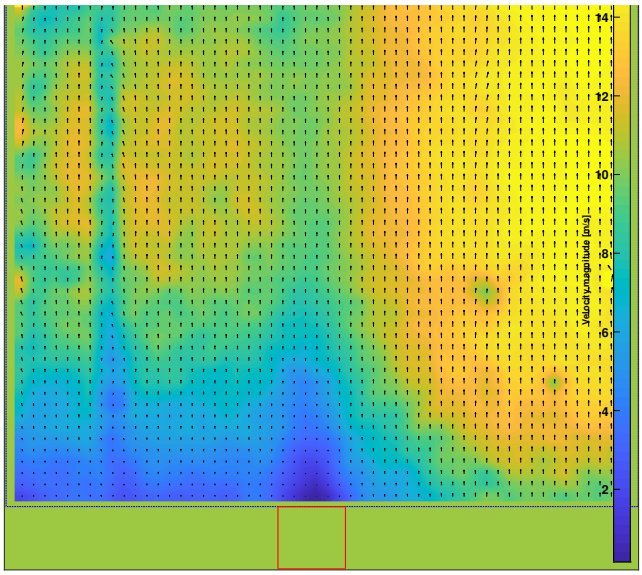

(a) Calculated flow field

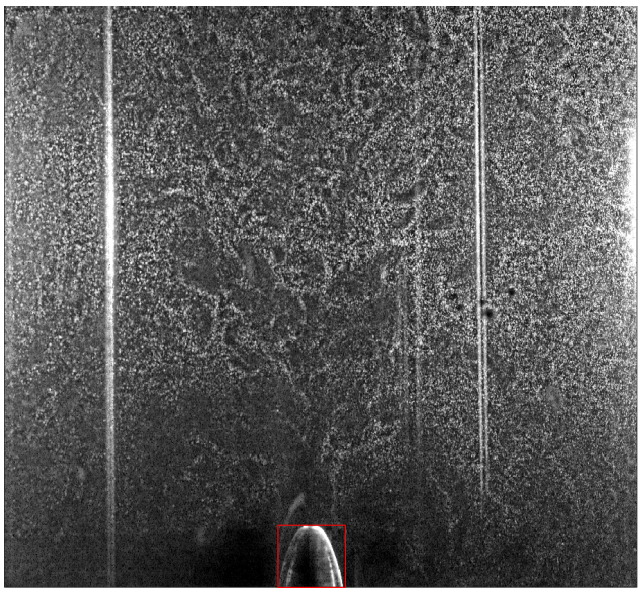

(b) Image with pre-processing applied

Figure 3.5: Cold co-flow results From PIV of tapered fuel injector, T=293K u = 12m/s

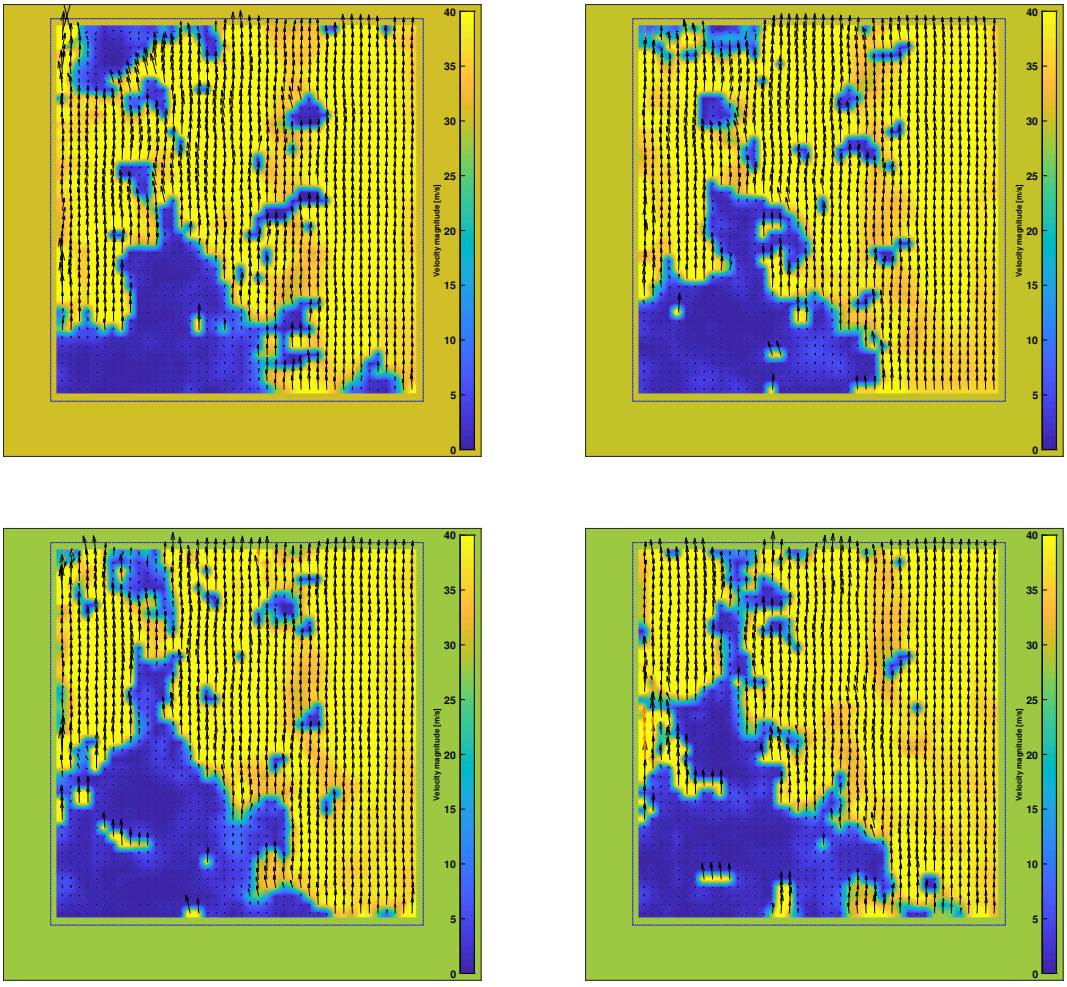

Figure 3.6: Example instantaneous flow fields from PIV using the tapered fuel injector at $1213K$, $44.1m/s$, 10.4% O_2

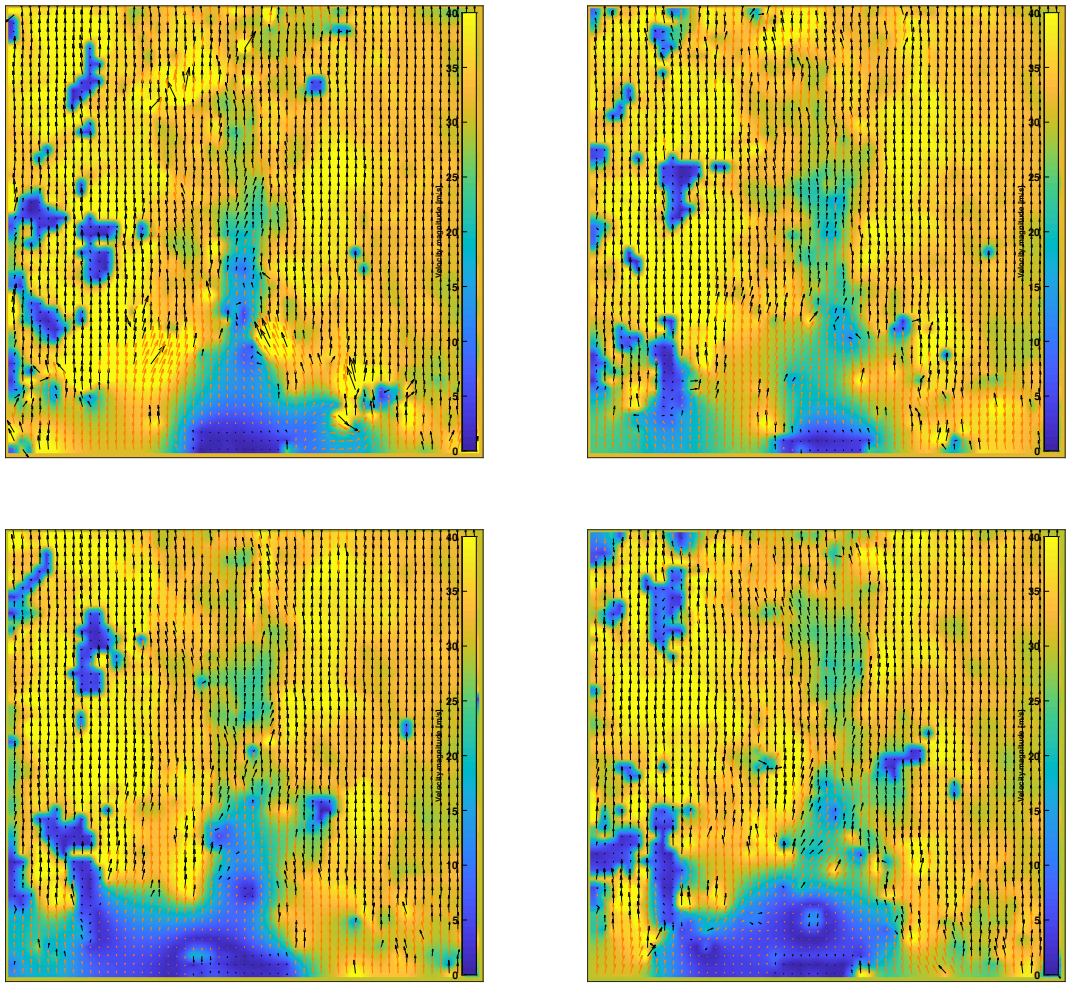

Figure 3.7: Example instantaneous flow fields from PIV using the tapered fuel injector at $1213K$, $43m/s$, 10.6% O_2

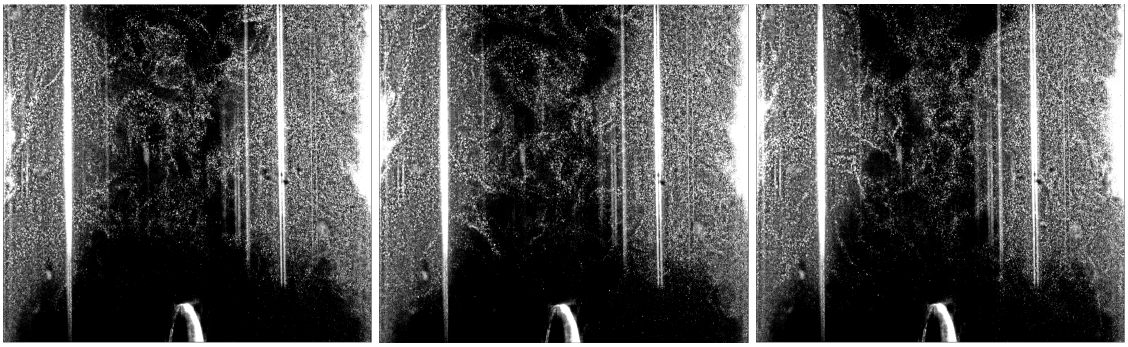

Figure 3.8: Consecutive images of PIV data with pre-processing to show particle uniformity, $1213K$, $44.1m/s$, 10.4%O_2

holes in the central region where with either there are no seeing particles, or their number is too low to produce a measureable scattering signal. The radial temperature profiles (Figure 3.1b) indicated that, on average, the vitiated air at the walls is cooler by at least $100K$. Therefore, we expect the gas (and particle) density to be $\approx$10% higher at the walls. The scattering images suggest the particle density difference is larger than this. As detailed in Chapter 2, the seed particles were introduced into the dilution air upstream of the dilution air plenum; they then passed through the plenum and the four dilution jets before mixing with the heated flow. If the seeding particles are uniform in the dilution plenum and dilution injection jets, these holes could indicate regions of the co-flow that have not mixed with dilution air. In turn, this would result in fluid pockets in the test section with much temperatures much higher than the average temperature, close to the exit temperature of the vitiator. An alternative explanation is the seeding particles are not uniformly mixed in the dilution air, either between the various jets or as a function of time during these tests. The scattering images from the cold-flow test (Figure 3.5) seem to indicate that when the vitiator is not in operation, the seeding is uniform. This suggests that the seeding density variation observed in the hot flow case is not due to poor mixing of the dilution jets with the pre-burner flow. However as noted above for the cold flow test, the air mass flow rate was kept the same as in the hot flow tests. Therefore, the flow velocity exiting the (unfueled) preburner was lower, and the momentum flux ratio between the dilution jets and the preburner exhaust would be higher for the cold flow case. This would allow a greater jet penetration and improved mixing for the cold flow case. The issue of temperature "hot spots" is investigated further in Chapter 4.

3.2 Fuel Spray Characterization

Fueal spray was characterized using PDPA to measure droplet properties and droplet Mie scattering to investigate any droplet response to flow dynamics.

3.2.1 Droplet Measurements

The fuel spray was characterized at 1-2mm increments along the X and Y, two orthogonal radial axes of the test facililty as defined by the axes of the traverse. Results are shown in Figure 3.9 for average flow conditions of T= 1171 K and u = 37m/s. The measurement locations are shown superimposed on a time-averaged UV PLIF image in the leftmost portion of the figure used to show an average image of fuel spray location. Measurements start just above the primary breakup region and end just before autoignition would occur in a heated system.

Results are shown in Figure 3.9 for the tapered fuel injector. The droplets in the center are the smallest, with an arithmetic mean diameter (AMD) near 12 μm. The large droplets are slung to the periphery of the spray where the average size reaches nearly 60 μm for the downstream measurements. The average droplet size, especially near the periphery, increases with distance downstream. This is attributed to small droplets evaporating quickly in the high temperature flow.

The droplet velocity profiles have a characteristic M shape; the velocity is low at the centerline, increases to a maximum a small distance off the centerline, and then decreases in the periphery of the spray. The most significant result is that the droplets are produced at a velocity well below the co-flow velocity, and they accelerate as they convect downstream. This can play a role in conversion to an appropriate convection time as the time fuel is spent as part of a droplet will be longer than what would be estimated using the co-flow velocity as the convection velocity.

The PDPA data rate (rightmost graph in Figure 3.9) can be used as a representation of relative droplet density since there is a low rejection rate of droplets in these measurements. The data rate drops with downstream distance as the droplets are evaporated and spread over a wider radial distance. A later chapter further investigate the behavior of droplets.

Figure 3.9b shows similar results for the blunt fuel injector. As a reminder, this is the same fuel injector, but with a blunt shape placed over it to change the (wake) flow field. The

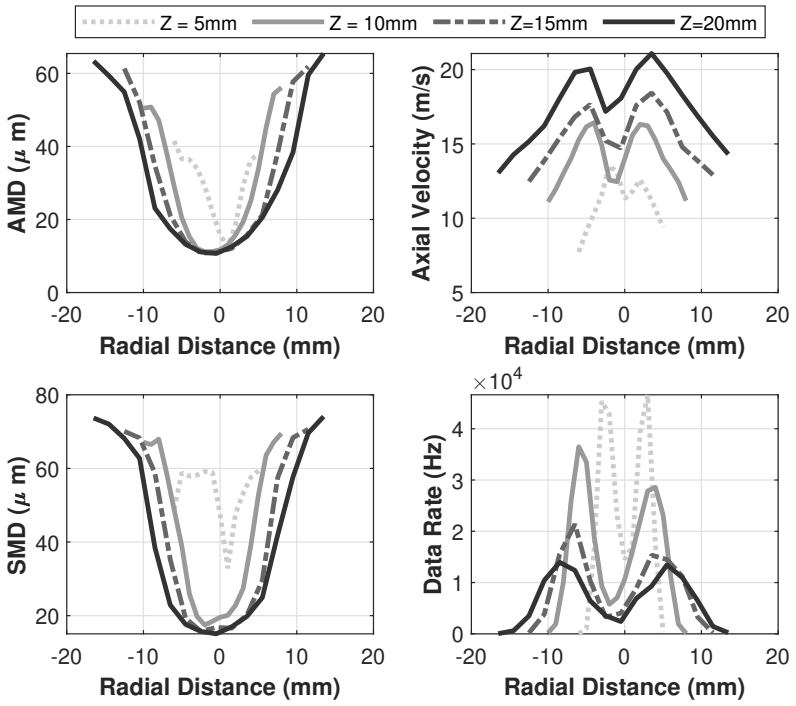

(a) Tapered fuel injector

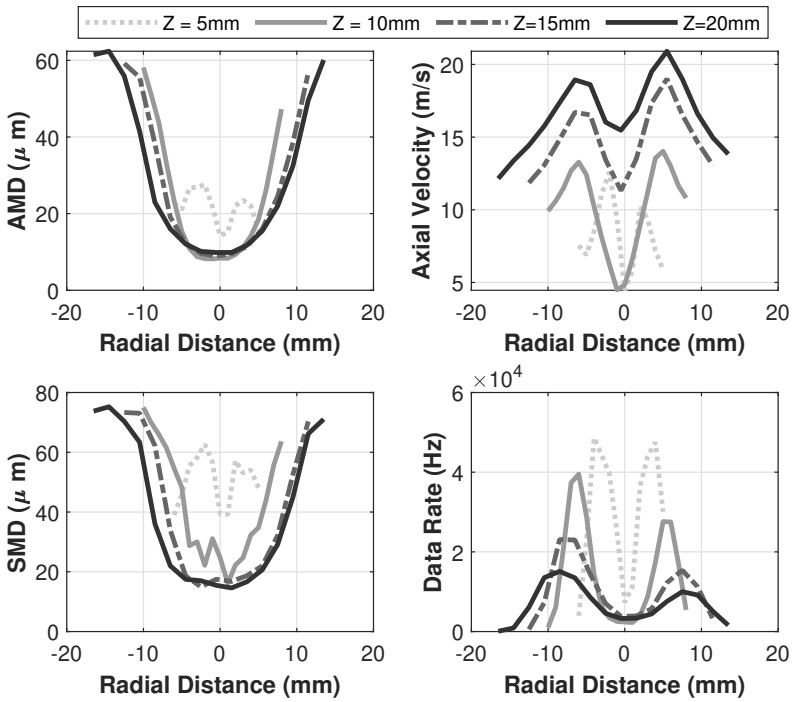

(b) Blunt fuel injector

Figure 3.9: PDPA measurements of droplet size (AMD), axial velocity, and velocity data rate at $u_{avg} = 37m/s,\ T = 1145K$

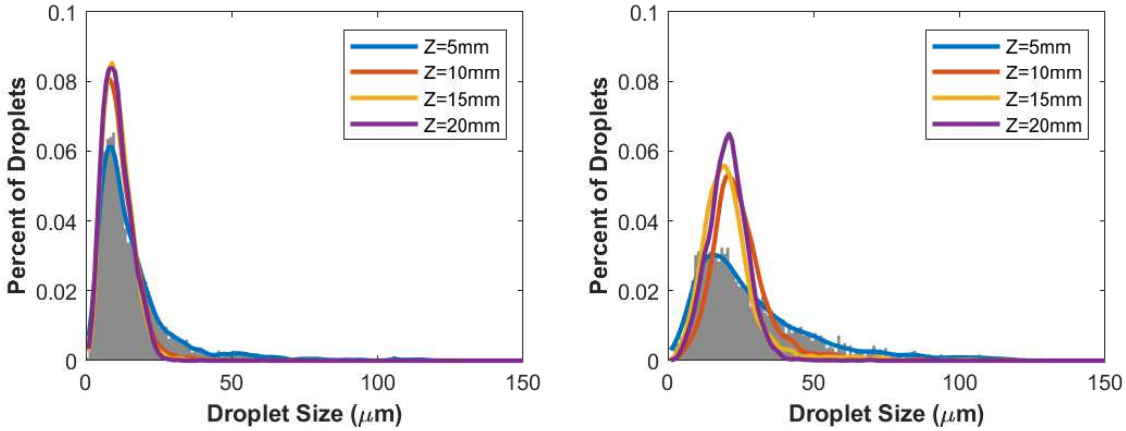

(a) Centerline droplet histogram

(b) Max data rate droplet histogram

Figure 3.10: A comparison of droplet size histograms for the tapered fuel injector, $u_{avg} = 37m/s,\ T = 1145K$

effects of this change are seen mostly in the region $5mm$ downstream of the injector, which from the LDV results would lie within the region of the recirculation zone of the wake. At this axial distance, the large droplets do not penetrate as far in the radial direction, so the maximum average droplet size occurs at a smaller radial distance from the center axis. The droplets also have a lower velocity when they are within the wake of the fuel injector, especially at the center axis, but eventually reach a similar droplet velocity to the tapered injector spray by 15-20 mm downstream of the injector. For the blunt fuel injector, this implies some of the droplets will experience longer residence times when observed at the same distance downstream as a droplets leaving the tapered fuel injector.

Droplet size histograms are shown along the streamline and along the maximum data rate streamline for the tapered fuel injector in Figure 3.10 and the blunt fuel injector in Figure 3.11. One example histogram is shown for the $5mm$ data set and the other data sets are shown only by the envelope curves for clarity. The bin size for the histograms is $1\mu m$ and the smallest droplet size measured is $0.5\mu m$. Along the centerline (leftmost graph) for both the tapered and blunt injectors, the droplet distribution starts narrow and stays narrow as the droplets convect downstream. Average droplet size here stays nearly constant with distance downstream, around 10-12μm at the centerline. At 5 mm, close to

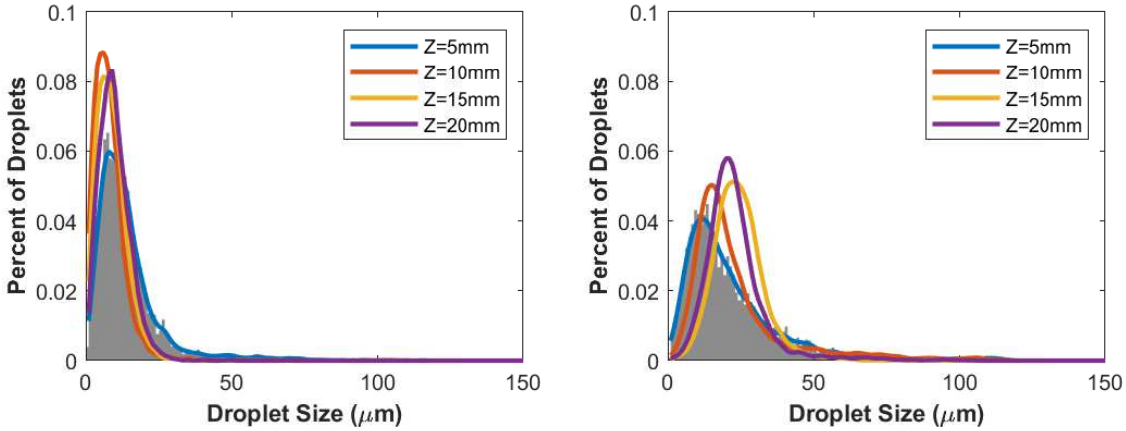

(a) Centerline droplet histogram

(b) Max data rate droplet histogram

Figure 3.11: A comparison of droplet size histograms for the tapered fuel injector, $u_{avg} = 37m/s,\ T = 1145K$

the fuel injector, there are slightly more droplets in the range of 20-50μm than at locations further downstream. These larger droplets are more likely to spread from the centerline due to their larger momentum.

The droplet histograms at increasing radial distance from the center show more spreading to larger droplet sizes. At the radial location corresponding to the maximum data rate, the histograms have 1.5-2 times more width. The largest droplet sizes observed range from 40μm furthest from the injector to 75μm near the injector for the tapered fuel injector, and a more uniform 50 μm maximum size for all locations for the blunt injector. The distribution of droplets narrows with distance downstream, again, most likely because the larger droplets have more momentum and are spreading outward. There are noticeably fewer small droplets in the range of 0.5-10 μm for the maximum data rate locations.

Using the range of droplet sizes as shown in the histograms and velocities ranges from the profiles at 5 to 20mm, the droplet Reynolds numbers were calculated. Along the center line, droplet sizes range from approximately 1 to 25μm, and average velocities range from 12 to 17m/s, corresponding to droplet Reynolds numbers on the order of 0.14 to 4.2. In the region of maximum droplet data rate where droplet sizes range from 1 to 50μm and velocities from 13 to 20m/s the values for Reynolds number range from 0.12 to 8.2. The

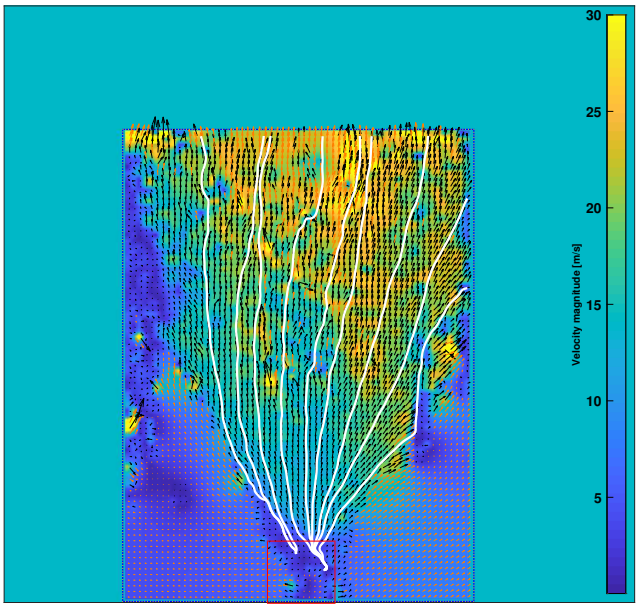

Figure 3.12: Calculated flow field of fuel spray at T = 1065K, u = 43.3m/s

smallest droplets are in the range of Stokes flow, while all droplets correspond to laminar flow.

The average spray velocity field, as determined from PIV of the flow with the fuel spray on and without seeding of the co-flow, is shown in Figure 3.12. The colors indicate velocity magnitude (with the color mapping shown to the right of the figure); velocity vectors and two-dimensional streamlines are superimposed upon the image. These results provide a more highly resolved droplet velocity field than was obtained through the PDPA measurements. Velocities calculations were isolated to the specified region of interest where droplets are dense enough to provide velocity vectors. In this image, the region of interest has total length in the axial direction of approximately 90mm from the fuel injector. The spray in this region is slightly asymmetric with a skew towards the right-hand side of the image. This was also evident in the PDPA results with slightly higher velocities at the positive radial dimensions. This may suggest some nonuniformity in the droplet velocities which could be caused by the fuel injector or co-flow nonuniformity. The right hand side

of the image should be in the wake of a pylon while the left half would be between two pylons. The velocity magnitudes show droplet velocities in the region of $5m/s$ at the exit of the fuel injector, which accelerate to 20-25m/s by approximately 30mm downstream of the injector. These results correlate with the PDPA results and show that past the region measured by PDPA the droplets continue accelerating, eventually reaching velocities near 30 m/s. Past this region of interest, the droplet Mie scattering density is decreased suggesting droplets have evaporated significantly.

3.3 Characterization of Combined Flowfield at High Temperature

Figure 3.13 shows the average flow field, as determined from PIV measurements, with the tapered injector and the preburner operating at a high temperature. The velocity field of the hot co-flow, without the fuel spray, is shown in Figure 3.13a, while the PIV results of the combined flow, with the co-flow seeded and the fuel droplets present, is shown in Figure 3.13b. As with the previous PIV results, the downstream tip of the fuel injector is located at the center of the bottom axis. The velocity magnitude is shown in color, with velocity vectors superimposed. It is expected that autoignition kernels would be present at these flow conditions. The bottom left hand quadrant of the image did not give expected results due to lack of seeding particles. From the right half of the image, it is clear that the co-flow velocity measurements are nearly uniform, around 35 m/s. There is a low velocity region visible in the wake of the fuel injector.

When fuel spray is added, the droplets dominate the velocity calculations in the region of dense spray, and the droplet velocity with the axial component is visible in the center of the flow. The presence of slower moving droplets expands the region of low velocity, both radially and axially, in the center where the fuel injector wake occurs. In Chapter 4, autoignition kernels are shown to begin around 20 mm downstream of the injector, thus droplet velocities rather than gas velocities likely provide a better approximation of the velocity experienced by a flow packet undergoing autoignition.

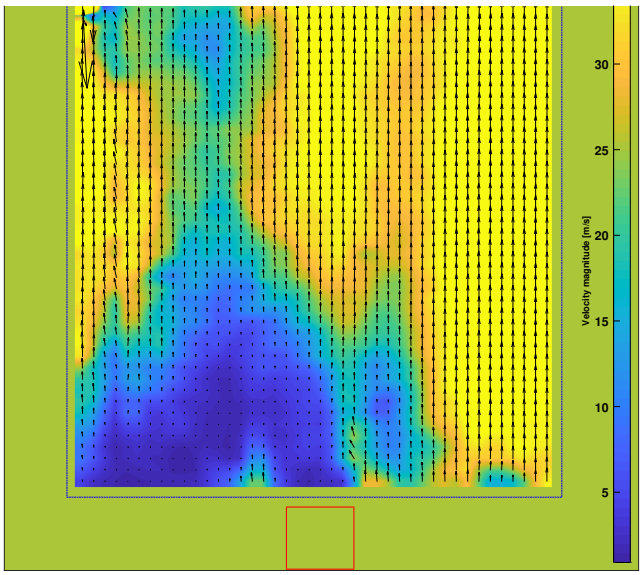

(a) Co-flow only, T = 1213K, u = 44.1m/s

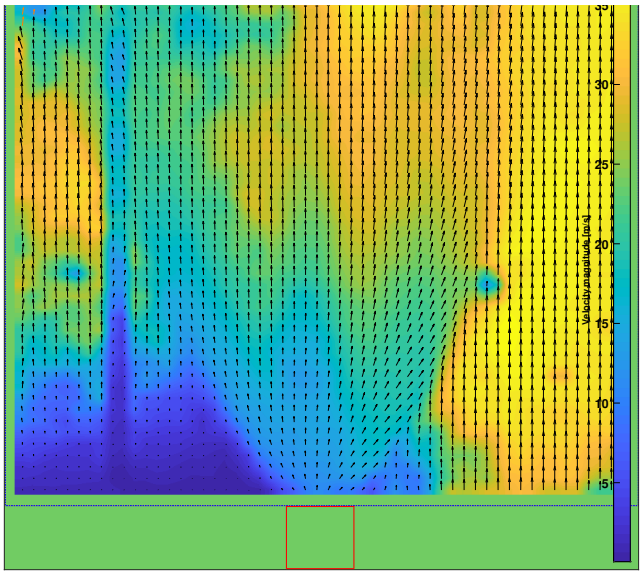

(b) Co-flow and fuel Spray, T = 1204K, u = 42.4m/s

Figure 3.13: PIV of flow using the tapered fuel injector

3.3.1 Summary of Flow Conditions

In summary, the flow conditions of the test facility were characterized using multiple diagnostic methods. Average temperature measurements show a linear distribution of temperature, with a maximum near the center and minimum at the cooled walls. If the seeding particles used for the PIV imaging are uniform, there is an indication that there are temporal fluctuations of temperature in the center of the test facility. The co-flow velocity was characterized with time-average Pitot probe techniques and high speed, higher resolution LDV and PIV laser diagnostics. The average velocity profile shows a uniform co-flow with a boundary layer at the wall. The LDV results show a wake in the center of the flow that increases in size as the injector shape widens, i.e., from tapered to blunt. The tapered fuel injector has no measurable recirculation zone and the blunt injector shape has a recirculation zone extending approximately 1.5 injector widths downstream. PIV results of the co-flow show a uniform co-flow velocity field, but in the presence of fuel spray, the droplets dominate the flow field and extend the low velocity region from just a wake to the entire dense regions of spray. Investigation of individual images suggests there may be non-uniformity in the co-flow. Droplet measurements show small droplet sizes in the center of the spray, with a low droplet density. The droplet size distributions in this region are narrow. Droplet size and distribution width increase as the radial distance from the center line increases, most likely due to the stronger outward momentum of the large droplets. PDPA and PIV measurements of droplet velocity show agreement and that the droplets continue to accelerate until droplet density decreases at which point velocity can no longer be measured. These results are used to inform the modeling and experimental interpretation found in later chapters.

CHAPTER 4
AUTOIGNITION BASELINE RESULTS

This chapter describes the results obtained for autoignition locations in the evaporating spray facility over a range of inflow temperatures and velocities and for injectors with different shape. As described in the previous chapter, the fuel spray produced by the injectors of different shape was similar except for changes in droplet velocity. The primary difference between injector shapes was measured to be different aerodynamic characteristics such as wake size and velocity profiles. In order to understand the statistical nature of the autoignition kernels in this poly-disperse spray, autoignition kernel locations were found using two high-speed measurement approaches: OH chemiluminescence and OH PLIF.

4.1 Results from Overall Combustion

Imaging results are first analyzed based on the entire combustion process using temporal analysis. The intermittency and time dynamics of chemiluminescence were determined for the tapered and blunt fuel injectors over the range of investigated temperatures. Additionally, autoignition was observed to have three distinct behaviors over the range of investigated flow conditions and these are discussed along with examples of kernel convection speeds.

4.1.1 Autoignition Kernel Intermittency

Figures 4.1 shows the intermittency results for both the tapered and blunt fuel injector shapes, represented by contours from 1 to 100%. The steps to determine intermittency values were outlined in Chapter 2 of the thesis. In summary, intermittency is used to represents the percentage of frames (or time) at which each pixel contains light above a determined threshold. This light can be produced by any combustion, not solely autoignition.

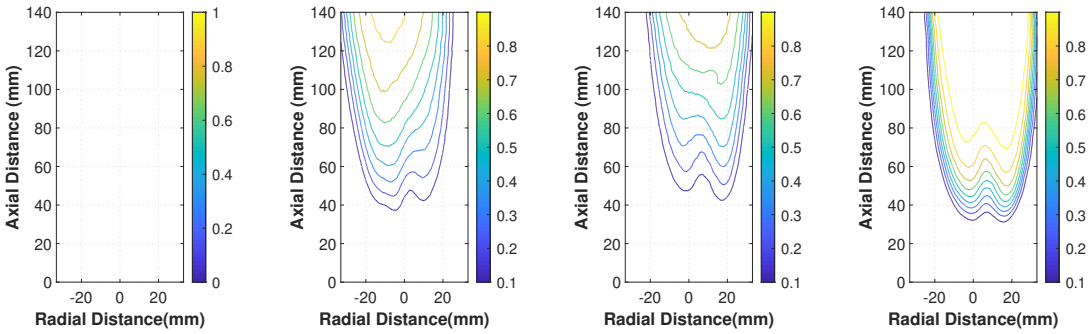

(a) 1061K, 41.7m/s (b) 1145K, 42.2m/s (c) 1212K, 40.0m/s (d) 1270K, 41.3m/s

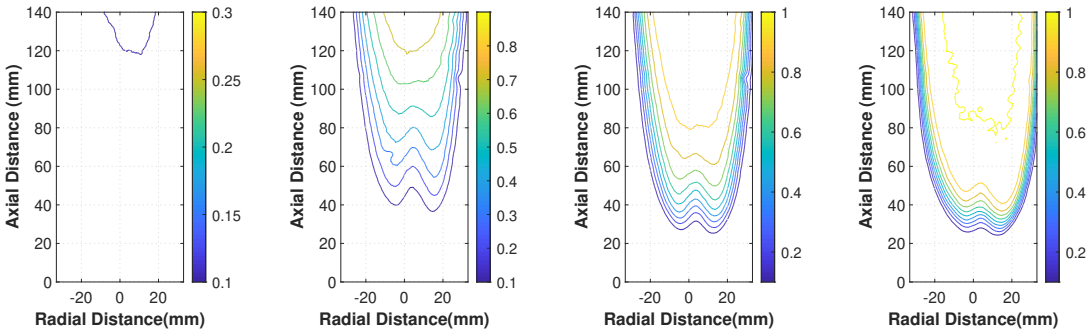

(e) 1065K, 43.5m/s (f) 1146K, 43.5m/s (g) 1210K, 40.0m/s (h) 1266K, 39.8m/s

Figure 4.1: Intermittency of OH* chemiluminescence with tapered fuel injector (a-d) and blunt injector (e-h)

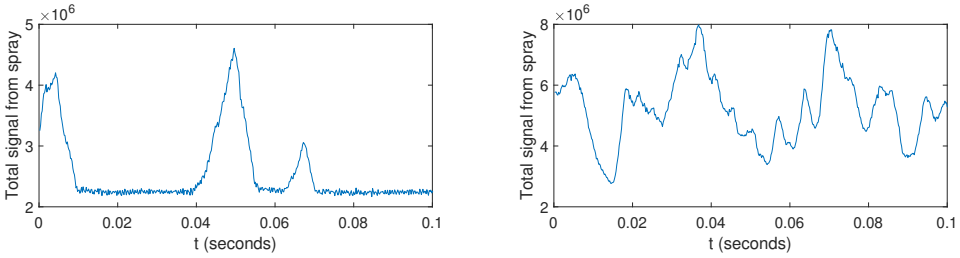

(a) T = 1061K, u = 41.7m/s (b) T = 1145K, u = 42.2m/s

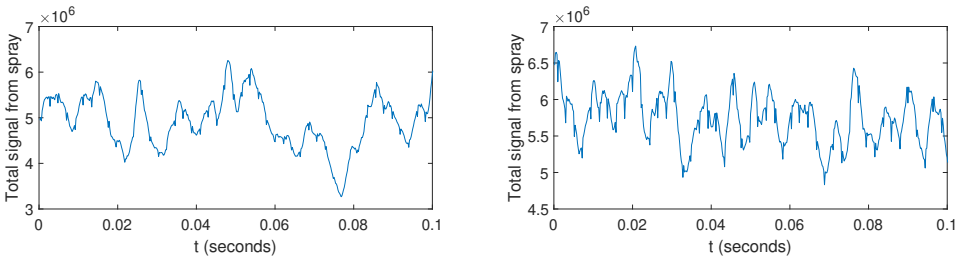

(c) T = 1212K, u = 40.0m/s (d) T = 1270K, u = 41.3m/s

Figure 4.2: Time histories of OH* total intensity with tapered fuel injector

The combustion that appear at the lowest temperatures correspond to light less than 5-10% of the total frames. At the highest temperatures tested, there are portions of the test section that have light >90% of the total frames. In the intermediate temperature range, the space between the contours decreases as temperature increases. This could correspond to combustion initiating within a smaller region, closer to the fuel injector and with less scatter or the regions of combustion growing faster and producing more heat release due to the higher temperatures. Operation at low temperatures will exhaust a large percentage of unburned fuel while high temperature operation will burn most of the fuel. This intermittency calculation, constrained to the upstream region, is another way to represent the autoignition kernel formation and scatter. These results show that autoignition and the subsequent combustion have nonuniform temporal behavior, which will be further investigated by looking at the dynamics of the combustion.

The total light intensity of each frame is shown as a time history in Figure 4.2. The time histories are shown for only the tapered fuel injector as the qualitative results are similar for both injector shapes. Note that time histories are shown for only 10% or 0.1s of the total data collected (1s or 5000 frames) to allow for better visibility.

As the temperature increases over the range tested, there are two characteristic changes: the average intensity level increases, and the spacing between peaks in chemiluminescence intensity decreases. At low temperatures, the kernels appear as bursts in the time history, while at high temperatures there is a persistent average light level around which fluctuations occur. This agrees with intermittency results;, as temperature increases the regions of high intensity chemiluminescence are more persistent in time, ultimately leading to regions where chemiluminescence is always visible and there is more overall heat release at higher temperatures. At low temperatures, the bursts do not occur frequently enough or maintain position in any given region long enough to contribute to significant heat release.

The time histories of total light intensity suggest there are fluctuations in light intensity that could indicate oscillatory autoigniton. In order to investigate further, a Fast Fourier transform was performed on each time history. The results are shown in Figures 4.3a and 4.3. The total signal was $1s$ at $5000Hz$ while the FFT was performed indvidually on 5 segments of each time signal and averaged to reduce noise. Any peaks in these results will be due to coherent fluctuations in the total chemiluminescence over time. At low temperatures, there are no discernible peaks in the spectral analysis. As temperature increases for both fuel injectors, a response appears near 120Hz, most likely corresponding to the 1/4-wave longitudinal mode of the test facility. The following frequencies are near the harmonic frequencies of the 120Hz peak. The period of this oscillation is approximately $8ms$. The autoignition delay times measured in the test facility range from $0.6ms$ to $4ms$. A large acoustic velocity fluctuation could potentially affect the results of the experiment since autoignition does not happen at long times compared to the period of the oscillation. The droplets will also be analyzed for a response to the acoustic oscillations.

4.1.2 Spray Dynamics

The fuel spray dynamics were characterized along the axial distance of the fuel spray using the Mie scattering from droplets during the PIV analysis. Since it was previously shown

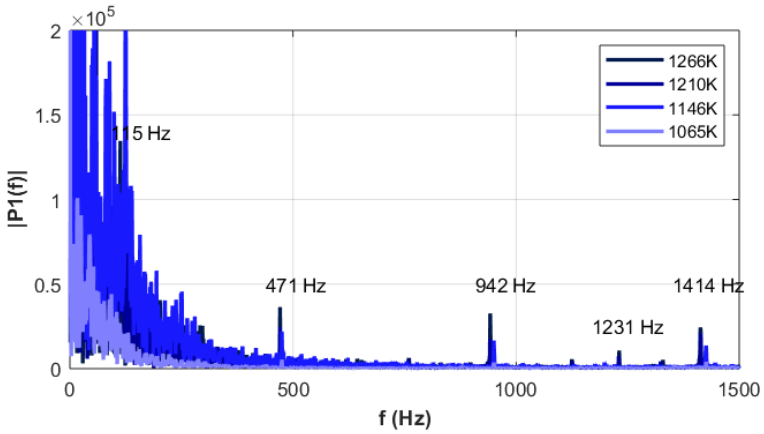

(a) Tapered fuel injector

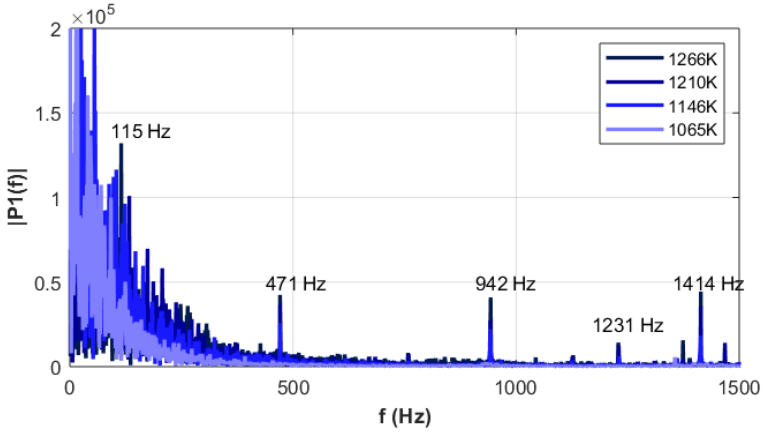

(b) Blunt fuel injector

Figure 4.3: FFT of OH* chemiluminescence time histories, $F_s = 5000Hz$, $\Delta f = 5Hz$

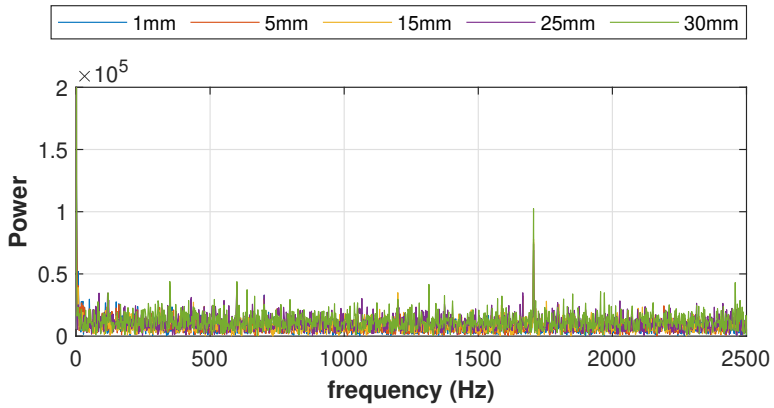

(a) Tapered fuel injector, T = 1204K, u = 42.4m/s

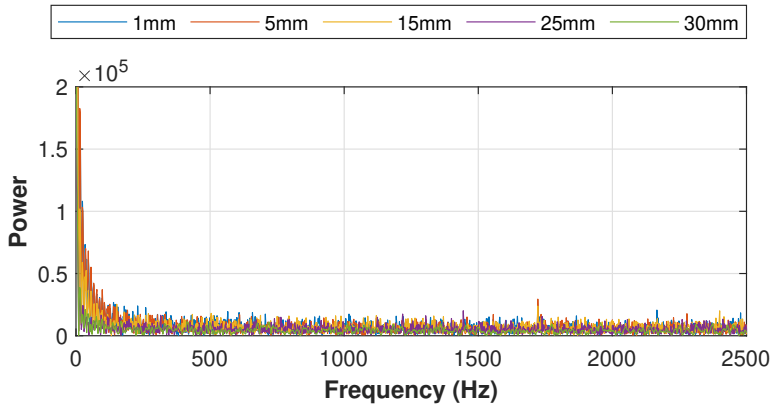

(b) Blunt fuel injector, T = 1177K, u = 44.3m/s

Figure 4.4: FFT of integrated droplet Mie scattering light intensity at 1, 5, 15, 25, and 30mm axial distance downstream of the fuel injector, F_s = 5000Hz, Δf = 8Hz

that the largest amplitude dynamics should occur at the hottest temperatures in the investigated range, only the results at those temperatures are shown. The total light at each axial distance was summed for each frame. An FFT was performed on the time history of the total light at a few axial planes, 1, 5, 15, 25, and 30mm from the fuel injection plane. The results of the FFT analysis is shown in Figure 4.4.

The plot suggests that the fuel spray does not couple with the flow dynamics in the test facility. Peaks near 120Hz and its harmonics are barely distinguishable from the noise in the spray dynamics response. If there is a slight coupling of spray oscillation and flow acoustics it could be due to reasons such as the droplets oscillating with the flow velocity.

If the oscillations are in phase, it would suggest this method. Alternatively, the acoustic pressure fluctuations could affect the spray formation and flow rate if the signals were out of phase. This does not seem likely because of the high pressure drop across the fuel injector; the pressure fluctuations would have to be very high to affect the injector performance. The dominate quarter wave mode and the harmonics as were seen in the total chemiluminescence analysis do not show high amplitude response in the fuel spray. Some of the planes show a dynamic response near $1700Hz$, which did have a corresponding response in the chemiluminescence dynamics. This oscillation would have a period of $0.6ms$ which is comparable to the lifetime of a small droplet and could affect the behavior if it became high amplitude.

4.1.3 Autoignition Behavior

As the inflow temperature was varied, three types of behavior were observed in the high-speed OH* chemiluminescence results. An example of each type is illustrated in Figures 4.5- 4.7. Each figure displays a representative sequence of images at one nominal operating condition. The time between each image shown in the sequence is $1ms$, and since the framing rate was 5 kHz, these sequences show only every fifth frame acquired during the time represented. These images are cropped such that the injector is located at the center of the bottom of the image, marked by a line in the figure. The test section walls are the left and right edges of the image, and the flow is moving upward.

At low temperatures, but high enough that autoignition is observed (e.g., $1061K$, Figure 4.5), autoignition occurs infrequently and randomly in time. Small kernels are formed that grow in size and brightness as they convect downstream. These kernels have usually completely left the test section before another autoignition kernel is formed. There is very low total heat release at this condition, and unburned fuel escapes the test section between autoignition kernels. In the example shown in Figure 4.5, the autoignition kernel is convecting at $26m/s$, while the average flow velocity in the test section is approximately

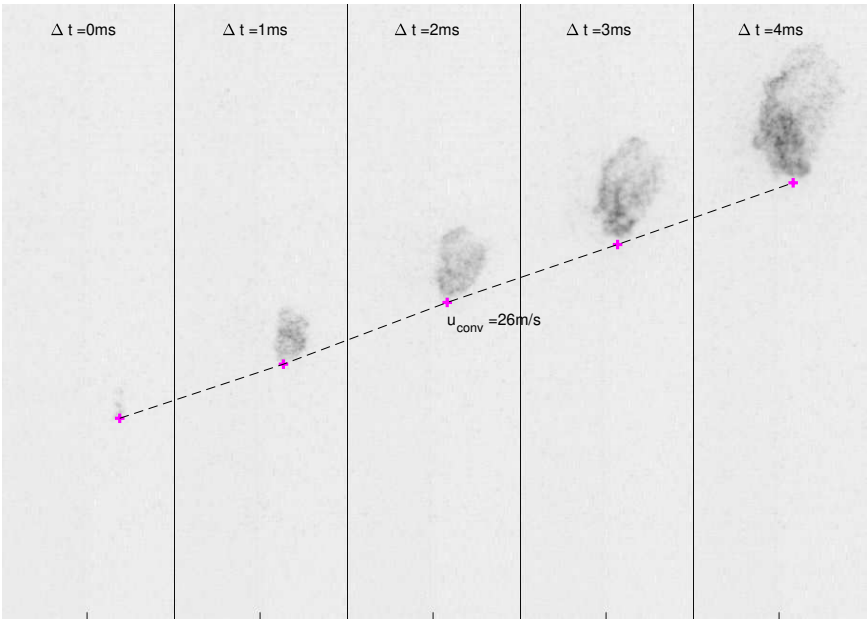

Figure 4.5: Random autoignition kernels from OH* chemiluminescence, $T_{corr} = 1061K$, u=41.7m/s; the width of each image corresponds to the internal diameter of the test section: 75mm

40m/s. This kernel is far enough downstream to not be affected by wakes produced by the fuel injector body. The difference in convection velocities suggests a flame propagation speed of 14m/s upstream.

As the temperature increases (e.g., 1145 K, Figure 4.6), the occurrence rate of autoignition kernels increases; they begin to form before previous kernels have exited the test section. In the specific case shown here, three distinct combustion regions are present in the early part of the sequence, though by the end of the sequence, they appear to have merged into a single flame moving downstream. At that time, however, a new kernel begins to form well upstream. The speed of three kernels can be calculated; each appears to move downstream at a different velocity, between 21 and 27m/s, with the lower velocities corresponding to the more upstream kernels. Thus these kernels move downstream more slowly than the low temperature example. The nominal flow velocity in the test section is nearly the same as before, since the air flow rate entering upstream remains relatively the

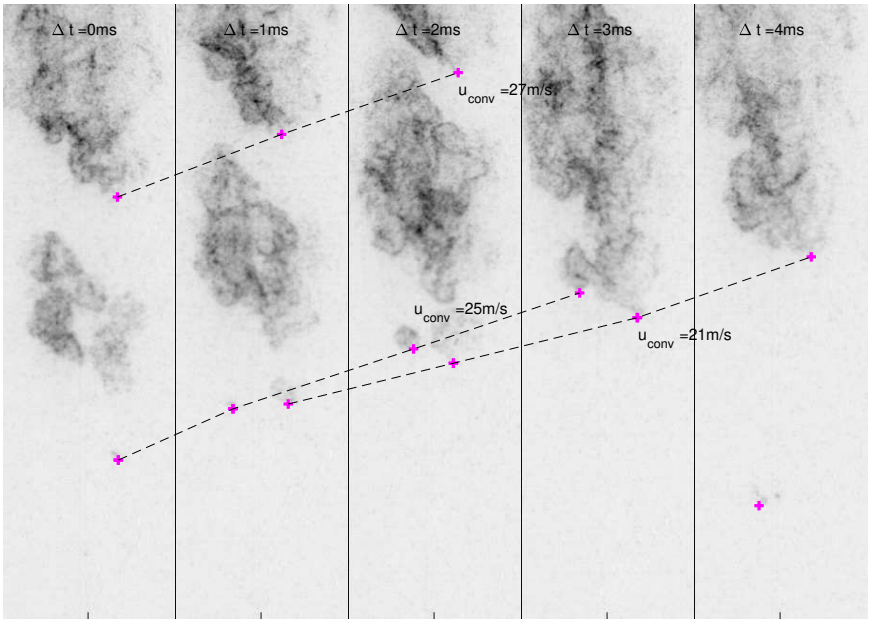

Figure 4.6: Periodic autoignition kernels from OH* chemiluminescence, $T_{corr} = 1145K$, u=42.2m/s; the width of each image corresponds to the internal diameter of the test section: 75mm

same. Finally, the kernels begin to appear preferentially (but not solely) at the longitudinal instability frequency of the test facility, approximately 120Hz as was shown in the FFT results in Figure 4.3a, which corresponds most closely to the quarter-wave mode of this open-closed configuration.

As temperature is increased further (e.g., 1270 K, Figure 4.7), there is a transition to a continuous flame mode that appears as a quasi-stationary, lifted flame in the fuel spray. The front edge of the lifted flame occasionally jumps forward, as shown in the last frame of Figure 4.7. A small downstream convection speed of 3m/s was observed before the autoignition kernel jumped upstream again. This behavior may suggest that the flame speed in this high temperature condition is sufficient to keep the flame at a nearly constant location. Only the observed upstream jump in the region of heat release is used to identify a new autoignition kernel formation, in order to distinguish autoignition from a potentially flame-stabilized condition. This jump corresponds to a 9mm change in position over 1

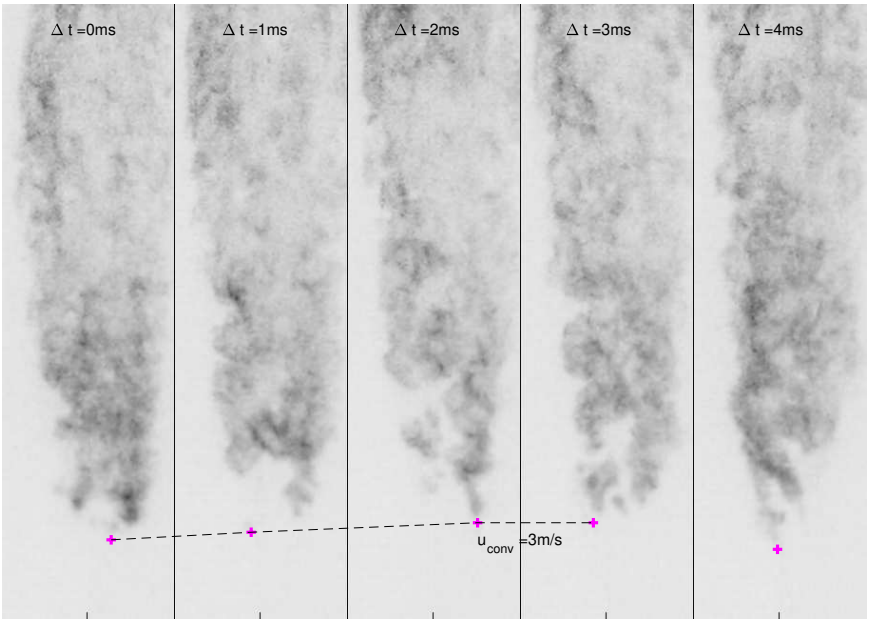

Figure 4.7: Continuous autoignition kernels from OH* chemiluminescence, $T_{corr} = 1270K$, u=41.3m/s; the width of each image corresponds to the internal diameter of the test section: 75mm

frame (5 frames are between each image shown, but this calculation is from the frame just before the last frame shown), which implies a minimum upstream velocity of 18m/s over the co-flow velocity of approximately 40m/s. It is unlikely that a jump would correspond to the flame traveling upstream at such high speeds so it is reasonable to use this condition as a determination between flame propagation and autoignition.

It should be noted that the average velocities in the wake of the injector are lower than the co-flow velocity as was previously shown in the flow characterization results of Chapter 2. These flame speeds are estimated based on the difference between the flow velocity and the downstream motion of the kernel for these images only, but could be lower if the region corresponds more with a wake velocity. This should only affect kernels that are formed very near the fuel injector with the wake extending to approximately 50mm downstream from the exit of the fuel injector.

Figure 4.8 shows the calculated temperature dependence of the 1-d laminar flame speed

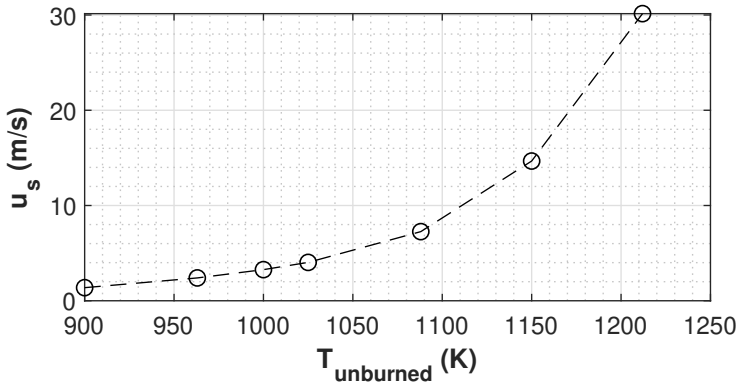

Figure 4.8: Calculated temperature variation of flame speed using HyChem model in Chemkin

of Jet-A as determined through the Chemkin analysis described in Chapter 2. The random and periodic kernels have estimated flame speeds of around 14-19 m/s corresponding to the difference in convection speed and average co-flow velocity. For the continuous autoignition case, the flame speed exceeds $35m/s$ which would occur at temperatures above 1225 K. The flame speeds estimated from the OH* data give values that are slightly higher than was predicted using the 1-d laminar flame. It is possible that autoignition is occurring in regions of the flow that have less mixed vitiated air product and dilution air, resulting in a higher temperature region or that the flame speeds are enhanced due to local turbulence.

4.2 Ignition Delay Time Analysis

Autoignition has historically been characterized primarily based on an overall ignition delay time measurement. This study allows for the calculation of instantaneous autoignition delay time statistics in addition to an average ignition delay time. In this section, the measured autoignition delay times are calculated, discussed, and compared to calculated average times and theoretical results based on modeling.

4.2.1 High-Speed Chemiluminescence Autoignition Locations

The methodology for determining the autoignition delay times was described in Chapter 2. It begins with the determination of the locations where ignition kernels form. These locations were first found from the $5000 fps$ OH* chemiluminescence imaging over a range of temperatures and for two injector shapes. The primary consideration is that only jumps upstream in chemiluminescence can be attributed to autoignition. From such data, the initiation location of autoigniton kernels was calculated for each $1s$ OH* chemiluminescence data set. The flow conditions for the test series are tabulated in Table 4.1.

The variation in the autoignition location can be seen in Figure 4.9 and Figure 4.10, which show the initiation locations of all the identified kernels for the tapered and blunt injectors. The dashed horizontal lines indicate Y_{min} for each condition, while the * symbol indicates the average position (r_{avg}, Y_{avg}). Separate OH* and CH* images were obtained simultaneously during the experiments, but as the resulting identical kernel locations were essentially identical, only the Y values from the OH* data are reported here. From such data, the average axial location (Y_{avg}), most upstream axial location (Y_{min}), and the corresponding standard deviation (σ_Y) were found.

For both injectors, the relatively rare occurrence of kernels at the lowest temperatures is clearly evident by the few data points compared to the higher temperature results. The lowest temperature case for the blunt injector produces more kernels than for the tapered injector; however, the temperature of the blunt case ($1065K$) is slightly higher than for the tapered case ($1061K$). So the increased occurrence may result from the higher temperature rather than the change in injector configuration. Additionally, Y_{min} moves upstream a significant amount ($15mm$) when the inflow temperature is increased by $84K$ (1061 to $1145K$) for the tapered injector. With roughly the same temperature increase for the blunt injector, but at a slightly higher range of temperature (an $81K$ change from 1065 to $1146K$), Y_{min} moves upstream by only $9mm$. At even higher temperatures, there is much less change in Y_{min}. Finally, the ignition locations are not uniformly distributed in the axial

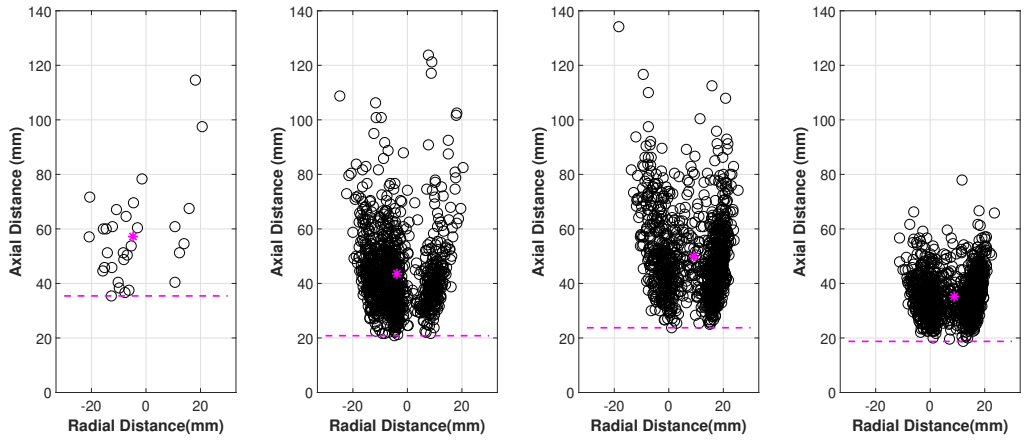

(a) $1061K, 41.7m/s$ (b) $1145K, 42.2K$ (c) $1212K, 40.0m/s$ (d) $1270K, 41.3m/s$

Figure 4.9: Autoignition kernel locations of OH* chemiluminescence with tapered fuel injector; dashed line illustrates Y_{min} location and $*$ indicates average autoignition location

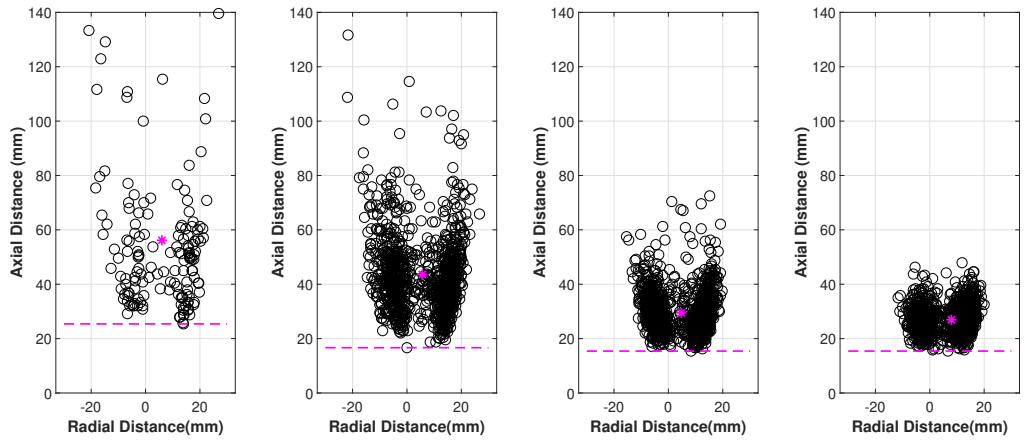

(a) 1012K (b) 1080K (c) 1130K (d) 1175K

Figure 4.10: Autoignition kernel locations of OH* chemiluminescence with blunt fuel injector; dashed line illustrates Y_{min} location and $*$ indicates average autoignition location

Table 4.1: Autoignition locations and scatter from OH* chemiluminescence imaging at $5000 fps$

Date	Shape	Vid #	T_{corr} (K)	O_2%	u (m/s)	Y_{min} (mm)	Y_{avg} (mm)	σ_Y (mm)
20150911	B	21	1266	8.8	39.8	15.4	27.0	4.9
		22	1210	9.5	40.0	15.4	29.5	7.64
		23	1146	9.3	43.5	16.7	43.6	16.4
		24	1065	9.6	43.5	25.4	56.2	30.7
	T	25	1270	9.1	41.3	25.4	56.2	30.7
		26	1212	9.3	40.0	25.4	56.2	30.7
20150914	T	21	1061	9.6	41.7	35.4	57.2	17.5
		22	1145	9.4	42.2	20.8	43.5	13.9
		23	1221	9.3	42.1	15.4	38.9	10.0
		24	1219	9.3	32.9	11.7	37.3	15.4
		25	1218	9.2	53.4	16.7	37.9	11.1

direction; rather the density of points is higher closer to the injector.

These behaviors suggest two things. First, there is some process limiting the most upstream location of the ignition kernels that is not a strong function of the inflow temperature. Second, the scatter in the initial location of the kernels is indicative of a stochastic process that likely results from variations in the inflow conditions with time, e.g., the distribution of the local flow temperature or fuel fraction. If there are such variations, which is quite likely, the ignition kernels would be associated only with the most favorable wings of those distributions.

It is also noteworthy that while the average ignition location is near the radial center of the test section, few autoignition kernels are initiated on the centerline. Rather at all temperatures, the kernel locations are clustered in the wake of the most dense region of fuel spray, based on the PDPA results. This region could correspond to where there is the most fuel vapor available for reaction.

Generally, as the inflow temperature increases, both the minimum and average ignition positions move upstream (increasing Y), with a greater change in the average position. Also the standard deviation of the initial kernel location decreases with increasing temperature.

Table 4.2: UV PLIF Flow Conditions

Inj	Temperature (K)	Velocity (m/s)	$O_2(\%)$	ϕ_{Jet-A}
T	1106	33± 2	11.3±0.1	0.7
T	1137	33± 2	11.3±0.1	0.7
T	1211	33± 2	11.3±0.1	0.7
T	1272	33± 2	11.3±0.1	0.7
T	1137	43± 3	10.8±0.1	0.7
T	1211	43± 3	10.8±0.1	0.7
T	1272	43± 3	10.8±0.1	0.7
B	1138	31.8	11.4±0.1	0.7
B	1180	34.2	11.3±0.1	0.7
B	1204	35.4	11.2±0.1	0.7

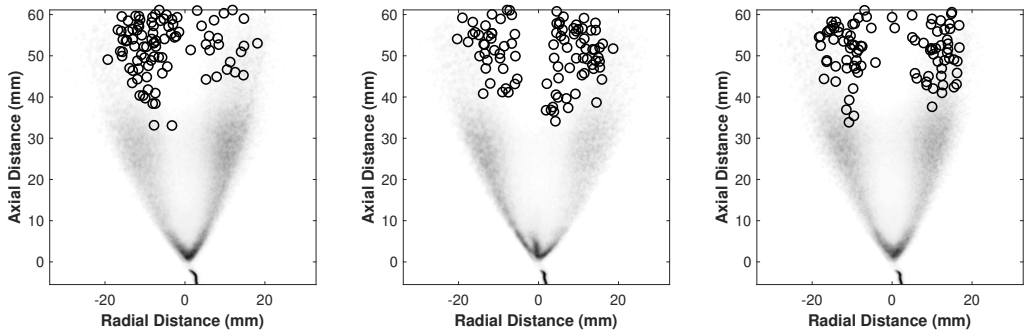

(a) 1137K (b) 1211K (c) 1272K

Figure 4.11: Autoignition kernel scatter from UV PLIF imaging at 43m/s for tapered fuel injector

4.2.2 OH PLIF Autoignition Kernel Locations

In order to investigate further the fuel spray and autoignition kernel interaction, UV PLIF was focused on the most upstream region where autoignition kernels were observed to be formed. From the instantaneous images, droplets are characterized by a bright signal and, or, a circular shape, while the autoignition kernels have a signal that occurs within fairly specific range of values and no defined shape. These differences were used to inform the edge tracking software and help eliminate objects. Once an autoigntion kernel was identified, the centroid of the kernel, total area and effective radius, and average intensity were calculated.

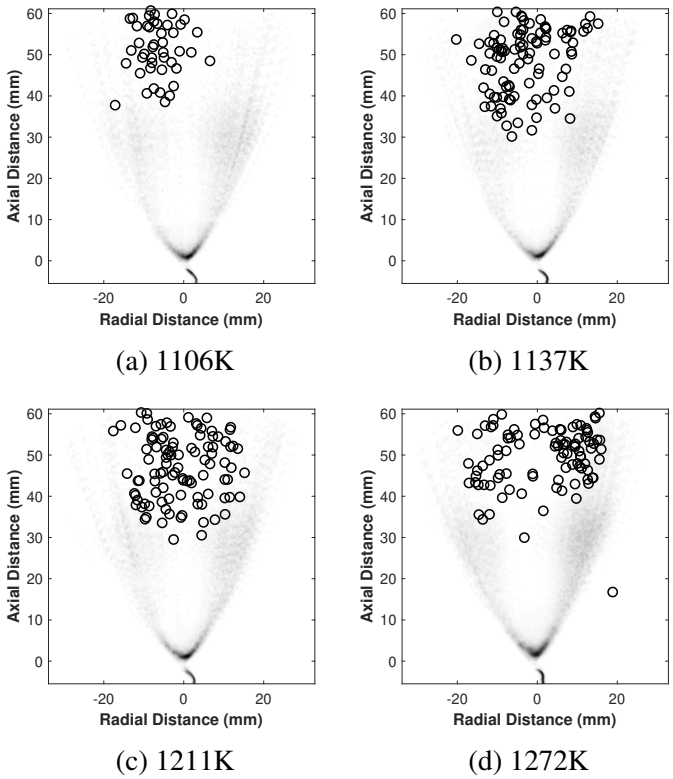

(a) 1106K (b) 1137K

(c) 1211K (d) 1272K

Figure 4.12: Autoignition kernel scatter from UV PLIF imaging at $33 m/s$

Figures 4.11 and 4.12 show the location of autoignition kernel centroids compared to the average UV fluorescence at two co-flow velocities. The average fuel spray is visible, and it is observed from these images that the fuel spray angle changes due to the change in velocity. A lower co-flow velocity gives a wider spray angle and the region of denser fuel droplets expands. Autoignition kernels were not observed in the measurement section at $1000K$ for either flow velocity or at $1040K$ for a $50 m/s$ co-flow. The effect of temperature at higher co-flow temperatures, where autoigniton kernels are formed within the viewing window is minimal. There is a slight shift upstream due to decrease in co-flow velocity, but a significant enough change as would be expected due to the change in convection time. Similar to the OH* chemiluminescence results, autoigntion kernels appear more frequently as temperature increases. A total of 100 kernels were found at each temperature, if possible, but the number of frames to find these kernels decreases with temperature. For example, the lowest temperature conditions took on the order of 1000 frames to find 53 kernels while

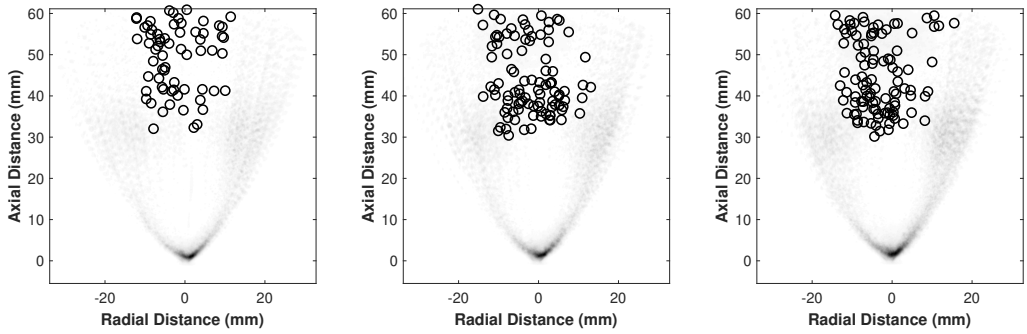

(a) 1138K (b) 1180K (c) 1204K

Figure 4.13: Autoignition Kernel Scatter from UV PLIF Imaging at 30m/s for blunt fuel injector

the highest temperature condition provided 100 kernels in 240 frames. Since the process to identify kernels was not fully automated it was quite time-consuming so 100 kernels was chosen as the goal for the number of data points to achieve.

In the dilute spray studied by O'Loughlin et al, OH PLIF autoignition kernels were reported on the outer edge of the spray [38]. In this denser fuel spray, autoignition kernels found using OH PLIF are focused inside the cone of the fuel spray. As with OH* chemiluminescence, the kernels are mainly downstream of the highest density droplet regions. More kernels were formed in the center of the spray at a lower velocity and wider spray angle. Autoignition kernel formation and growth in relation to the droplet locations will be discussed further in the following chapter.

Figure 4.13 shows the scatter of autoignition kernel locations for the blunt fuel injector at the lower co-flow velocity. The average image in the background of the plot shows an even wider spray angle than observed in Figure 4.12, most likely due to the lower velocities and presence of a recirculation zone in the wake of the blunt fuel injector cap. The spread of radial locations of autoignition kernel initiation fall within a narrower region than similar flow conditions with the tapered fuel injector. The axial location of the autoigniton kernels start at comparable locations, near 30mm for these temperatures.

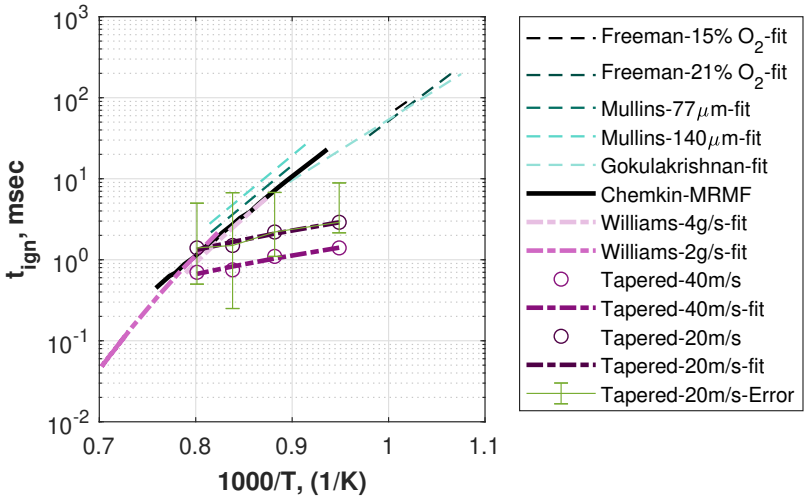

Figure 4.14: Calculated average ignition delay times compared to Chemkin simulation

4.2.3 Ignition Delay Times

Figure 4.14 shows the average ignition delay times calculated from the mean location of the kernel measured for the tapered fuel injector at 40 m/s compared to values determined from the analysis of the most reactive mixture fraction (MRMF). Ignition delay times are calculated only from OH* chemiluminescence kernel locations. The Chemkin model used to find the MRMF ignition delay has been previously discussed; but to summarize, methane and air are burned in a laminar flame at stoichiometric conditions, then cooling air is added and heat loss is introduced in the plug flow reactor used to represent the mixing section. The parameters are chosen to match the overall vitiator equivalence ratio and match measured temperatures at the entrance to the test section. This temperature is the center flow value calculated from the wall thermocouple, using the center-to-wall correlation and radiation correction. Lastly, prevaporized Jet-A is mixed with the preheated air and the HyChem A2 fuel mechanism is used to determine the reaction rates and resulting ignition delays. Ignition delay time was calculated as the point of inflection in the temperature profile of the plug flow reactor.

Traditionally, the average co-flow velocity is used to convert measured autoignition locations to delay times in this type of experiment. If the results of LDV and PIV mea-

surements are considered, the flow velocities in the region of the fuel injector are slower than the bulk average velocity. The injector wake continues until approximately $50mm$ downstream of the fuel injector (with additional reduction of the flow when spray is in operation, due to the drag from the slow moving droplets). For the cases under consideration here, autoignition occurs within or just beyond this low velocity region, so the fluid packets that become ignition kernels have experienced these slower velocities through most of their pre-ignition history. Therefore, results are shown in Figure 4.14 using the bulk average coflow velocity of $40m/s$ and a more representative velocity of $20m/s$ to convert distances to times.

For both choices, the measured autoignition delay times are shorter than the MRMF predictions for premixed, prevaporized conditions and the experimental values reported in the literature from experiments [23, 25, 26, 27]. The slower velocity results are closer to the MRMF simulation and the previous results, with the difference decreasing with temperature. In fact, at the highest temperature, the average ignition delay time is comparable to, just slightly longer than, the MRMF prediction.

It is worth to note that previous average ignition delay times obtained in this facility [27] (denoted Williams-$4g/s$ in the figure) are longer than the current delay measurements and closely match the MRMF predictions and other values reported in the literature. The previous measurements, however, relied on long-exposure images of the chemiluminescence. The faster ignition delay times were observed only when using time-resolved, intensified imaging techniques. Using long exposure (and thus time-averaged) measurements produces an image that is skewed towards the highest intensity light seen by the camera. In the previous work, the entire test facility was imaged, resulting in a very bright flame downstream of where autoignition begins, since the flame has grown in size and intensity. This method of averaging is less likely to catch any early, dim autoignition events. In contrast, the high-speed imaging technique with intensifier has a very short open shutter time so the images are able to capture the earlier, dim autoignition kernels.

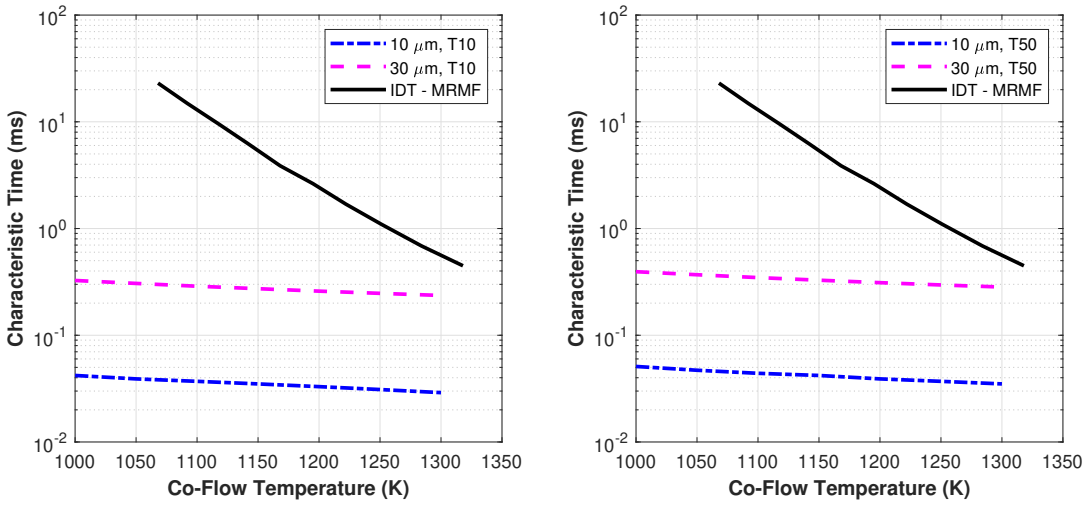

(a) 10% Recovery Temperature of Jet-A (b) 10% Recovery Temperature of Jet-A

Figure 4.15: Comparison of calculated ignition delay times at most reactive mixture fraction using HyChem model in Chemkin to droplet heat-up times for 10 and 30μm droplets at 10 or 30% Jet-A recovery temperatures

Figure 4.14 also includes representative deviation bars for the range of ignition delay times measured at the corresponding flow conditions. The upper limit is determined using twice the RMS of the locations and then converted to convective time using the 20m/s flow velocity. The approach used for the upper deviation limit would result in negative ignition delay times is applied to the lower limit, therefore the lower limit is determined from the difference between the average location and most upstream location. Ignition delay times along the upper limit of the measured range are longer or nearly agree with the MRMF predictions and previous work.

While the average ignition delay times are shorter than expected, the results tend toward agreement with the MRMF predictions at higher temperatures. Figure 4.15 shows the calculated characteristic times calculated using the model described in Chapter 2. The ignition delay times shown correspond to the values calculated for the most reactive mixture fraction and the droplet heat up times are calculated for two different droplet sizes, 10μm and 30μm for both 10% and 30% Jet-A recovery temperatures. These droplet sizes represent two regions in the fuel spray: the center of the fuel spray has small droplets with

average size of approximately $10\mu m$ while the region of most dense spray, as represented by the highest velocity data rate, has average sizes of approximately $30\mu m$. It is expected that minimal evaporation will happen during the droplet heat up time. At lower temperatures, in the range studied throughout this thesis, the characteristic ignition delay time, representing the chemical delay portion of the ignition delay time is much longer than the droplet heat up time. This suggests that droplet vaporization would not limit any chemistry at these conditions. As the temperature increases to the highest average values measured in this study, the chemical time approaches the droplet heat-up time estimated for $30\mu m$ droplets and droplet vaporization could become the limiting timescale. Any local variation in temperature higher than the average temperature or region of the spray with larger droplets would exacerbate this condition even further.

A single droplet is a simplification of the polydisperse fuel spray used in the experiment. At locations from the center of the fuel spray, the droplet size distribution becomes wider and has a tail of large droplets. These larger droplets will not give much vapor to the system as they will have a much longer droplet heat-up time.

The flow characterization discussed in Chapter 3 suggests that while the average temperatures and velocity in the test facility seem uniform there could be temporal nonuniformities represented by regions of low seeding particle density in the PIV data. If these regions of low particle density represent flow that has not been significantly mixed with dilution air, temperatures could locally be much higher than the measured co-flow temperature. It would take a small increase in temperature (on the order of 10% of the flow temperature) to more closely match the values reported in literature and the amount decreases with increasing temperature. Using the Chemkin model, the vitiator exit temperature with $300K$ inlet air and room temperature natural gas would correspond to a max of $2200K$ if the vitiator operates at stoichiometric equivalence ratio as was shown in the profile in Figure 2.16. This implies that the flow would be cooled by a maximum of 900 to 1150 degrees through both dilution air and heat loss to the air cooled walls to achieve flow tem-

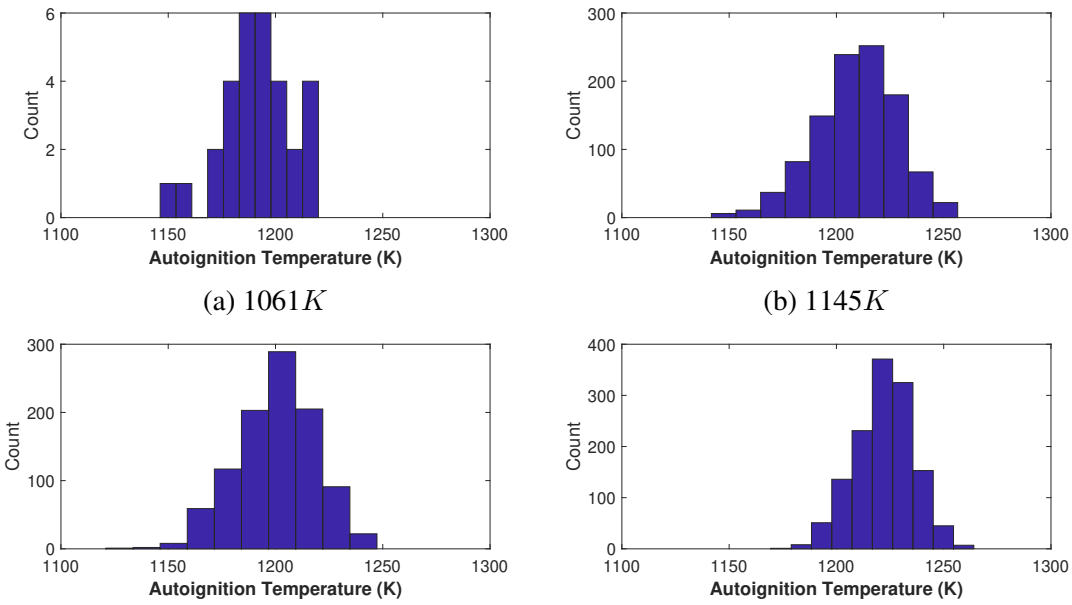

(a) $1061K$ (b) $1145K$

(c) $1212K$ (d) $1270K$

Figure 4.16: Histograms of temperature based on ignition delay times with tapered fuel injector

peratures of 1050 to 1300K (corrected for radiation at correlated center temperatures). A 10% temperature fluctuation is within what could be achieved if portions of the flow from the vitator exit are not cooled due to incomplete mixing.

Using the relationship between flow temperature and ignition delay time, this temperature effect is investigated further by estimating the temperature experienced by a kernel based on its ignition delay time. The $20m/s$ estimate for velocity in the wake and fuel spray regions and the ignition delay time correlation for most reactive mixture was used to convert the ignition locations from OH* chemiluminescence data to temperatures. The resulting values are shown in Figure 4.16 and Figure 4.17 for the tapered and blunt fuel injectors.

These results show that except for the lowest temperature condition, there are ignition kernels that formed at distances (and residence times) that correspond to the average co-flow temperature. For all conditions, there are also autoignition kernels corresponding to temperatures above $1200K$. There are no kernels observed with temperatures higher than

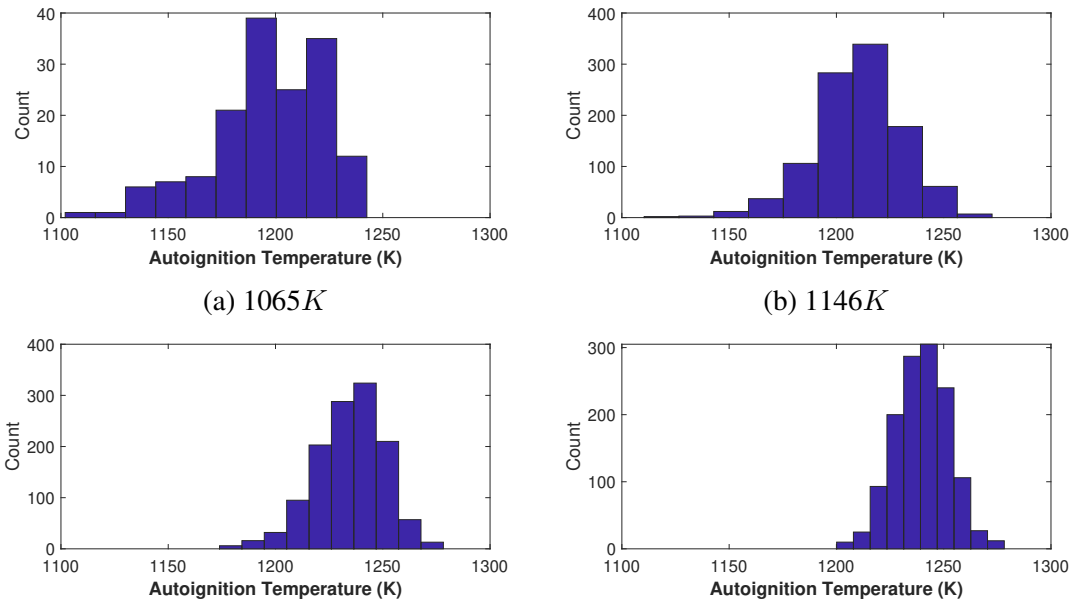

(a) $1065K$ (b) $1146K$

(c) $1210K$ (d) $1266K$

Figure 4.17: Histograms of temperature based on calculated ignition delay times with tapered fuel injector and the most reactive mixture

$1275K$ even though the highest average flow temperatures measured are 1266-$1270K$. Referring again to the calculated characteristic times in Figure 4.15, this seems to correspond to a region where droplet heat up times begin to become the limiting time scale as opposed to chemical time. Autoignition times that correspond to lower temperatures could be due to either regions of cooler co-flow due to lack of mixing, or regions that have been cooled more considerably due to large droplet evaporation. Due to the range of temperatures experienced by kernels in the flow, the average ignition delay times have less response to average temperature than would be predicted by using solely the average co-flow temperature.

4.3 Comparison of Diagnostic Methods

First it is worthwhile to summarize the difference in the two diagnostic methods. OH* chemiluminescence is a line-of-sight, integrated technique, while the UV PLIF is planar. Chemiluminescence can be attributed to light produced from a chemical reaction or high temperature. The UV PLIF is a representation of the concentration of OH species, whether

hot or cooled and will additionally show liquid Jet-A and potentially very cool Jet-A vapor.

Ignition locations are slightly further downstream than the locations found with chemiluminescence, up to a $10mm$ difference. The methodology for finding kernels for two diagmostic methods was different. The centroid of the PLIF kernel was found, while the most upstream location of the OH* chemiluminescence was used. PLIF kernels were formed primarily in the size range of 1-10mm^2 with a few larger kernels in the size range of $35mm$, according to the size histograms shown in Figures 4.18 to 4.22. If these sizes are converted to an equivalent radius, assuming a circular kernel (which was often not the observed shape), the radius would range 1 to $2mm$ with excursions to 4-5mm for the largest kernels. These values would explain some of the differences seen in ignition delay time differences. The overall equivalence ratios are stoichiometric for the chemiluminescence autoginition and 0.7 for the PLIF. Slightly less fuel could potentially slow reaction rates and increase ignition delay times, but as this is a non-premixed system it is unlikely to have a local effect.

Another observation is that despite the same measured wall temperature, the OH* chemiluminescence kernels measured a lower oxygen content at the wall than the OH PLIF flow conditions. A single wall to center temperature correlation was used for both experimental campaigns. Despite the campaigns being close in time, it is possible that the thermocouple aged or the split between vitiator and dilution air could have changed and caused a higher wall temperature to be measured during the PLIF tests, requiring a lower vitiator fuel-air ratio and therefore higher oxygen content. At these temperatures, to move the ignition locations downstream by 5-8mm (accounting for the radius calculated previously) would require a small increase in temperature, on the order of $50K$ would be enough to account for this difference.

Due to the larger viewing window with the OH* chemiluminescence, kernels are observed forming at locations much further downstream than can be seen in the limited view of the PLIF, which will affect a comparison of the average axial locations calculated using

each method. The PLIF locations are skewed to faster, upstream kernels that are visible in the limited viewing window. The range of radial autoignition locations is comparable for both diagnostic methods, they occur roughly between $\pm$20mm in the radial direction. At some flow conditions, the PLIF data shows more autoignition kernels in the center of the fuel spray that was observed in the chemiluminescence. Additionally, the autoignition kernels from chemiluminescence analysis are much larger in size than the sizes calculated using the PLIF analysis. This may imply that the kernels observed in the chemiluminescence data is actually a grouping of smaller kernels that are indistinguishable due to the image resolution and line-of-sight nature of the chemiluminescence.

A comparison the ignition kernel location results shows both methods could be used to determine ignition delay times if the UV PLIF laser could be reliably expanded to a larger sheet size or the temperature range confined to a region where all of the kernel scatter could be located within the laser sheet. The difference in kernel size between the two methods may imply there may be more to the structure of an autoignition kernel than what can be captured using integrated imaging. The next chapter will investigate the structure of autoignition kernels and their relationship to the fuel spray and droplets using primarily the UV PLIF results.

4.4 Other Autoignition Kernel Properties

4.4.1 Kernel Size

The size of each kernel was calculated at the time of first appearance. This was done by adding the total number of pixels in the thresholded region that corresponded to an autoignition kernel, then using the appropriate scaling to convert units to cm^2. Histograms of the kernel size from OH* chemiluminescence are shown in Figures 4.18 and 4.19. Kernels can be formed at any time between the consecutive frames, so they could be formed at smaller sizes and have grown before they have been recorded by the image.

At lower temperatures, only small, individual kernels are formed. As the co-flow tem-

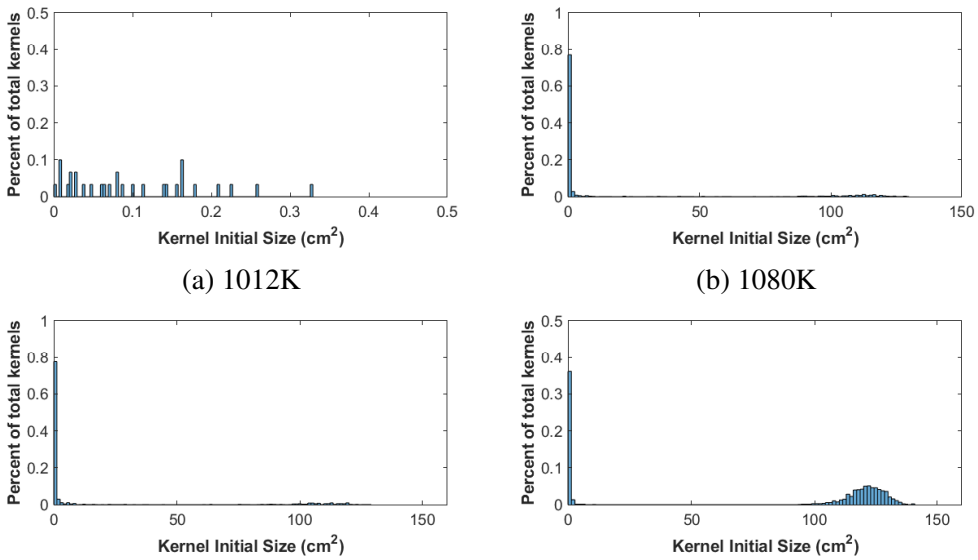

(a) 1012K (b) 1080K

(c) 1130K (d) 1175K

Figure 4.18: Initial autoignition kernel size with tapered fuel injector using OH* chemiluminescence

perature increases, kernels of larger size begin to form. Based on examination of images like those shown in Figure 4.7, these larger sizes correspond to kernels forming upstream that are connected to larger areas of luminosity downstream. As these kernels form farther upstream of the existing combustion region than can easily be justified by flame propagation, this is still considered to be autoignition.

At the highest temperature, which was described above as continuous autoignition, most of the autoignition is characterized by these jumps upstream. The total area of the test section observed using the high speed chemiluminescence system was $200cm^2$. The largest kernels observed are when continuous autoignition occurs and kernel appears near the fuel injector that is connected to the continuous combustion region. These kernels approach a maximum size of $160cm^2$, nearly 80% of the observed test section area contains chemiluminescence.

The size of kernels as observed using the UV PLIF method are shown in Figures 4.20 and 4.21 for the tapered fuel injector at $43m/s$ and $33m/s$ and in Figure 4.20 for the blunt fuel injector at $33m/s$. The kernels are much smaller size than those measured with the

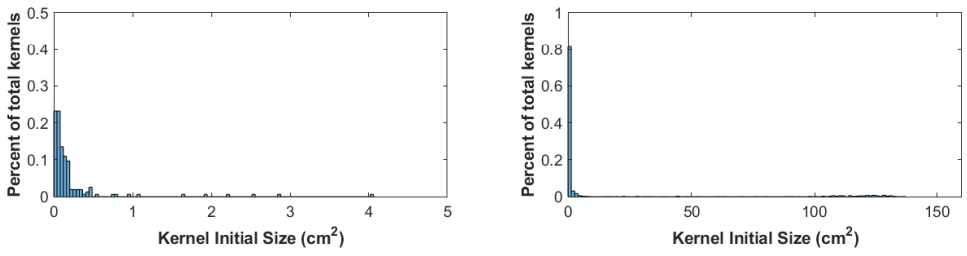

(a) 1012K

(b) 1080K

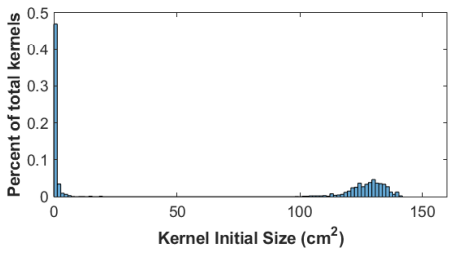

(c) 1130K

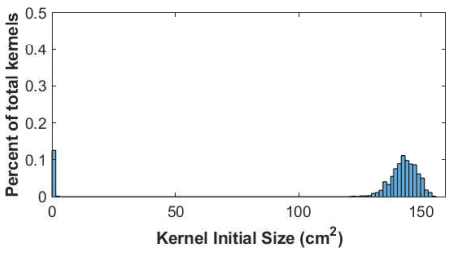

(d) 1175K

Figure 4.19: Initial autoignition kernel size with blunt fuel injector using OH* chemiluminescence

OH* chemiluminescence. It is possible that the PLIF measurement is more sensitive and shows the autoignition kernels sooner in their development compared to the OH* chemiluminescence experiment, therefore appearing smaller when they are first observable. The intensifier gate duration was half as long for the PLIF data compared to the chemiluminescence imaging so the chemiluminescence kernels could appear larger due to movement or growth during each snapshot. However as the kernels do not appear to grow as quickly between consecutive frames, this is unlikely to be the cause. Finally, it is also possible that the line-of-sight integrated chemiluminescence shows multiple, separate autoignition kernels as one larger conglomerate kernel. Multiple autoignition kernels were a common observance using the PLIF methodology and when spatially integrated could appear as a larger kernel.

4.4.2 Effect of Flow Velocity

Autoignition initiation locations are shown in Figure 4.23 for three different co-flow velocities at nearly the same co-flow temperature. As velocity changes, it is expected that

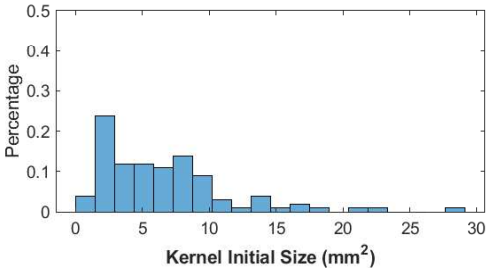

(a) 1065K

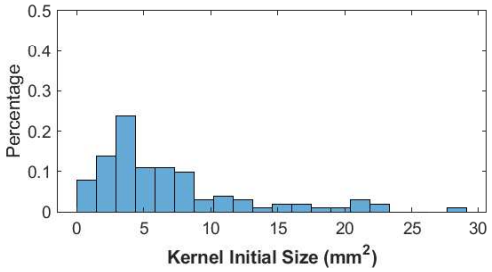

(b) 1124K

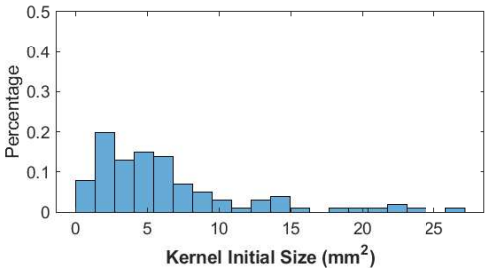

(c) 1171K

Figure 4.20: Histograms of kernel size at 43m/s for tapered fuel injector using UV PLIF

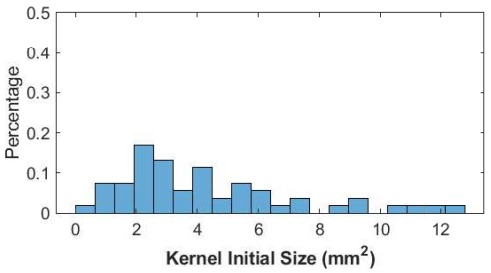

(a) 1040K

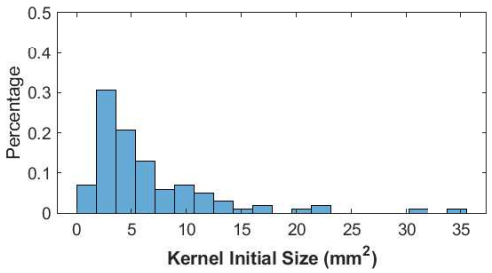

(b) 1065K

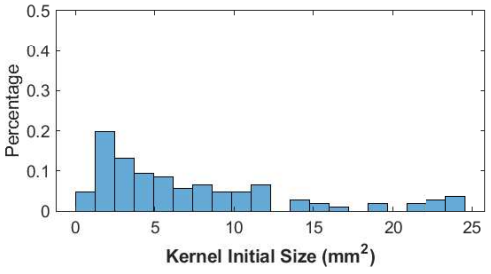

(c) 1124K

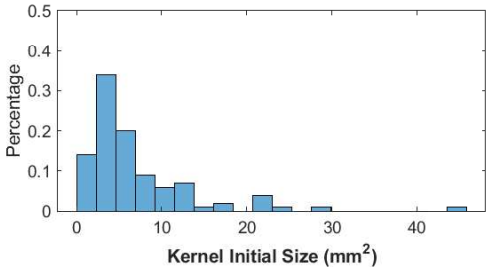

(d) 1171K

Figure 4.21: Histograms of kernel size at 33 m/s for tapered fuel injector using UV PLIF

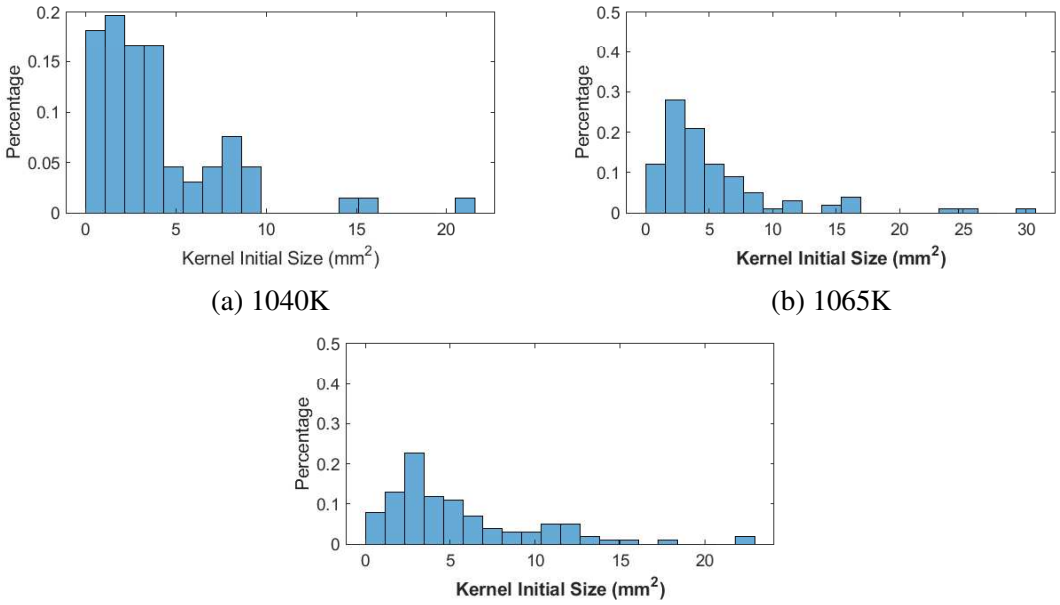

(a) 1040K

(b) 1065K

(c) 1124K

Figure 4.22: Histograms of kernel size at 33 m/s for tapered fuel injector using UV PLIF

ignition locations will change based on a convection time difference. Using there associated average co-flow velocities, based on vitiator mass flow rate, the most upstream location of autoignition gives similar values of $0.35ms$, $0.37ms$, and $0.32ms$ respectively, although that value for the median velocity is based on one isolated point. The majority of upstream locations for that condition occur slightly further downstream, pushing the ignition delay time closer to $0.4ms$. The temperature correction was performed at a single bulk velocity and would likely change with increasing flow rate. The center temperature correction is likely higher at the higher flow rate since their will be less heat loss to the walls and lower at the lower flow rate with more heat loss to the cooled walls.

The average ignition location does not show significant change over this range of velocity change. Interestingly, the lowest temperature shows the largest range of axial values. The ignition delay times corresponding to the most downstream kernels are $3ms$, $2ms$, and $1.5ms$. This could indicate that the lower velocity condition experienced more pockets of lower temperature than the higher velocity conditions, and that the uniformity of the flow and mixing are a function of velocity. As stated previously it is likely that the heat loss is

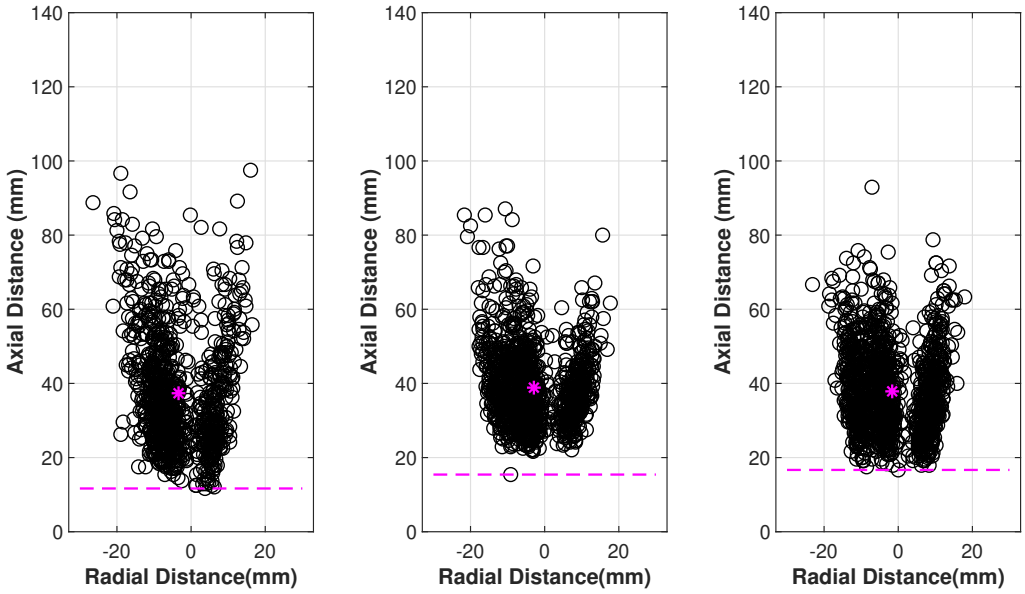

(a) $1221K$, $32.9m/s$, O_2 = 9.3%

(b) $1219K$, $42.1m/s$, O_2 = 9.3%

(c) $1218K$, $53.4m/s$, O_2 = 9.2%

Figure 4.23: Comparison of autoignition location scatter for tapered injector at 3 velocities; Dashed line illustrates Y_{min} location and $*$ indicates average autoignition location

lower at higher velocity so the decrease in "maximum" ignition delay time could be due to higher center temperatures as well.

4.5 Summary

Using high speed chemiluminescence, three distinct behaviors were observed: random autoignition, periodic autoignition, and continuous flames, and the transition from random to continuous occurs with an increase in co-flow temperature. The speed of upstream flame propagation of a kernel after it forms increases with increases with co-flow temperature, and the flame speeds are slightly higher the predicted adiabatic laminar flame speeds, possibly increased due to the low RMS velocity fluctuations previously characterized in Chapter 3. Also in the continuous flame mode, it was shown that the characterization used to define an autoignition kernel is valid as the jumps upstream correspond to speeds too fast to be flame

propagation.

The location of ignition kernel initiation was determined for each instance of autoignition kernel for each flow condition using both OH* chemiluminescence and OH PLIF, which provides statistical insight of the autoignition delay times. These results provide sufficient agreement for ignition delay times. It was shown that the OH PLIF method gives a higher number of autoignition kernels of smaller size than was observed using OH* chemiluminescence. This could be due to the line of sight nature of chemiluminescence showing kernels throughout the test section as a single larger kernel, or the sensitivity of the OH PLIF to OH concentration could be higher than the intensity needed to show a kernel in chemiluminescence imaging.

While the measured average ignition delay times from OH* chemiluminescence gave values almost exclusively faster than the calculated MRMF results for prevaporized, premixed Jet-A, it is likely that those averages times are biased by kernels experiencing pockets of higher temperature flow. The maximum ignition delay times give results that more closely agree with calculated times and previous results in the literature using time-average methods. The highest temperature flow condition did agree with the most reactive mixture calculated time and did not produce kernels associated with higher temperatures as the kernels supported a stabilized flame at these conditions. A calculation of characteristic times shows that the droplet heat-up time is on order with the chemical time at that flow temperature and any deviations from average temperature to higher temperature would be limited by droplet heat-up times.

CHAPTER 5
ANALYSIS OF AUTOIGNITION KERNEL BEHAVIOR IN THE PRESENCE OF LIQUID DROPLETS

This chapter combines the findings of the autoignition statistics results with analysis from the fuel spray characterization and low order modeling in order to elucidate the local conditions that control the behavior of ignition kernels in a polydisperse fuel spray. These results are compared to the autoignition initiation location statistics from the OH* chemiluminescence. Next, example behavior of individual kernels is shown from the UV PLIF imaging results. The characteristic timescales with an expanded calculation of total droplet lifetime is calculated and used to inform the results of the UV PLIF data sets. Finally, the statistics of kernel formation with relationship to visible droplets is shown and the results are further investigated for insight on the droplet dependence of autoignition kernels.

5.1 Comparison of Fuel Spray with Autoignition Kernel Initiation Locations

The location of autoignition kernel initiation as determined by the chemiluminescence imaging is shown in Figure 5.1, along with the results of mean diameter, axial velocity, and data rate from the PDPA measurements. The chemiluminescence results were shown previously in Chapter 4, while the fuel spray characterization was discussed in Chapter 3. The left set of images was obtained with the tapered fuel injector while the right set of images is with the blunt fuel injector. The PDPA measurements were taken at essentially the same average flow conditions as the ignition results. So the droplet measurements at $20mm$ correspond to the region of the spray where we have the earliest onset of autoignition for these conditions.

Ignition rarely occurs in the center of the spray. For some reason, this region of low droplet density (based on the data rate) and where the droplets are small, is not conducive

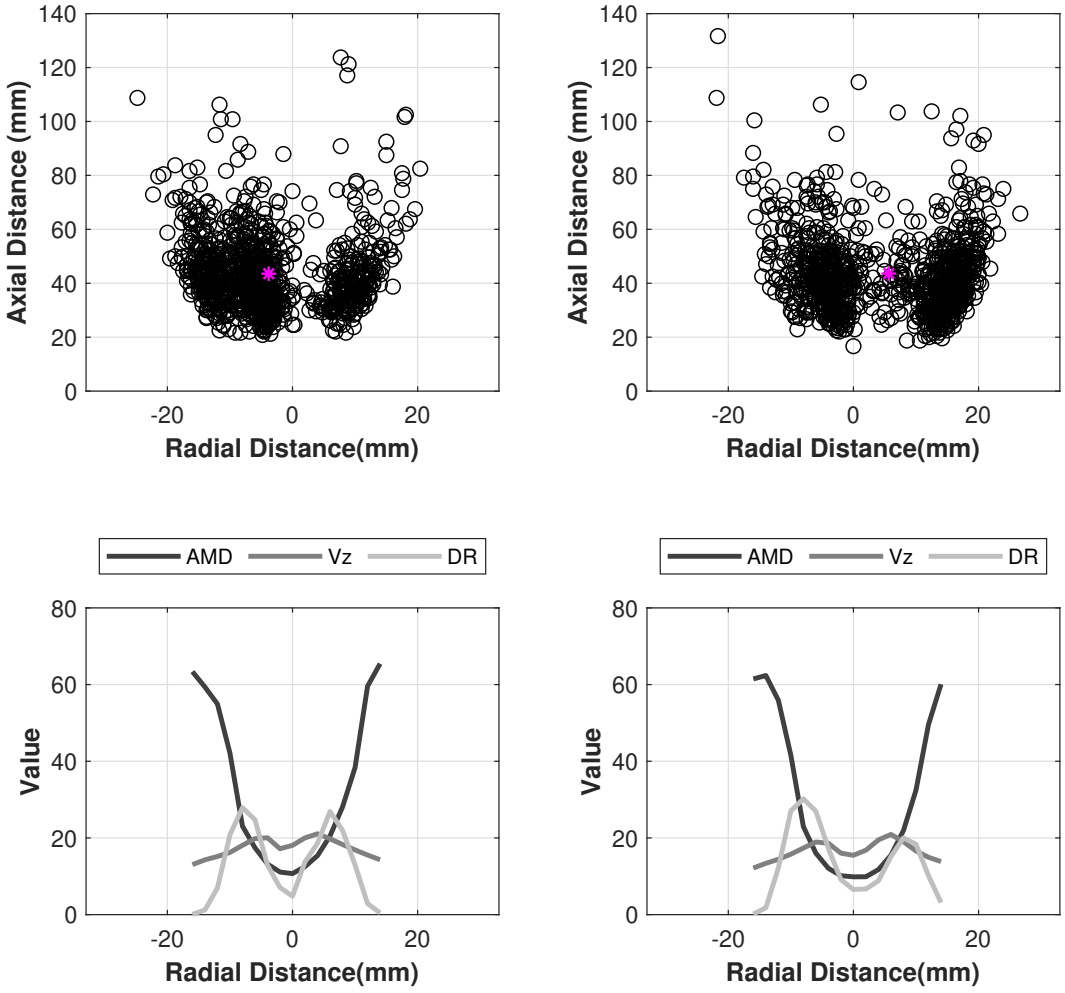

(a) Tapered fuel injector,
PDPA at $37m/s$ and $1145K$,
OH* at $42.2m/s$ and $1145K$

(b) Blunt fuel injector,
PDPA at $37m/s$ and $1145K$,
OH* at $43.5m/s$ and $1146K$

Figure 5.1: Comparison of OH* chemiluminescence autoignition events to PDPA measurements at $20mm$ downstream of fuel injection

to autoignition kernels. Where we see the autoignition kernels occurring most often aligns with the dense spray region where the droplets are larger.

5.2 Analysis of Droplet Characteristic Timescales

The measured fuel spray characteristics, fully described in Chapter 3, show a wide range of droplet conditions in this polydisperse spray. Three notable regions of the spray are: the center, the dense spray, and the (outer) spray periphery. The center of the spray characteristically consists of small droplets with a narrow size distribution (for example with the tapered injector, the mean diameter is around $11\mu m$ and the full-width at half maximum of the distribution is $11\mu m$), low velocity (compared to the dense spray region), and a low droplet density, with the latter observation based on the especially low data rate from the PDPA measurements (though this could be partly attributed to the low velocity in this region). The dense spray region, identified by the maximum PDPA data rate, has larger droplets (again for the tapered injector, mean diameters around $32\mu m$ close to the injector but decreasing downstream), with higher velocities. The periphery of the spray is dominated by large droplets (mean diameters typically greater than $40\mu m$). Furthermore, the autoignition locations reported in Chapter 4 suggest that autoignition rarely if ever initiates near the spray periphery; so that region will not be analyzed in this chapter.

Total ignition delay time in a liquid fueled system is dependent on the time for droplet heat-up and vaporization, and chemical reaction. Any of these processes could be a limiting timescale for ignition delay depending on the conditions. Therefore, characteristic droplet times were calculated based on initial droplet size measurements and residence times of average droplets were calculated based on the PDPA droplet velocity measurements as a function of axial distance. The estimate uses the measured velocity at each axial distance to calculate the residence time from the previous distance and gives a total residence time to reach an axial location $20mm$ from the fuel injection plane, which is the farthest downstream measurement location in the hot flow where PDPA data is available. It is also the

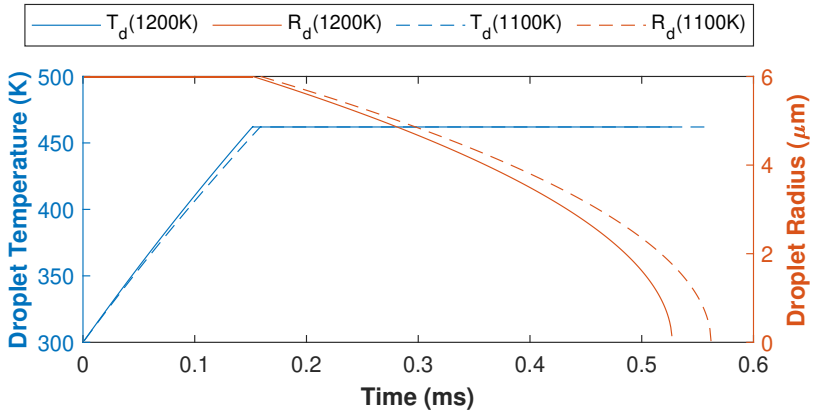

(a) Initial droplet diameter of $12\mu m$ corresponding to centerline average droplet size

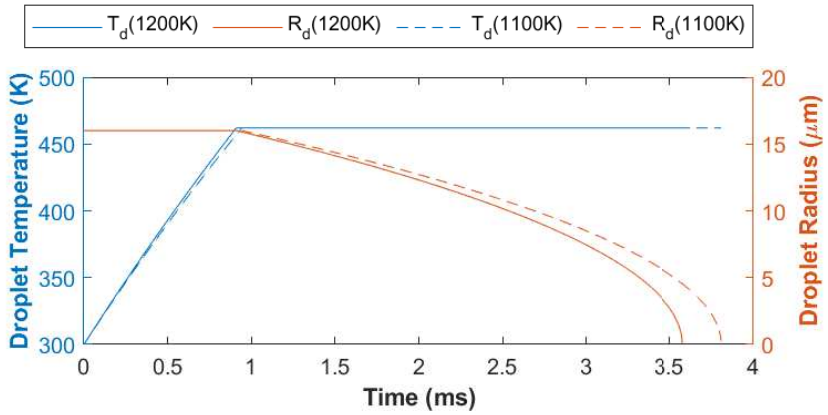

(b) Initial droplet diameter of $32\mu m$ corresponding to dense spray streamline average droplet size

Figure 5.2: Calculated droplet heat up and vaporization as a function of residence time; co-flow at $1200K$ $1100K$ and $40m/s$ with initial droplet temperature of $300K$ and initial droplet velocity of $15m/s$

axial location at which kernels first begin to form at elevated temperatures.

For a droplet that follows the centerline streamline, the total residence time would be approximately $1.44ms$ to reach this location. For comparison, a droplet following the streamline corresponding to the maximum data rate (i.e., in the densest region of the spray), experiences an average residence time that is only slightly shorter, approximately $1.31ms$. Though the axial distance traveled in both cases is the same, the dense spray streamline is elliptic and moves radially out from the center, so these droplets also travel a greater distance.

The characteristic times required for a droplet to heat-up to a prescribed vaporization

temperature, and the vaporization time required to fully evaporate the droplet were calculated for average sized droplets moving along the same streamlines identified above, those following the centerline and the most dense region of spray. The models used to calculate these characteristic times and their assumptions are described in Chapter 2. The earliest average droplet size measured was at an axial plane $5mm$ downstream of the injector. For lack of better information, these values were used to estimate the initial droplet size. The results are shown in Figure 5.2 for a co-flow temperature of $1200K$ and $1100K$, in order to compare the effect of temperature on these characteristic times.

For the small droplets that dominate the centerline of the fuel spray (Figure 5.2a), the droplet will heat up and completely evaporate in just over $0.5ms$. This is much less than the $1.4ms$ residence time required to reach $20mm$, so we would expect almost all of the fuel to be in vapor form at $20mm$. In fact, the droplets should vaporize by the time they have traveled approximately $6mm$ downstream. For the larger droplets that exist along the most dense spray streamline (Figure 5.2b), it takes approximately $1ms$ just to heat the droplets to a temperature where the vaporization rate becomes significant. Furthermore at $1.3ms$, which is the time required to reach $20mm$ downstream, these large droplets will have just begun to vaporize. A single droplet that was initially $32\mu m$ in diameter would have shrunk to just $29.7\mu m$ and lost $2.8ng$ of fuel (or 3% of its total mass). For comparison, a single $12\mu m$ centerline droplet that has fully evaporated contributes just $0.72ng$ of fuel vapor. So even though the larger droplets in the dense spray region have barely begun to vaporize when they have reached $20mm$ downstream of the injector, the center of the flow should have a much lower fuel concentration due to its low number density and small droplet sizes. These results are minimally affected by a change in co-flow temperature. As expected, a decrease in temperature increases the total lifetime of the droplet with the significant portion of that change attributed to the change in vaporization time.

Figure 5.3 shows the calculated ignition delay times for cold ($300K$) fuel vapor mixed with hot, vitiated oxidizer at two oxidizer temperatures, corresponding to the lower and

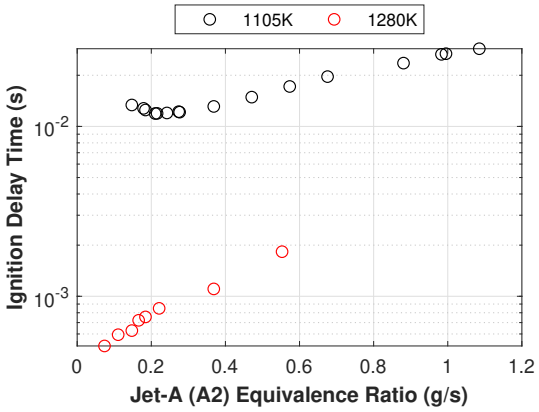

Figure 5.3: Ignition delay time as a function of Jet-A equivalence ratio in order to evaluate the most reactive mixture fraction at low and high temperatures

higher range of the mean flow temperatures used in the experiments. Results are shown for a range of fuel-oxidizer mixtures. These calculations are done using the approach outlined in Chapter 2. For a co-flow (oxidizer) temperature of $1105K$, the results reveal a clear minimum ignition delay that defines a most reactive mixture fraction at $\phi_{Jet-A} = 0.22$ with a delay just over $10ms$. At the higher temperature ($1280K$), the ignition delay continues to decrease with decreasing fraction of Jet-A. Furthermore, the ignition delays become quite short, less than $0.5ms$, below $\phi_{Jet-A} = 0.07$. However, there is little temperature rise due to combustion at these quite low equivalence ratios (e.g., less than $50K$ at $\phi_{Jet-A} = 0.07$). Thus at high temperatures, we could expect autoignition would occur shortly after the fuel starts vaporizing for larger droplets (e.g., $32\mu m$). For small droplets (e.g., $12\mu m$), on the other hand, significant evaporation could occur before ignition might become observable.

5.3 Examples of Observed Behavior

As discussed in the previous chapter, the integrated nature of chemiluminescence makes it difficult to accurately compare to the planar Mie scattering data or the spatially resolved PDPA results; so the UV PLIF data is analyzed here to look for similar behavior with planar autoignition measurements. An example time sequence of UV PLIF images is shown in Figure 5.4 for an intermediate co-flow temperature of $1211K$. The images obtained from

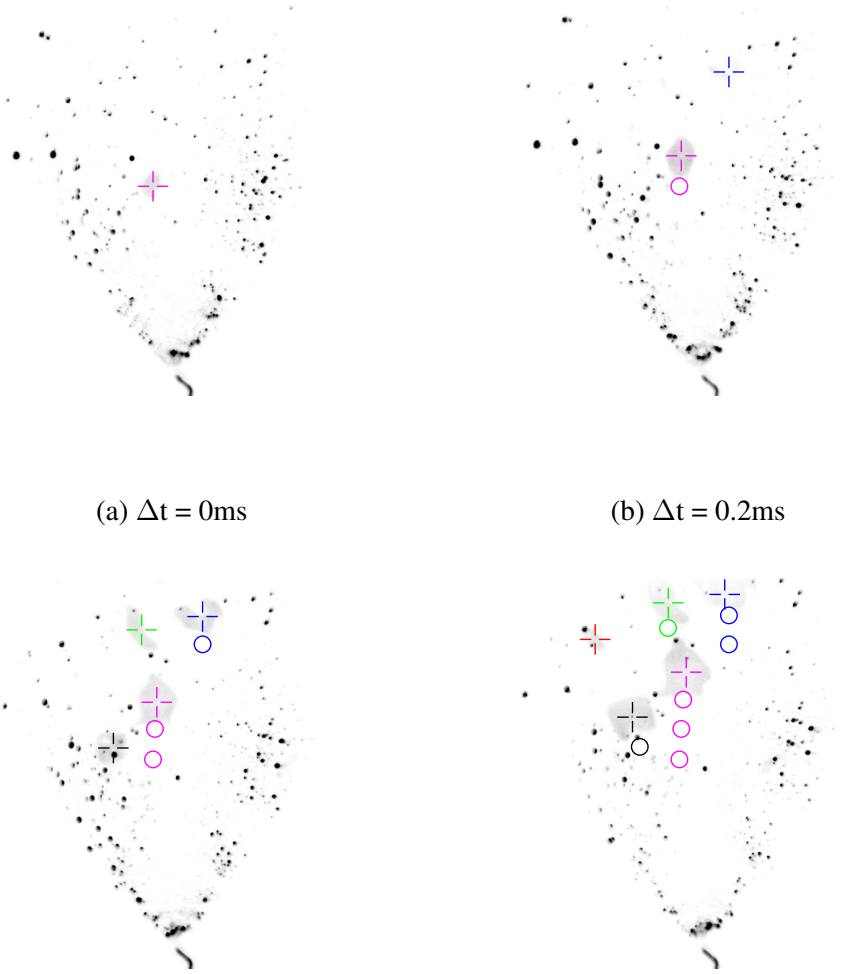

(a) Δt = 0ms

(b) Δt = 0.2ms

(c) Δt = 0.4ms

(d) Δt = 0.6ms

Figure 5.4: An example time history of UV PLIF at $1211K$ and $33m/s$

the intensified cameras are inverted in this display for ease of viewing. Using the method described in Chapter 2 to differentiate the OH PLIF signal from the fuel fluorescence, ignition kernels are identified and their center is indicated by a cross. Different colors are used to track different kernels in time, and the location of a kernel from the previous images is shown on an image with an open circle of the same color. This provides a visualization of the path of each kernel.

In the 0.6 ms time period represented by this example, a total of five ignition kernels

formed. The first kernel to form is identified by the magenta color; it appears in the first frame and contains one identifiable fuel droplet (or cluster of small droplets that are unresolved by the imaging optics) near its most upstream edge. As this kernel grows in the next two frames (lasting 0.4 ms), the droplet signal decreases and becomes undetectable. This suggests the fuel has evaporated, and possibly been consumed by the kernel; though it is also plausible that the small droplet has moved out of the thin laser sheet. Based on an estimated sheet thickness of 0.4 mm, and assuming a droplet initially centered in the sheet, a small droplet could leave the laser sheet in this time if its velocity was greater than 1 m/s. In the last frame (0.2 ms further along), this kernel is shown to have grown towards two clearly identifiable liquid fuel droplet structures while also engulfing a third droplet.

The second kernel observed to form, marked by the blue symbols, is not round when first observed, but rather appears as a thin arc, convex relative to the upstream direction, with no visible liquid fuel in the adjacent region. Though there are two droplets downstream of the kernel. It is also the kernel that forms the furthest downstream of any of the kernels identified in this image sequence. In the next frame (0.4 ms), the kernel has grown to engulf the left fuel droplet, while the right edge is approaching the second droplet. Thus it appears this kernel formed in a region where fuel has completely vaporized. Furthermore, the shape of the kernel would suggest either a few regions of fuel-air mixture have nearly simultaneously ignited and grown together to form this kernel. A more likely interpretation is that the kernel is growing non-spherically because it has formed and is growing into the flammable fuel-air mixture produced by the wake of the two droplets just downstream of the kernel. The fact that the kernel grows primarily towards these two droplets supports this interpretation.

The kernel formed in frame 3 and identified by the black cross is formed containing 3 visible droplets and a "hole" within the kernel. As this kernel grows and moves downstream, it leaves behind a large droplet that may have been associated with the hole while the other droplets contained within the kernel dim. This example shows that kernels formed

at the same flow conditions, and even at the same time instances can have different droplet interaction, and some kernels proceed towards droplets while others do not. It is also observed that center of the kernels are traveling downstream at speeds approximately 22-25 m/s, potentially slowed by the wake of the fuel injector or slower droplet injection velocities. More examples of the first appearance of autoignition kernels and their subsequent evolution are shown in Appendex A.

Figures 5.5 and 5.6 show similar time histories but now for the highest temperature case, the "continuous flame condition, for the tapered and blunt fuel injectors. The time step between frames shown is $0.4ms$, meaning one frame of recorded data is omitted between each consecutive frame shown in the figure. Compared to the results of Figure 5.4, where the conditions corresponded to the periodic kernel regime, the kernels in the "continuous" regime grow much faster into large kernels that wind throughout the fuel spray.

The initial frame of Figure 5.5 shows three kernels. The right-most of the three kernels, designated by the green markers, appears to grow and lose intensity in the next frame, while the kernels around it grow into larger flame structures and new kernels are formed nearby that grow in time. The bottom-left kernel formed in the first frame, shown by magenta markers, grows in the second frame and some of the droplets that were present downstream of the kernel disappear, presumably evaporating the droplets due to the high temperature of the burning kernel and consuming the fuel. For a droplet to evaporate in the $0.4ms$ between frames, it would have to be $\leq 13.25\mu m$ in size at a flow temperature of 1300K or $15\mu m$ for a flow temperature of $2000K$. As was previously shown with the droplet lifetime model, the effect of temperature is slight on droplet lifetimes.

The majority of kernels that are formed in this example have an interaction with droplets at the time they are first observed and as they propagate. The kernels and their subsequent flame propagation are preferentially located off the centerline of the test section for most times. According to the previously shown chemiluminescence, there will eventually be combustion in the center. These OH PLIF results are shown for a lower overall equivalence

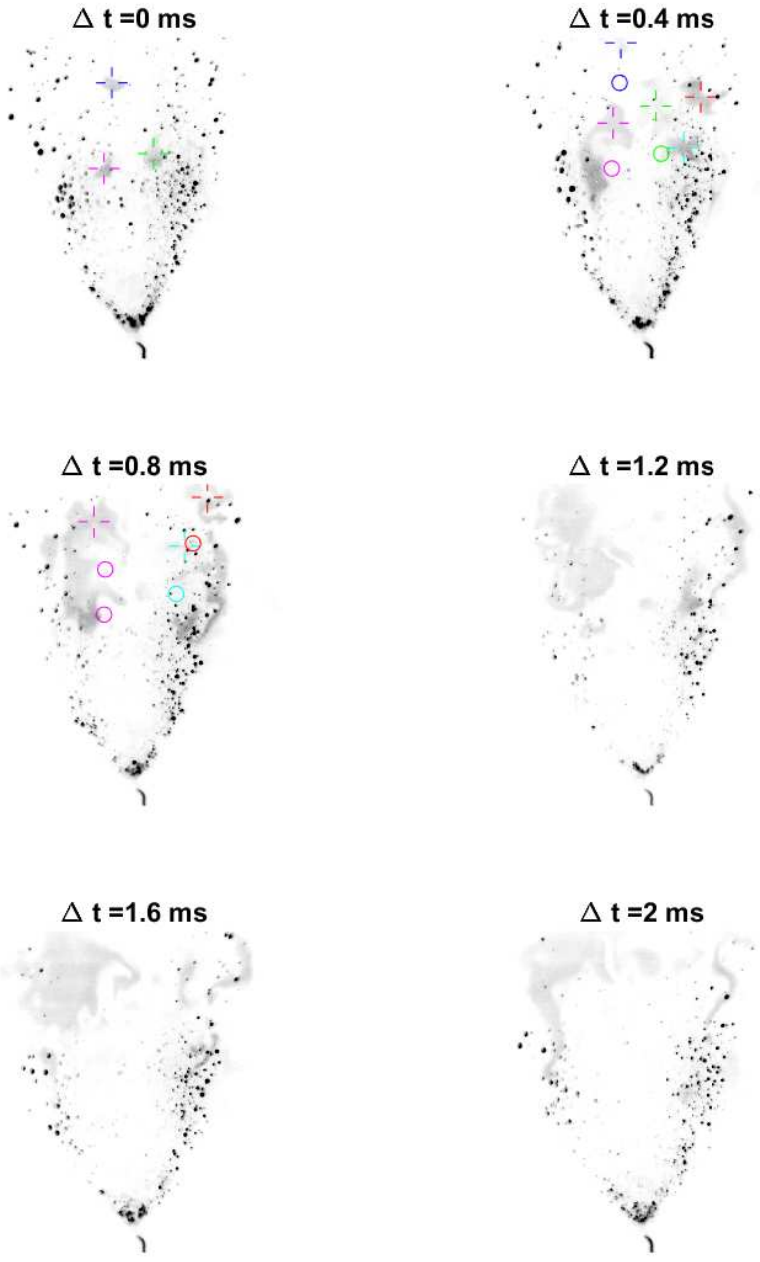

Figure 5.5: Time sequence of images at conditions of continuous flame behavior, T = $1272K$, u = $33m/s$, with tapered fuel injector. Time between images shown is $4ms$, there is one frame between each image set not shown

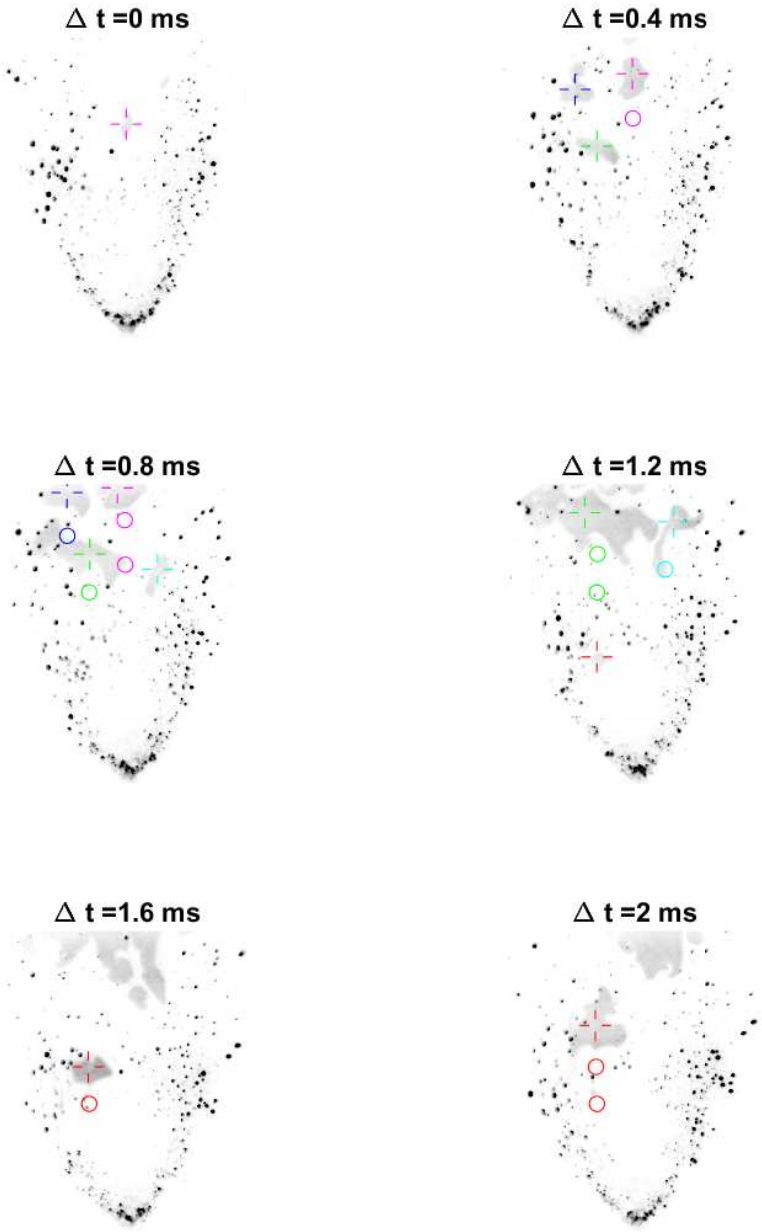

Figure 5.6: Time sequence of images at conditions of continuous flame behavior, T = $1204K$, u = $35.4m/s$, with blunt fuel injector. Time between images shown is $4ms$, there is one frame between each image set not shown

ratio, φ_{Jet-A}=0.7, than the OH* results at stoichiometric equivalence ratio. So the behavior of two conditions shows little dependence on Jet-A flow rate over this small range of equivalence ratio. A lower Jet-A equivalence ratio in this experimental system implies a lower pressure drop across the fuel injector which would most likely result in lower droplet velocities.

If the small droplets in this region are vaporizing completely but not producing enough fuel vapor to initiate autoignition in the time before kernels initiated off center will propagate to the center, autoignition kernels would not be visible in this center region. The fuel would be combusted through flame propagation before any autoignition event could occur. It can also be observed, specifically for the kernel designated by the magenta markers, that the upstream edge of the combustion event as it convects downstream does not move significantly with time. At these temperatures and a lower co-flow velocity, it is likely the laminar flame speed (Figure 4.8) could match the flow velocities, especially in the region of slower flow near the injector.

There are some similarities between the results from the two injector shapes. For one, we see distinct kernels, disconnected from previously burned combustion regions. This implies that even in the continuous flame regime, where the line-of-sight integrated chemiluminescence indicated the appearance of a stabilized flame, the flame is still initiated by autoignition events rather than flame propagation. In other words, we have an autoignition stabilized spray flame at these elevated temperatures. As a reminder, there are no significant recirculation zones in the facility, especially with the tapered fuel injector. At the lower $33m/s$, is possible the gas velocities match the laminar flame speeds at these high-temperature conditions, while the higher velocity should exceed laminar flame speeds. Despite the nearly constant upstream edge of the magenta kernel and proceeding propagation, there are kernels that form upstream of that edge at both 1.2 and $1.6ms$. Overall, regardless of whether droplets are present when kernels are first observed, as they grow they propagate towards nearby droplets in a nonhomogeneous manner. Based on the fuel PLIF, large

droplets decrease in number when large kernels are present. For example in the Δt=0ms frame, there are many large droplets present in the upper left hand corner of the image. Despite the total intensity of the spray flurorescnece appearing to be nearly constant, that region has less droplets when an autoignition event propagates through the region in times 1.2 to 2ms. Some of the large droplets remain present but there are few smaller droplets, especially on the interior of the combustion event.

It is interesting to compare results for the two injector shapes at the same continuous flame conditions. For the tapered fuel injector, there is little combustion near the test section centerline, even near the downstream edge of the interrogation region (roughly 60mm from the fuel injector). There is occasionally combustion in the center of the spray but the majority of combustion is off center. For the blunt fuel injector, ignition kernels form in similar locations to the tapered injector, off center, but now combustion is able to propagate to the center of the spray. This suggests a more flammable mixture in the central flow region for the blunt injector. Furthermore as seen in Figure 5.6, more detectable fuel droplets are observed in the center of the spray for the blunt fuel injector. The main differences observed in the flow around the fuel injectors is the increased wake size and lower average velocities for the blunt design. The stronger recirculation zone in the wake of the blunt injector could increase mixing and potentially droplet or evaporated fuel entrainment back into the wake of the fuel injector from the denser spray region. This would increase the amount of fuel vapor that convects downstream in the center of the flow. This would make the center of the flow more flammable, despite the similarly measured average spray properties. Although the droplets in the center of the flow were already expected to have evaporated by the time autoignition occurs downstream, the lower velocity region with recirculation experienced in the wake of the blunt injector could allow more time for fuel to mix regions of higher fuel vapor concentration in the dense droplet regions of the spray.

5.4 Analysis of Droplet Kernel Interaction

The examples of instantaeous images shown in the previous section suggest that some kernels are initiated with a visibile droplet interaction while others are not. This section evaluates the total kernels identified for each flow condition and looks for trends in droplet interaction. In Chapter 4, the locations of autoignition kernel initiation were discussed for the UV PLIF data. The kernel scatter results are replicated here in Figures 5.7 through 5.9 with droplet interaction identified. For each kernel, it was determined whether a droplet was visibly interacting with the kernel on its first appearance, either inside or touching the boundary of the kernel. Kernels have either a droplet present (o) or no droplet (*), with the no droplet kernels further identified by whether (green) or not (blue) they fall within the region of dense fuel spray. The region of dense fuel spray was identified by thresholding the average image, and the boundary is shown superimposed on that image. It is important to note that while the OH* chemiluminescence data was collected at an overall stoichiometric fuel-air ratio, the UV PLIF data is overall fuel-lean with an overall equivalence ratio of 0.7.

For the $43m/s$ co-flow with tapered fuel injection, there is a distinction in autoignition locations and droplet interactions. Kernels with droplets occur primarily in the dense region of the fuel spray or just within that region, while kernels without droplets occur primarily outside the region of dense droplets. This observation does not hold when the co-flow velocity is decreased.

As the co-flow velocity is decreased from 43 to $33m/s$ (Figures 5.7 and 5.8), the spray widens slightly. With the change to a blunt fuel injector, the fuel spray widens further. This impacts where autoignition kernels initiate. The chemiluminescence data discussed in Chapter 4 showed that as velocity changes, the leading edge of autoignition is controlled mostly by convection; similarly, a decrease in velocity caused the range of kernel initiation locations to increase. As expected, the PLIF results also show that the kernels initiate farther upstream when the convection velocity drops. They also reveal, however, that the

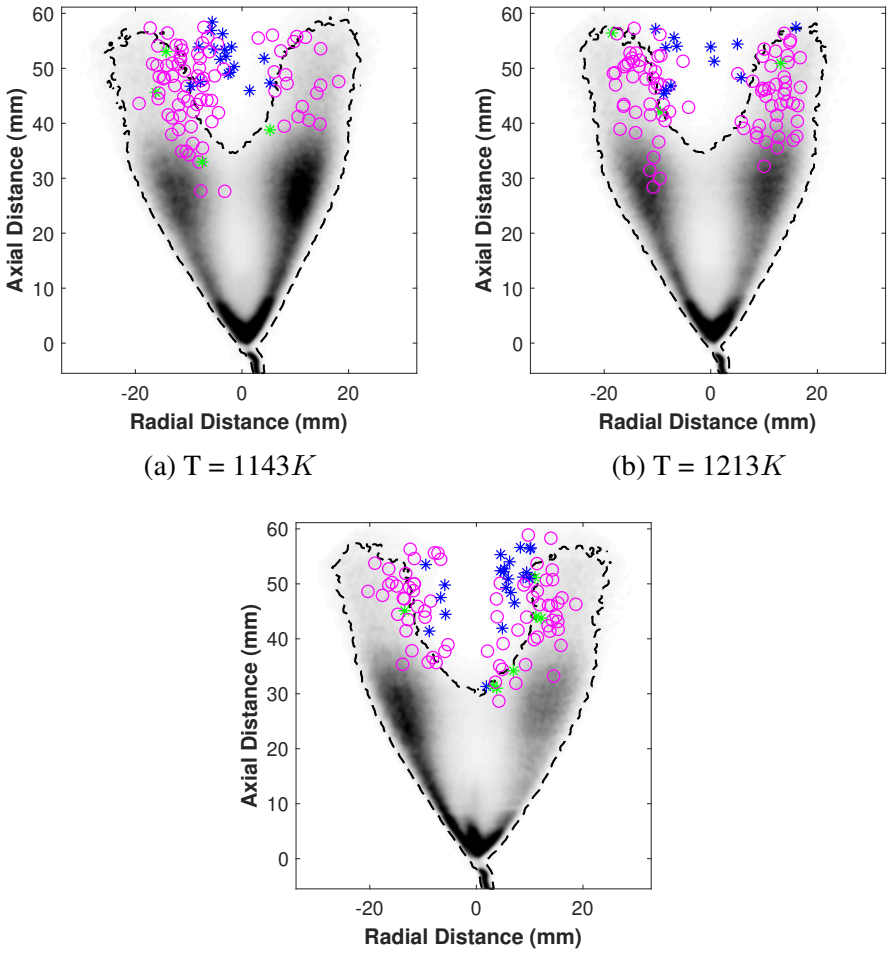

(a) T = 1143K

(b) T = 1213K

(c) T = 1280K

Figure 5.7: Autoignition kernel initiation locations for UV PLIF at 43m/s distinguished by droplet(o) or no droplet(*), with no droplet occurring either within (green) or outside (blue) the dense fuel spray region

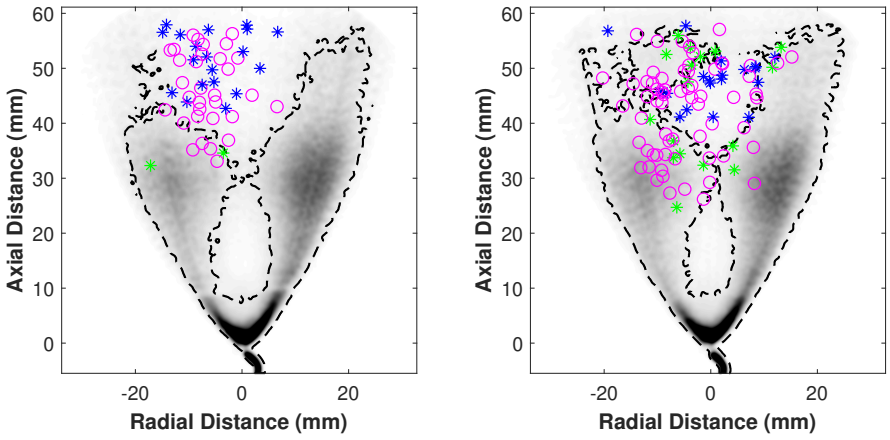

(a) T = 1106K (b) T = 1137K

(c) T = 1211K (d) T = 1272K

Figure 5.8: Autoignition kernel initiation locations for UV PLIF at 33m/s distinguished by droplet(o) or no droplet(*), with no droplet occurring either within (green) or outside (blue) the dense fuel spray region

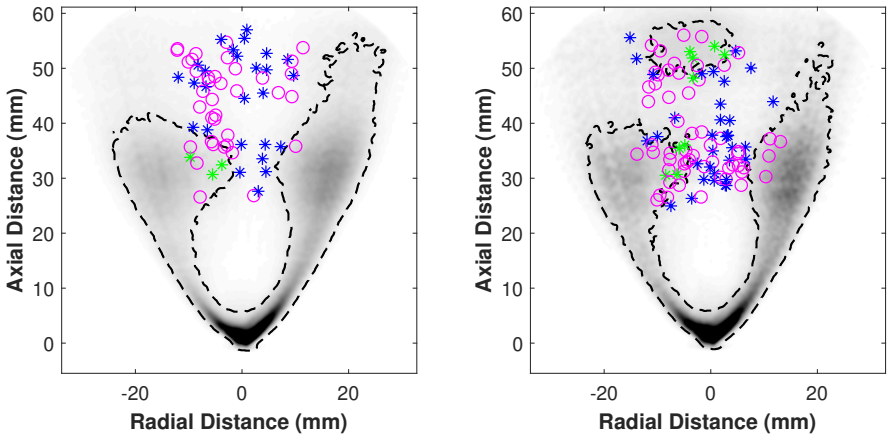

(a) T = 1138K, u = 31.8m/s

(b) T = 1180K, u = 34.2m/s

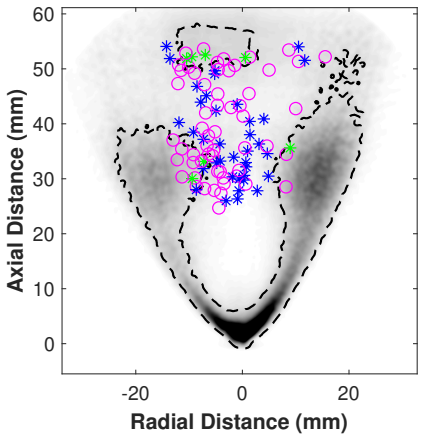

(c) T = 1204K, u = 35.4m/s

Figure 5.9: Autoignition kernel initiation locations for UV PLIF distinguished by droplet(o) or no droplet(*), with no droplet occurring either within (green) or outside (blue) the dense fuel spray region

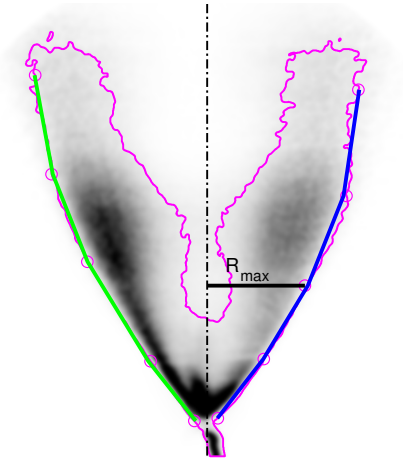

Figure 5.10: Definition of R_{max}, the radial distance of the edge of the dense fuel spray

probability increases of finding a kernel initiate in the center of the flow for the lower speed flow. At a lower velocity, but constant temperature, the (ideal) chemical time should remain the same, so kernels will ignite farther upstream.

In order to better visualize the behavior of droplet interaction as a function of radial distance in the spray, the radial locations of kernel initiation are normalized by the maximum radius of the dense spray at that axial distance. Figure 5.10 illustrates the definition of R_{max} for an average image of UV PLIF. The same thresholding is shown as was used in the previous scatter images. The centerline is drawn directly downstream from the center of the fuel injection. Five locations were chosen on the outer edge of the spray as determined from the thresholding, and a 2nd order polynomial was used to fit these curves for the left and right side, allowing for the possibility of asymmetric behavior. Now at each axial location, the curve fits give an R_{max} that quantifies the outer edge of the dense fuel spray.

The number of kernels observed for each radial location is shown in Figures 5.11 through 5.13. The histograms are stacked to differentiate between: 1) kernels that appear with a droplet interaction, 2) kernels that have no droplet and occur within the dense

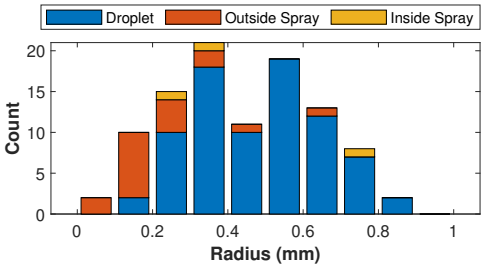

(a) T = 1143K

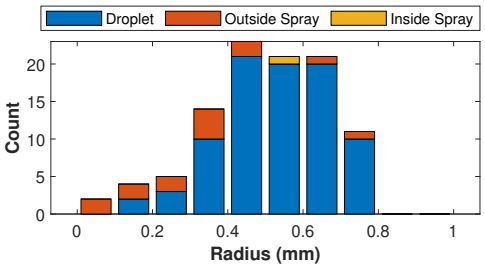

(b) T = 1213K

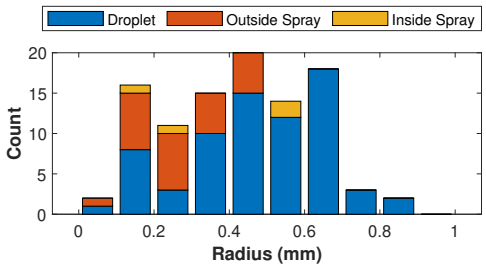

(c) T = 1280K

Figure 5.11: Histogram of normalized radial location of autoignition intiations for UV PLIF at 43m/s with tapered fuel injector, distinguished by droplet, no droplet occurring either within or outside the dense fuel spray region

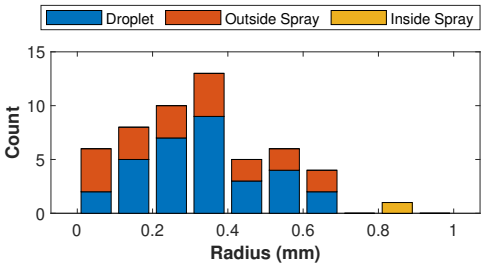

(a) T = 1106K

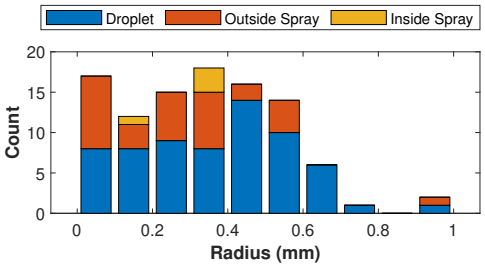

(b) T = 1145K

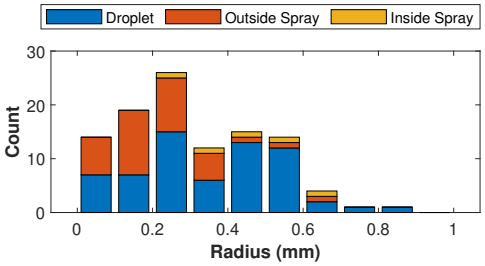

(c) T = 1206K

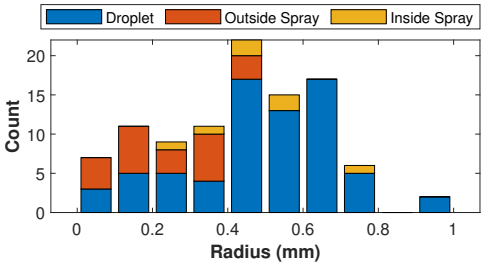

(d) T = 1317K

Figure 5.12: Histogram of normalized radial location of autoignition initiations for UV PLIF at 33m/s with tapered fuel injector, distinguished by droplet, no droplet occurring either within or outside the dense fuel spray region

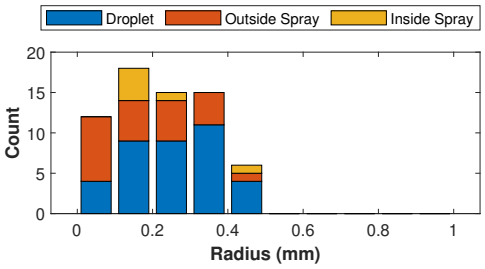

(a) T = 1138K, u = 31.8m/s

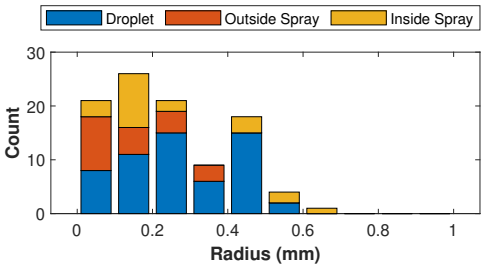

(b) T = 1180K, u = 34.2m/s

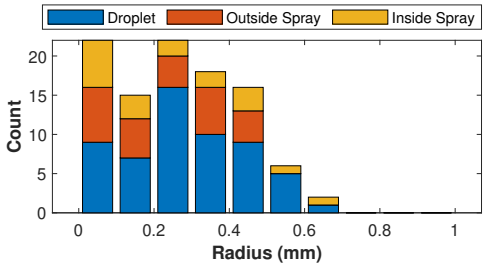

(c) T = 1204K, u = 35.4m/s

Figure 5.13: Histogram of normalized radial location of autoignition locations for UV PLIF with blunt fuel injector distinguished by droplet, no droplet occurring either within or outside the dense fuel spray region

fuel spray, and 3) kernels that have no droplet and occur outside of the dense spray. For the tapered fuel injector at 43m/s, which corresponds closely to conditions for the OH* chemiluminescence results, kernels are less likely to occur near the center of the fuel spray, as was shown by previous results. Kernels do not appear beyond a normalized radius of 0.9, i.e., at the outer edge of the fuel spray. Furthermore, droplets without a kernel are more likely to occur more towards the center of the fuel spray, where droplets are not as frequently observed in the UV PLIF imaging.

As the co-flow velocity drops, kernels become more likely to occur towards the center of the fuel spray. It is still characteristic that the kernels without droplets are occurring more skewed towards the center of the fuel spray. For the blunt fuel injector data shown in Figures 5.9 and 5.13, there is a region at the top of the field of view, directly downstream of the fuel spray centerline, that gives a signal on the average image unlike the other conditions. The instantaneous images shown in Figure 5.6 show that there may be a few more droplets in that region of the fuel spray as compared to the tapered fuel injector, but pos-

sibly more significantly, there is combustion towards the center of the fuel spray that does not occur for the tapered fuel injector.

It was noted previously from qualitative observation of the averaged images that the fuel spray widens with a change from tapered to blunt fuel injector for the $33m/s$ data sets. The histograms for this data set show that compared to the maximum radius of the dense spray, the kernels all occur closer to the centerline than for the tapered fuel injector. This most likely is a results of the increased wake dynamics due to the larger blunt injector shape.

5.5 Discussion

Based on the literature review, it was suggested that autoignition of sprays could manifest in many different modes. The kernels observed in this polydisperse spray that ignite with droplets present are exhibiting behavior most closely described by the theory of cloud ignition. The kernels form in a small region with multiple droplets present, referred to as cluster ignition.

In the examples shown, autoignition kernels seem more likely to appear near smaller droplets and propagate towards the large droplets. There are small and large droplets that are still present in the vicinity of autoigniton kernels. Autoignition kernels do not form near the periphery of the spray where very large droplets are present. The large droplets in the periphery, with an average size of $60\mu m$ and larger, require more time to heat up than the residence time associated with reaching $20mm$ from the injector, and thus have not begun to vaporize. The smaller droplets in the center have already vaporized since they have a very short lifetime. The lack of autoignition kernels in the center of the spray likely corresponds to a region of vaporized small droplets leading to insufficient fuel concentration to produce significant heat release and then fast reaction rates. Thus no autoignition is observable at sufficiently upstream locations at some flow conditions. The results of the droplet heat up and vaporization calculations show that the small droplets that are located in a region of less

dense fuel spray will likely have evaporated less mass in the same time, and therefore, be more likely to find leaner equivalence ratios in that region. The regions on the periphery of the spray will have no fuel vapor while the center is likely too lean to support autoignition. In this case, there could be autoignition reactions in the center, but they are not detectable at such low fuel concentration.

Looking at the examples of kernels from UV PLIF shown in this chapter, there do not seem to be an examples of autoignition kernels behaving as indivual droplet flames. As mentioned previously, more examples of kernel initiation are shown in Appendix A. There is a single kernel for Frame 172 of the PLIF-07 set of images where autoignition appears first in the "wake" of a large droplet. This type of kernel seems the closest example of a single droplet supporting an autoignition kernel. In the subsequent frame, the kernel has grown in size and intensity and the droplet is no longer present, having been consumed or traveling out of the plane of the laser. Frame 19 of PLIF - 10 shows a second example of this same behavior. This kernel initially formed in the vaporized fuel wake of a single droplet; in the next frame, it overtakes three droplets that were previously downstream of the kernel and now encompasses four droplets in total. Overall, there are a very limited number of kernels with this behavior and this behavior is very similar to that of the cloud ignition that is most often observed.

All of the droplets observed in this spray are smaller than droplets typically used for single droplet autoignition studies, and it is likely that that this spray is dense enough that droplet interactions and group autoignition are more likely than single droplet autoignition. The kernels shown and discussed here do show involvement with multiple droplets, and regions between droplets, suggesting that droplet interaction is important in determining the likelihood of autoignition kernels. The wide range of flow mixture and temperatures present due to two-phase flow allow for more possible paths for the autoignition events to grow along.

In general, it has been shows that droplet distribution and local droplet wakes play an

important role in the location of autoignition kernel initiation and even more so in the propagation of these kernels into flames. The balance between local cooling due to vaporization, most reactive mixture rate, and high temperature spots from the vitiated flow is likely to control the location of autoignition initiation locations.

CHAPTER 6
SUMMARY AND CONCLUSIONS

This chapter summarizes the work described in this thesis and lays out the contributions and implications of this work. Additionally, the suggested future work is presented.

6.1 Summary of Work Performed

Previous work has proposed a number of ways for a fuel spray to autoignite, such as ignition of single droplet flames and cloud ignition. The majority of experimental liquid-fueled autoignition studies, however, have been parametric in nature, focusing on ignition delay and describing its dependence upon parameters such as droplet size, flow rates, and turbulence intensity. Little has been done to investigate the local behavior of autoignition.

The current work explored autoignition in a specially developed test facility that is capable of reproducing important flow conditions in a gas turbine reheat combustor. The flow was characterized in detail in order to understand the conditions under which autoignition is occuring, and to provide sufficient information for future modeling efforts. Results show the co-flow is uniform on average, with an expected trapezoidal profile and wake downstream of the injector body in the flow. Velocity profiles downstream of the fuel injector shapes show wakes dependent on the bluntness of the shape, with the maximum wake formed by the blunt shape. PIV suggests that there are flow non-uniformities in the center of the flow that could correspond to poorly mixed dilution air with vitiated product forming higher temperature pockets in the flow. Droplet measurements show a region in the center of the spray with small average droplet size, narrow droplet distribution and low data rate. The majority of droplets are produced in a region approximately halfway between the center of the spray and the periphery and droplets here have an intermediate average size of $30\mu m$. The shape of fuel injector primarily affects the droplet velocity at axial locations

less than $15mm$ from the fuel injector, which is just above the boundary of the recirculation zone.

High speed chemiluminescence was used to determine the statistical nature of autoignition events, primarily where ignition occurs, and the dependence on the vitiated flow temperature and velocity. In order to elucidate the behavior of autoignition kernels in relation to droplet distribution, UV PLIF was used to simultaneously visualize autoigniton kernels and fuel spray in a plane that bisects the test section through the center of the fuel spray.

6.2 Contributions and Implications

This thesis provides an extensive data set of detailed measurements of autoignition in a polydisperse spray at conditions relevant to gas turbine reheat combustors. Limited previous studies of local autoignition are at lower temperatures and with few droplets present in the autoignition regions. Both the vitiated flow and liquid spray were extensively characterized in order to provide a complete understanding of the flow conditions. While this data set is lacking in temporal or spatially resolved vitiated flow temperature measurements, it was shown that understanding the non-homogeneities of real systems and flow fields is important when characterizing autoignition. The time-averaged flow fields appear uniform, however fluctuations in temperature and mixing, as suggested by non-uniform seeding particles, lead to a wide range of observed autoignition delay times. Hot spots and non-uniform reaction rates due to non-homogeneous fuel-air mixing can lead to ignition delay times shorter than predicted, based on average conditions. Furthermore, ignition delay times determined using time-integrated approaches can fail to detect these events. While parametric studies of ignition delay time using averaged quantities have their place in understanding combustion mechanisms and surrogate fuels, in order to fully understand the underlying physics, it is important to include to the spatial and temporal response of autoignition delay times.

A major novelty of this work is the application of spatially and temporally resolved,

modern diagnostic methods to examine the behavior of autoignition of a well-characterized polydisperse fuel spray at high temperatures. Modern diagnostics allowed for the visualization of autoignition events that had not been previously characterized in order to compare their behaviors to different modes predicted in the literature. Four primary observations of autoignition kernel formation and propagation were observed.

Autoignition kernels more often form in the presence of a fuel droplet and often multiple fuel droplets, which is most similar to the behaviors described in literature as cloud ignition. Since it is likely that in this system, looking at local autoignition events, any region with significant cooling would autoignite further downstream, these autoignition events correspond to local regions where cooling due mixing cold vaporized fuel is not as drastic and there exists a lean mixture such that the mixture is near the most reactive mixture fraction. Thibaut and Candel found this method of internal cloud ignition to be indicative of a region with longer droplet lifetime and quick chemistry [13]. To the best of the author's knowledge, this is the first experimental study of autoignition in a polydisperse fuel spray that can attest for this behavior in a real system.

Second, autoigniton kernels propagate towards regions with large droplets that have been vaporizing fuel. This behavior is very striated and non-uniform in nature due to the non-homogeneous two-phase flow. Since kernels do not propagate toward regions without visible droplets, or regions that could have completely vaporized small droplets it seems likely that these small droplets, in the quantity produced in this fuel spray, do not provide enough fuel vapor to support a most reactive mixture fraction or do not produce enough heat release to initiate reaction in nearby packets of fluid in order to provide an observable signal. Autoignition kernels that cannot propagate into higher fuel mixture fraction regions are unlikely to have a significant heat release.

Third, it was observed that when the flow field in the vicinity of the fuel injector changed to provide recirculation zones and enhanced mixing, autoignition kernels became more likely to form in the center of the flow, where there was previously not enough fuel

to support autoignition.

Lastly, at the highest temperatures studied in this work, the appearance of a continuously autoigniting flame was shown. Using high-speed chemiluminescence imaging it was shown that these flames "jump" upstream with corresponding velocities higher than the flame speed at these elevated temperatures. Upon further investigation using UV PLIF, it was shown that these continuous flames are in fact autoignition stabilized and anchor upon the continuous formation of distinct kernels feeding into a stabilized flame.

At the conditions investigated in this thesis, as autoignition transitions from being controlled primarily by chemical time at low temperatures to being controlled by droplet heat up time, the change in upstream location of autoignition becomes independent of temperature changes and the scatter in autoignition delay times becomes very short. The short chemical times lead to an autoignition stabilized flame that burns the fuel-air mixtures that were not yet capable of autoignition so kernels cannot be observed at downstream locations. As temperature becomes significantly high, i.e., $1200K$, autoignition can occur immediately when droplets vaporize so it will require only an estimate of droplet heat-up times to predict the location of autoignition. While the droplet heat up times are dependent upon the distribution of droplets in the fuel spray and the temperature at which the controlling times would change with a different fuel spray, it is important to show that this can affect the autoignition results at gas turbine relevant conditions. Fuel injection could be designed to control the spray distribution such that regions of droplets with intermediate average droplet size (for these flow temperatures and velocities, that corresponds to near $30\mu m$) and the location of likely autoignition could be controlled in order to better control the upstream region of heat release.

The implications of these observations can be used to inform the design of modern combustors that could be prone to autoignition. This work was motivated by two schools of thought on the presence of autoignition: autoignition can be used as a method of flame stabilization without the assistance of other stabilization methods or autoignition can occur

in wanted regions of an engine having unwanted consequences the most severe being engine failure. If autoignition is a desired component of engine design, it would be helpful to utilize the high temperature continuous flame regime. This study shows it is possible to stabilize a flame using autoignition that would be present at most locations in the combustor 100% of the time, as shown by the intermittency calculations, and would continuously burn the fuel that is injected. While this situation is prone to instabilities there are ways to dampen acoustic modes. A combustor that is more acoustically isolated from other components or utilizes Helmholtz resonators to dampen the acoustic modes may not be as susceptible as the open system tested here. The fuel spray could be designed in such a way as to control the regions of the flow that have higher likelihood of most reactive mixture fraction and therefore more autoignition kernels.

When autoignition is a safety concern and should be avoided, it is important to consider the most upstream appearance of kernels and whether they are capable of contributing enough heat release to effect the surroundings. If autoignition is being considered as a hindrance to engine lifetimes, it important to consider the impact of the kernel on its surroundings. When operating in the random kernels regime, the kernels often did not grow large enough to be observable on any time-averaged imaging technique and do not produce significant heat release. Depending on the residence time through a combustor, unless there is a region in a flow that could entrain a kernel and allow the kernel to burn more fuel it is possible that a single random autoignition event would not cause significant damage. As kernels become more frequent and occur more frequently in time their likelihood of transferring heat and damaging surroundings increases.

Expanding upon the implications of combustor design previously discussed, these "hot spots" due to non-uniformity can control the autoignition limits in a safety-oriented design. If autoignition must be completely absent, any flow that could have hot spots can autoignite with very minimal amount of vaporized fuel as shown with the most reactive mixture fraction. Again, it is important to control the interaction of non-uniformities in the heated air

flow and the presence of enough vaporized fuel to allow for a most reactive mixture fraction and propagation into a richer region of the two-phase flow. The small fluctuations in flow temperature will dominate the earliest ignition locations.

6.3 Future Work

The next logical step in contining this work would be to compile the statistics of more autoignition kernels. This would primarily rely on the ability to fully automate the detection of autoignition kernels from the UV PLIF imaging results.

Additionally, the importance of understanding the time-resolved behavior of flow conditions was shown with the variations in ignition delay times. A time-resolved temperature measurement should be added to elucidate the magnitude of temperature fluctuations in the co-flow. The variation of temperature should be compared to the scatter of the OH* chemiluminescence autoigntion locations and calculated "autoignition temperatures" to determine if the scatter is primarily due to changes in temperature or changes in mixture fraction, both of which impact reaction rates in the striated two-phase flow. The current model relies on single droplet size to calculate characteristic times. In a polydisperse spray, there will be droplets that heat up faster or persist as liquid droplets within the same regions. The modeling should be improved to investigate the effect of adding temperature fluctuations and a range of droplet size to determine the scatter in autoignition kernel location.

Gaseous studies have successfully characterized the fuel vapor and most reactive mixture fractions in a non-premixed system. While it would be difficult to follow the path of a packet of mixture before it autoignites, it would be still be useful to have an indication of local fuel vapor concentrations for autoignition kernel initiation and growth. A method of simultaneously visualizing fuel vapor in addition to fuel droplets and combustion would provide a way to prove that the kernels propagate into regions of prevaporized fuel once ignited.

In order to relate this work to other combustion applications, such as gas turbine main

combustors, it is important to consider the effect of pressure on the dominant processes in polydisperse autoigniton. First, an increase in pressure will increase the heat transfer coefficient, accelerating the heat-up of a droplet. An increasing pressure would decrease the enthalpy of vaporization, allowing the droplet to vaporize faster. These effects together will decrease the lifetime of droplets, providing more fuel vapor at earlier times in the spray. For ignition delay time, an increase in pressure will increase reaction rates and decrease the overall chemical time. All of the effects have a tendency to reduce the characteristic times that impact autoignition. Depending on the magnitide of these changes, the droplet heat-up and vaporization times could decrease slower than the decrease in ignition delay time, causing the droplet lifetime to become limiting at lower temperatures or it ignition delay could decrease at a slower rate and expand the region where the chemical times are controlling. These pressure effects should be studied in an appropriate high pressure flow reactor and improved modeling of characteristic times.

Appendices

APPENDIX A

EXAMPLE UV PLIF KERNELS AT FIRST INITIATION

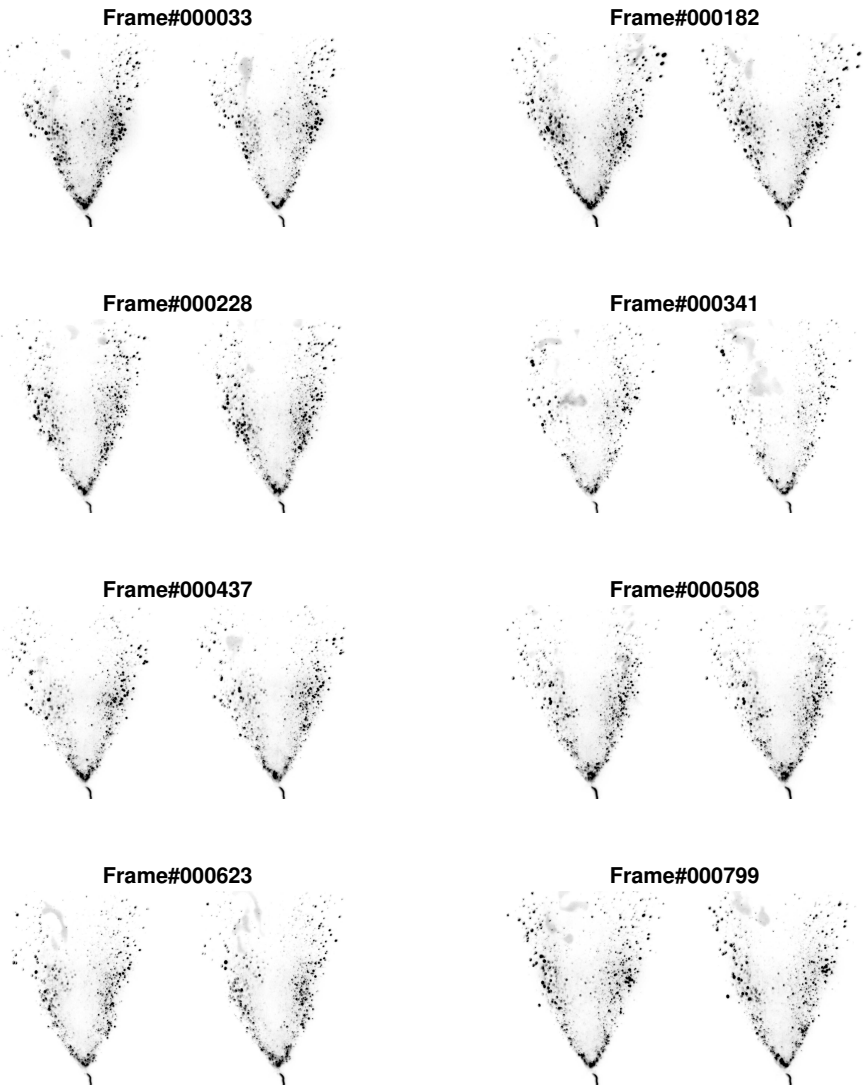

Figure A.1: Example kernels from UV PLIF with tapered fuel injector at T = $1143K$ and u = $43m/s$

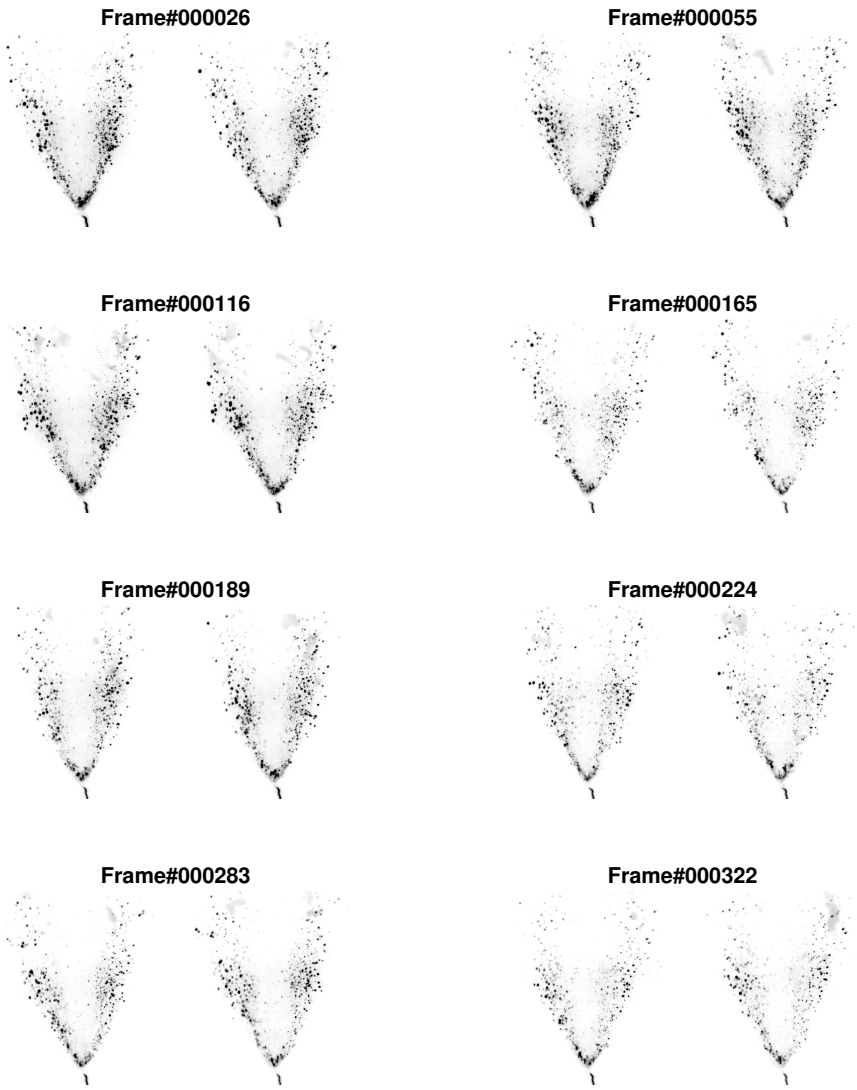

Figure A.2: Example kernels from UV PLIF with tapered fuel injector at T = $1213K$ and u = $43m/s$

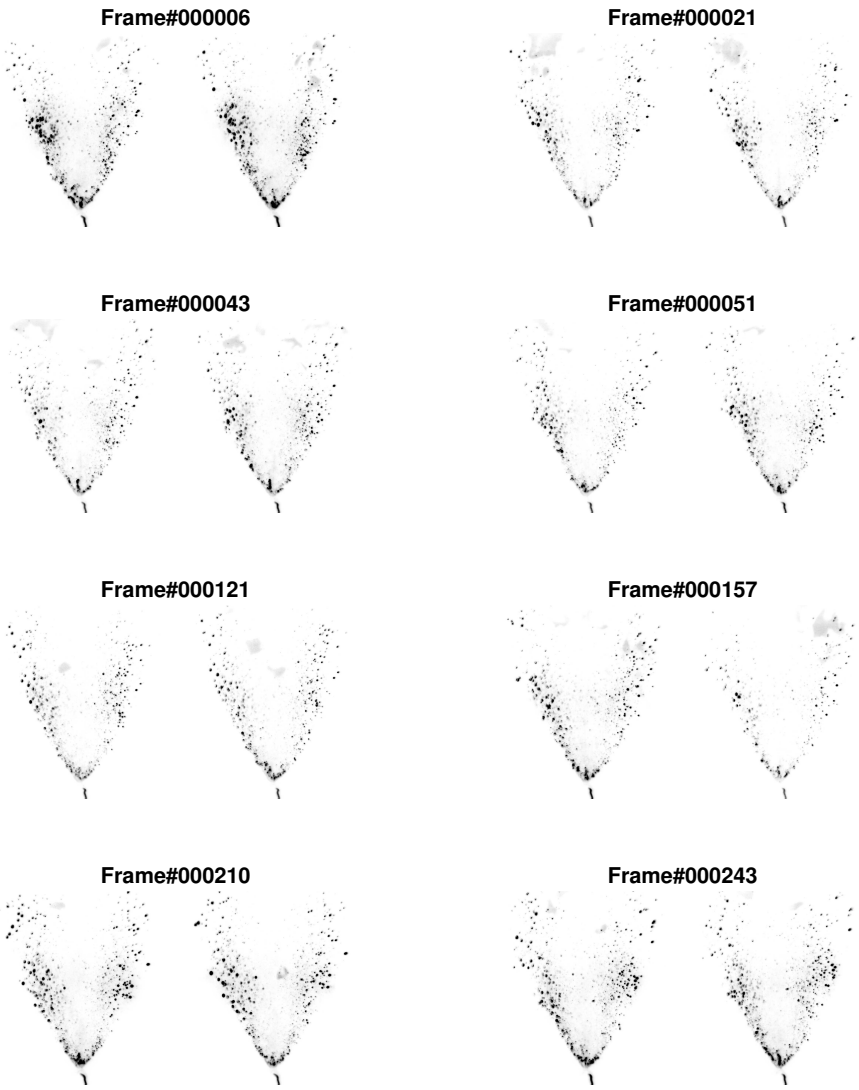

Figure A.3: Example kernels from UV PLIF with tapered fuel injector at T = $1280K$ and u = $43m/s$

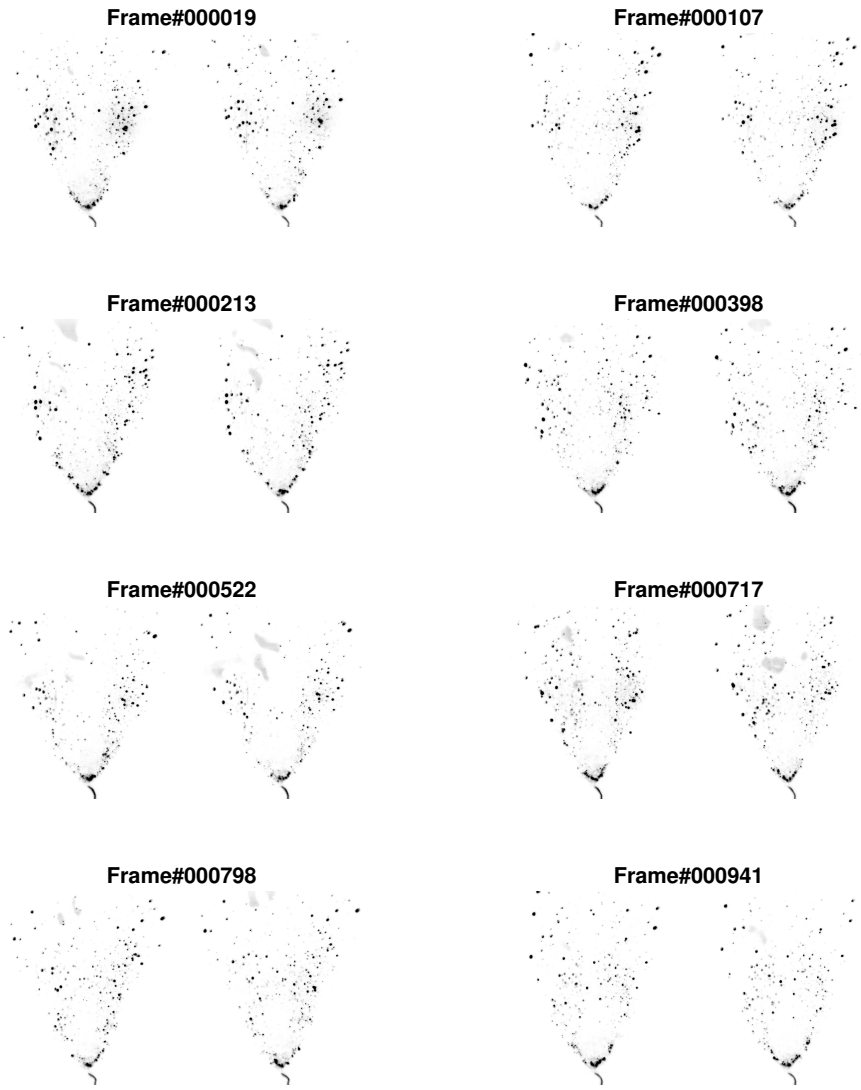

Figure A.4: Example kernels from UV PLIF with tapered fuel injector at T = $1106K$ and u = $33m/s$

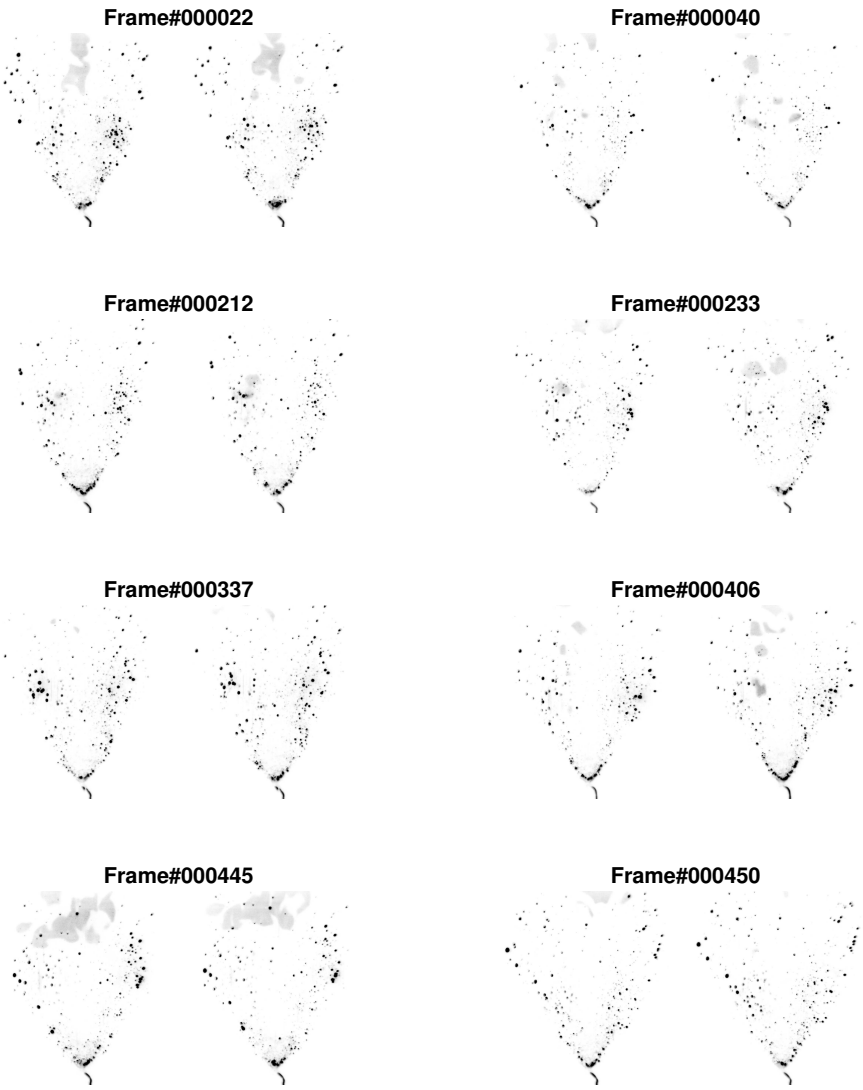

Figure A.5: Example kernels from UV PLIF with tapered fuel injector at T = $1137K$ and u = $33m/s$

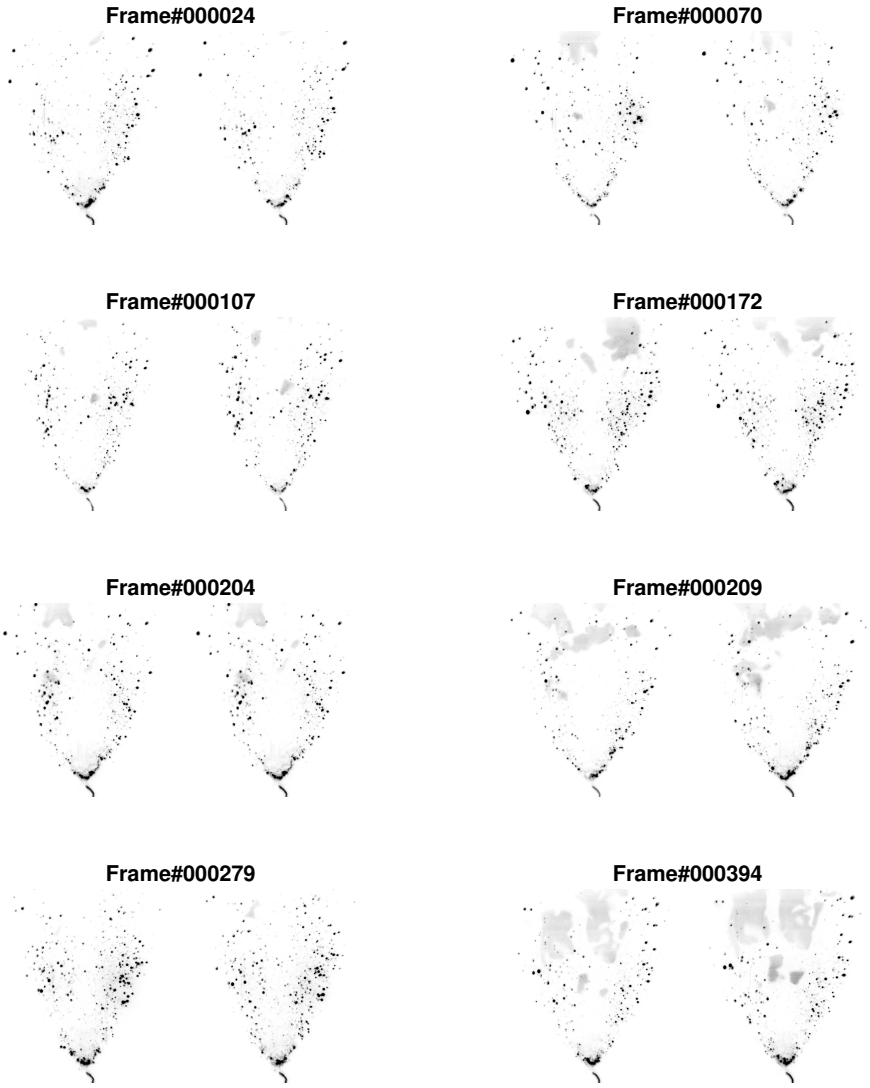

Figure A.6: Example kernels from UV PLIF with tapered fuel injector at T = 1211K and u = 33m/s

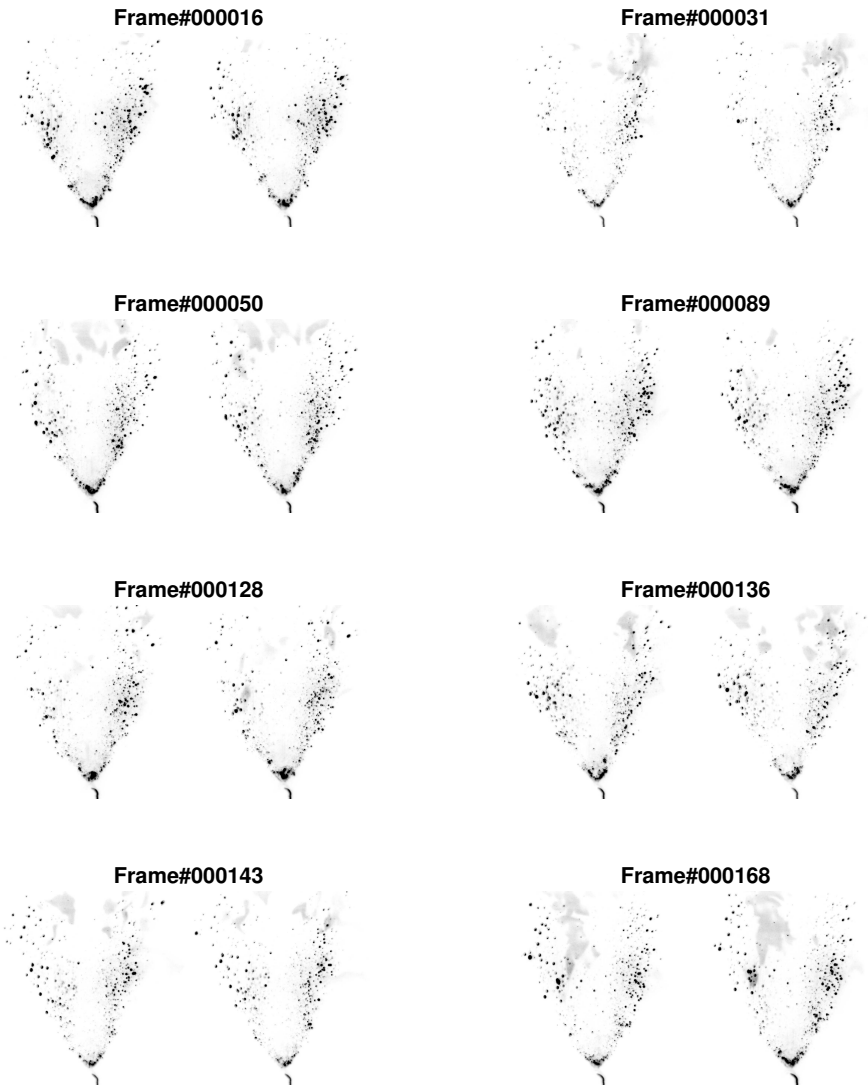

Figure A.7: Example kernels from UV PLIF with tapered fuel injector at T = $1272K$ and u = $33m/s$

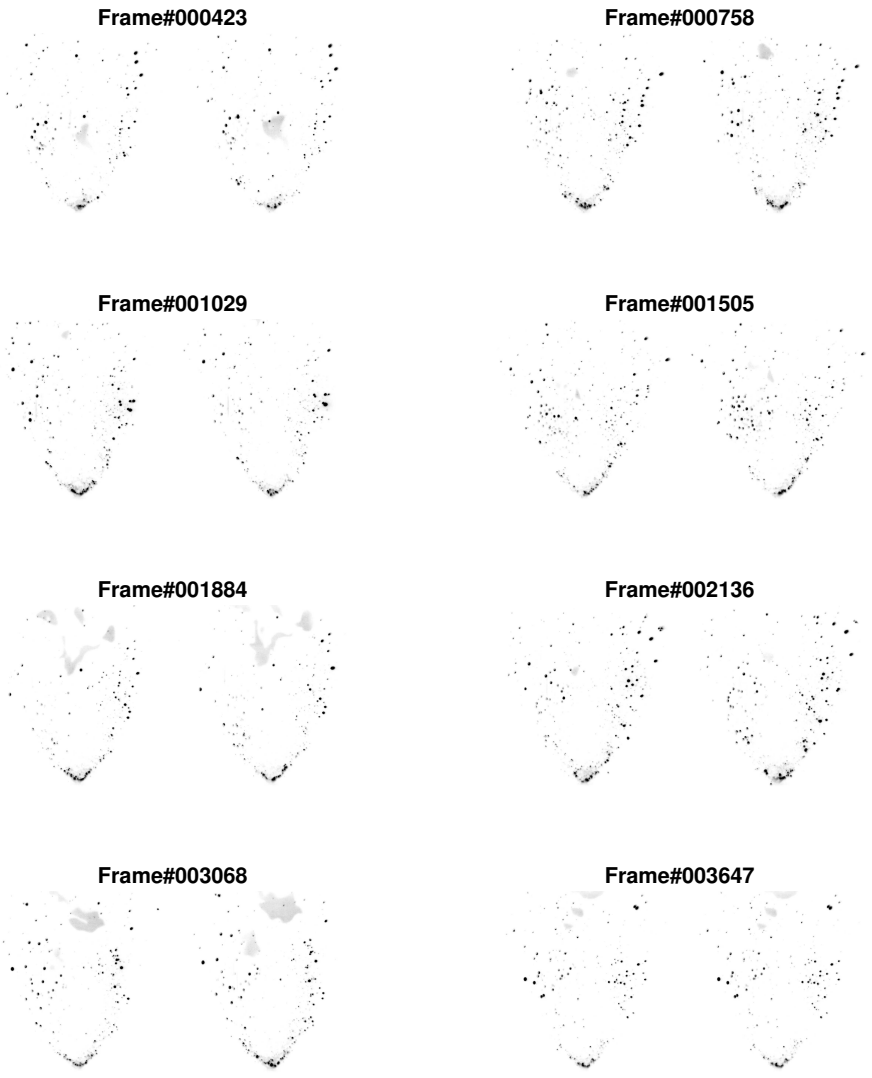

Figure A.8: Example kernels from UV PLIF with blunt fuel injector at T = 1138K and u = 31.8m/s

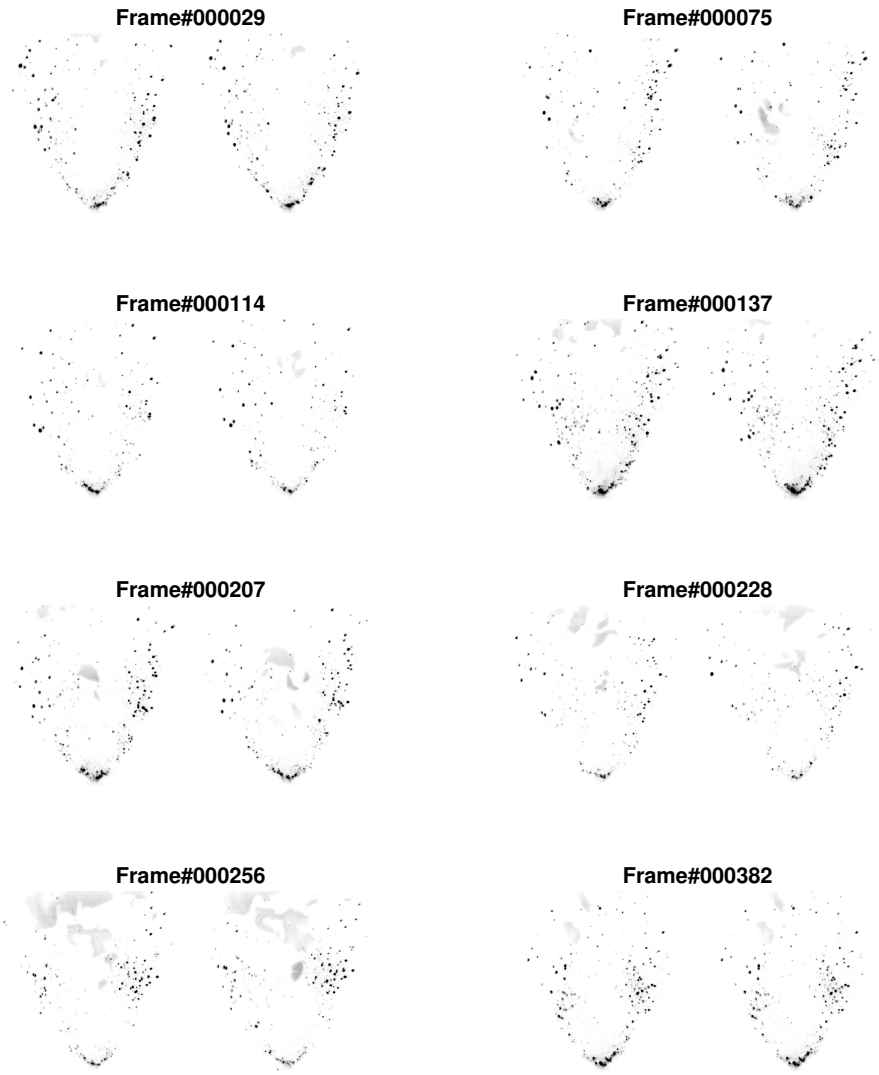

Figure A.9: Example kernels from UV PLIF with blunt fuel injector at T = 1180K and u = 34.2m/s

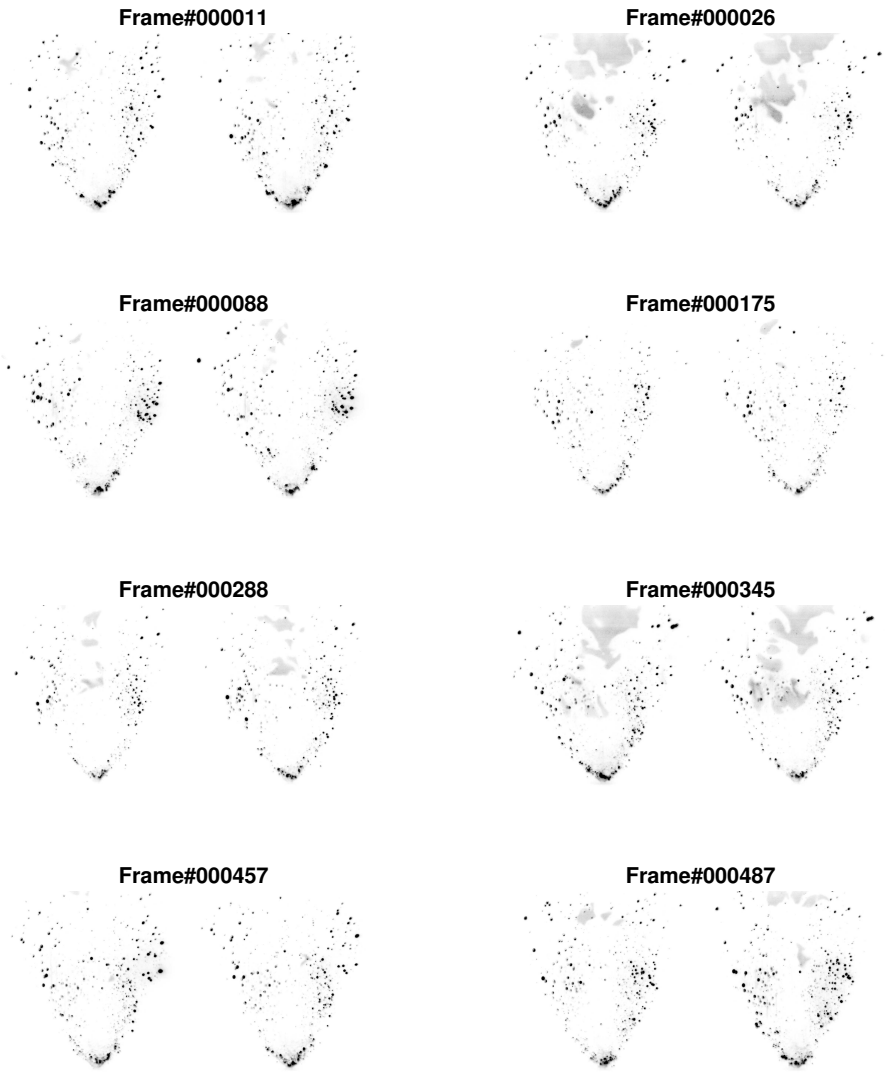

Figure A.10: Example kernels from UV PLIF with blunt fuel injector at T = $1204K$ and u = $35.4m/s$

APPENDIX B

DROPLET HEAT-UP AND VAPORIZATION CODE

```
%%%%%%%%%%%%%%%%%%%%%%%%%%%%%%%%%%%%%%%%%%%%%%%%%%%%%%%%%%%%%%%%%%%%%%%%%%%%
%%%%%%%%%%%%%%  Simple Droplet Heat-Up and Vaporization Model %%%%%%%%%%%%%%
%%%%%%%%%%%%%%%%%%%%%%%%%%%%%%%%%%%%%%%%%%%%%%%%%%%%%%%%%%%%%%%%%%%%%%%%%%%%
close all
clear
clc
%%%%%%%%%%%%%%%%%%%
%Input conditions%
%%%%%%%%%%%%%%%%%%%
d0 = 12*10^(-6); %um, droplet initial diameter
Td0 = 300; %K, droplet initial velocity
Tcf = 1200; %K, co-flow temperature
ucf = 40; %m/s, co-flow velocity
ud = 15; %m/s, droplet velocity

%%%%%%%%%%%%%%%
% Properties %
%%%%%%%%%%%%%%%
MW_f = 159;
Tboil = 462; %K, boiling point temperature
Tbar = 1/2*(Tboil + Tcf); %K, Average temperature for evaluating properties
cpg = 2.6*10^3; %J/kg-K, Specific heat of fuel vapor - at Tbar
kF = 0.08; %W/m-K, Thermal conductivity of fuel vapor - at Tbar
kcf = 0.0444; %W/m-K, Thermal conductivity of co-flow - at Tbar
kg = 0.4*kF + 0.6*kcf; %Average thermal conductivity of gas mixture
hfg = 428000; %J/kg, Heat of vaporization of fuel
rho_l = 800; %kg/m3, liquid density of fuel
%Vitiated air Properties:
MW_vitair = 27.66; %From gaseq
mu_vitair = -5.295*10^(-12)*Tcf^2+3.92*10^(-8)*Tcf+7.37*10^(-6); %kg/m/s Dynamic↙
viscosity - GasEq
nu_vitair = 6.693*10^(-11)*Tcf^2+7.263*10^(-8)*Tcf-1.718*10^(-5); %m2/s KinViscosity↙
- GasEq
cp_vitair = -0.0002188*Tcf^2+0.7555*Tcf+821.1; %J/kg/K
k_vitair = -1.049*10^(-8)*Tcf^2+8.122*10^(-5)*Tcf-0.00264; %J/m/K/s
rho_vitair = 2.832e-07*Tcf^2-0.0009102*Tcf+0.9647; %kg/m3 - from GasEq

%%%%%%%%%%%%%%%%%
% Calculations %
%%%%%%%%%%%%%%%%%
Psat = exp(-(hfg/8315)*MW_f/1000*(1/Tbar-1/Tboil)); %Saturation pressure
X_surf = Psat; %Mole fraction of fuel on droplet surface
Y_surf = X_surf*MW_f/(MW_f+MW_vitair); %Mass fraction of fuel on droplet surface
BM = Y_surf/(1-Y_surf); %Mass-based Spalding number
FBM = (1+BM)^(0.7)*log(1+BM)/BM; %Function of BM
% Reynolds Number:
Red = abs(ucf-ud)*d0/nu_vitair;
%Prandtl Number:
Prd = cp_vitair*mu_vitair/k_vitair;
```

```
%Nusselt Number:
BT = cpg*(Tcf-Td0)/hfg;
FBT = (1+BT)^(0.7)*log(1+BT)/BT;
Nu0 = 2*(log(1+BT)/BT)*(1 + ((1+Red*Prd)^(1/3)*max([1,Red^0.077])-1)/(2*FBT));
Nu = 2 + 0.555*Red^.5*Prd^.3333/(1+1.232/(Red*Prd^1.3333))^0.5;
%%%%%%%%%%
% Sahzin %
%%%%%%%%%%
%Setup time
dt = 1E-6;
t0 = 0;
ii = 1;
Td = Td0;
while Td<Tboil
%Calculation function of time
%for ii = 1:length(t)
%ti = t(ii);
ti = t0+ii*dt;
h = Nu0*kF/(d0);
Td(ii) = Tcf + (Td0-Tcf)*exp(-3*h*ti/(cpg*rho_l*d0/2)); %Droplet temp - function of↙
time
ii = ii+1;
end
t = 1:1:length(Td);
t = t.*dt;

t_hu = max(t)
%%%%%%%%%%%%%%%%%%%%%%%%
% Droplet Evaporation %
%%%%%%%%%%%%%%%%%%%%%%%%
Bq = cpg*(Tcf-Tboil)/hfg;
K = 8*kg/rho_l/cpg*log(Bq+1);
td = d0^2/K
%Setup Time for evaporation, starting at vaporization end
tevap = t_hu:dt:(td+t_hu);
Rd = 0.5*(d0^2-K*(tevap-t_hu)).^(1/2);
%%%%%%%%%%%%%%%%
% Plot Results %
%%%%%%%%%%%%%%%%
tplot = [t, tevap];
Td(length(t)+1:length(tevap)+length(t)) = Tboil;
figure
set(gcf, 'position', [200, 100, 400, 250], 'color', 'w')
yyaxis left
plot(tplot*1000, Td)
ylabel('Droplet Temperature (K)', 'fontweight', 'bold')
hold on
yyaxis right
plot(t*1000, ones(length(t))*d0/2*10^6, '-')
```

```
plot(tevap*1000, Rd*10^6, '-')
ylabel('Droplet Radius (\mum)', 'fontweight', 'bold')
xlabel('Time (ms)', 'fontweight', 'bold')
```

REFERENCES

[1] J. A. Lovett, T. P. Brogan, D. S. Philippona, B. V. Keil, and T. V. Thompson, "Development needs for advanced afterbuner designs," in *40th AIAA/ASMA/SAE/ASEE Joint Propulsion Conference and Exhibit*, 2004.

[2] J. T. Cutright, Y. Neumeier, B. T. Zinn, and E. Shahid, "Ignition triggering of afterburner fuel using partial oxidation mixtures," in *Proceedings of ASME Turbo Expo*, 2009.

[3] A. Tammer, J. T. Cutright, Y. Neumeier, and B. T. Zinn, "Performance comparison of aero-engine thrust augmentors stabilized by bluff body flames holders and a flameholder-less concept," in *Proceedings of ASME Turbo Expo*, 2011.

[4] M. C. Wolff, J. Meisl, R. Koch, and S. Wittig, "The influence of evaporation on the autoignition-delay of n-heptane air mixtures under gas turbine conditions," in *27th Symposium (Intl.) on Combustion*, 1998.

[5] C. K. Westbrook and F. L. Dryer, "The ignition, oxidation, and combustion of kerosene: A review of experimental and kinetic modeling," *Prog. Energy Combust. Sci*, vol. 32, no. 1, pp. 1–57, 1984.

[6] H. Wang and M. A.Oehlschlaeger, "Autoignition studies of conventional and fischer-tropsch fuels," *Fuel*, vol. 98, pp. 249–258, 2012.

[7] A. Williams, *Combustion of Liquid Fuel Sprays*. Butterworths, 1990.

[8] P. Dagaut and M. Cathonnet, "The ignition, oxidation, and combustion of kerosene: A review of experimental and kinetic modeling," *Progress in Energy and Combustion Science*, vol. 32, pp. 48 –92, 2006.

[9] W. A. Sirignano, "Fuel droplet vaporization and spray combustion theory," *Progress in Energy and Combustion Science*, vol. 9, no. 4, pp. 291 –322, 1983.

[10] W. A. Sirignano, "Advances in droplet array combustion theory and modeling," *Prog. Energy Combust. Sci.*, vol. 42, pp. 54–86, 2014.

[11] A. Stagni, L. Esclapez, P. Govindaraju, A. Cuoci, T. Faravelli, and M. Imhe, "The role of preferential evaporation on the ignition of multicomponent fuels in a homogeneous spray/air mixture," *Proceedings of the Combustion Institute*, 2016.

[12] S. K. Aggarwal, "A review of spray ignition phenomena: Present status and future research," *Prog. Energy Combust. Sci*, vol. 24, pp. 565–600, 1998.

[13] D. Thibaut and S. Candel, "A simple model of ignition modes of dense droplet clouds," in *26th Symposium (Intl.) on Combustion*, 1996.

[14] C. K. Law, "Theory of thermal ignition and extinction in droplet burning," *Combustion and Flame*, vol. 26, pp. 89–98, 1975.

[15] C. K. Law, "Theory of thermal ignition in fuel droplet burning," *Combustion and Flame*, vol. 31, no. 285-296, 1978.

[16] S. K. Aggarwal, "Single droplet ignition: Theoretical analyses and experimental findings," *Prog. Energy Combust. Sci*, vol. 45, pp. 79–107, 2014.

[17] K. Annamalai and W. Ryan, "Interactive processes in gasification and combustion. part i: Liquid drop arrays and clouds," *Prog. Energy Combust. Sci*, vol. 18, pp. 221–295, 1992.

[18] J. J. Sangiovanni and A. S. Kesten, "Effect of droplet interaction on ignition in monodispersed droplet streams," *16th Symposium (International) on Combustion*, pp. 577–592, 1977.

[19] R. L. Gordon, C. N. Markides, and E. Mastorakos, "Autoignition of liquid fuel droplets in a turbulent cross-flow of air," *49th AIAA Aerospace Sciences Meeting*, 2011.

[20] R. L. Gordon and E. Mastorakos, "Autoignition of monodisperse biodiesel and diesel sprays in turbulent flows," *Experimental Thermal and Fluid Science*, vol. 43, pp. 40–46, 2012.

[21] W. R. Laster and K. Annamalai, "Ignition delay of droplet clouds: Results from group combustion theory," *Chemical Eng. Commun.*, vol. 105, pp. 201–219, 1991.

[22] J. Bellan and K. Harstad, "Ignition of non-dilute clusters of drops in convective flows," *Combust. Sci. and Technol.*, vol. 53, pp. 75–87, 1987.

[23] B. P. Mullins, "Studies on the spontaneous ignition of fuels injected into a hot air stream," *Fuel*, 1953.

[24] L. J. Spadaccini and J. A. TeVelde, "Autoignition characteristics of aircraft-type fuels," NASA CR-159886, Tech. Rep., 1980.

[25] G. Freeman and A. H. Lefevbre, "Spontaneous ignition characteristics of gaseous hydrocarbon-air mixtures," *Combustion and Flame*, vol. 58, pp. 153–162, 1984.

[26] P. Gokulakrishnan, G. Gaines, J. Currano, M. S. Klassen, and R. J. Roby, "Experimental and kinetic modeling of kerosene-type fuels at gas turbine operating conditions," *Journal of Engineering for Gas Turbines and Power*, vol. 129, no. 3, pp. 655–663, 2007.

[27] A. Williams, D. Schherbik, O. Bibik, E. Lubarsky, and B. T. Zinn, "Autoignition of a jet-a fuel spray in a high temperature vitiated air flow," *Proceedings of the ASME Turbo Expo*, 2015.

[28] P. Gokulakrishnan, G. Gaines, M. Klassen, and R. Roby, "Autoignition of aviation fuels: Experimental and modeling study," in *Joint Propulsion Conferences*, American Institute of Aeronautics and Astronautics, Jul. 2007.

[29] C. Markides, G. D. Paola, and E. Mastorakos, "Measurements and simulations of mixing and autoignition of an n-heptane plume in a turbulent flow of heated air," *Experimental Thermal and Fluid Science*, vol. 31, no. 5, pp. 393 –401, 2007, Fourth Mediterranean Combustion Symposium {MCS04}.

[30] C. C. Fuller, P. Gokulakrishnan, M. S. Klassen, R. J. Roby, and B. V. Kiel, "Investigation of the effects of vitiated conditions on the autoignition of jp-8," in *45th AIAA/ASME/SAE/ASEE Joint Propulsion Conference & Exhibit*, 2009.

[31] A. Schönborn, P. Sayad, and A. A. K. J. Klingmann, "Visualisation of propane autoignition in a yurbulent flow reactor using oh* chemiluminescence imaging," *Combustion and Flame*, vol. 160, pp. 1033–1043, 2013.

[32] J. M. Fleck, P. Griebel, A. M. Steinberg, C. M. Arndt, C. Naumann, and M. Aigner, "Autoignition of hydrogen/nitrogen jets in vitiated air crossflows at different pressures," *Proceedings of the Combustion Institute*, 2012.

[33] W. Meier, I. Boxx, C. Arndt, M. Gamba, and N. Clemens, "Investigation of autoignition of a pulsed methane jet in vitiated air using high-speed imaging techniques," *Journal of Engineering for Gas Turbines and Power*, vol. 133, 2011.

[34] C. M. Arndt, J. D. Gouder, W. Meier, and M. Aigner, "Auto-ignition and flame stabilization of pulsed methane jets in a hot vitiated coflow studied with high-speed laser imaging techniques," *Applied Physics B: Lasers and Optics*, vol. 108, pp. 407–417, 2012.

[35] A. Krisman, E. R. Hawkes, and J. H. Chen, "Two stage autoignition and edge flames in a high pressure turbulent jet," *J. Fluid Mech*, vol. 824, pp. 5–41, 2017.

[36] E. Mastorakos, "Ignition of turbulent non-premixed flames," *Prof Energ Comb Sci.*, 2009.

[37] Markides, "Autoignition in turbulent flows," PhD thesis, University of Cambridge, 2005.

[38] W. OLoughlin and A. Masri, "A new burner for studying auto-ignition in turbulent dilute sprays," *Combustion and Flame*, vol. 158, no. 8, pp. 1577 –1590, 2011.

[39] O. Hinkeldey, R. S. l, M. Cano-Wolff, R. Koch, H. J Bauer, and U. Maas, "Laser based study of autoignition of sprays in a continuous flow reactor," *Proceedings of the European Combustion Meeting*, 2007.

[40] O. Hinkeldey, R. Koch., J. Bauer, M. Cano-Wolff, and P. Schober, "Laser based study of spray auto-ignition in a generic mixing duct," in *Proceedings of ASME Turbo Expo*, 2008.

[41] Z. Wang, P. Stamatoglou, Z. Li, M. P. Aldén, and M. Richter, "Ultra-high-speed plif imaging for simultaneous visualization of multiple species in turbulent flames," *Optics Express*, 2017.

[42] M. Orain, P. Baranger, C. Ledier, J. Apeloig, and F. Grisch, "Fluorescence spectroscopy of kerosene vapour at high temperatures and pressures: Potential for gas turbine measurements," *Applied Physics B*, vol. 116, no. 3, pp. 729–745, 2014.

[43] H. Wang, R. Xu, K. Wang, D. F. Davidson, R. K. Hanson, K. Brezinsky, and F. N. Egolfopoulos, "A physics-based approach to modeling real-fuel combustion chemistry - i. evidence from experiments, and thermodynamic, chemical kinetic and statistical considerations," *Combustion and Flame*, vol. 193, pp. 502–519, 2018.

[44] R. Xu, K. Wang, S. Banerjee, J. Shao, T. Parise, Y. Zhu, S. Wang, A. Movaghar, D. J. Lee, R. Zhao, X. Han, Y. Gao, T. Lu, K. Brezinsky, F. N. Egolfopoulos, D. F. Davidson, R. K. Hanson, C. T. Bowman, and H. Wang, "A physics-based approach to modeling real-fuel combustion chemistry - ii. reaction kinetic models of jet and rocket fuels," *Combustion and Flame*, vol. 193, pp. 520–537, 2018.

[45] S. S. Sahzin, T. Kristyadi, W. A. Abdelghaffar, and M. R. Heikal, "Models for fuel droplet heating and evaporation: Comparative analysisfuel," *Fuel*, vol. 85, pp. 1613–1630, 2006.

[46] B. Abramazon and W. A. Sirignano, "Droplet vaporization model for spray combustion calculations," *Int. J. Heat Mass Transfer*, vol. 32, no. 9, pp. 1605–1618, 1989.

[47] S. R. Turns, *An Introduction to Combustion*. McGraw-Hill, 2011.